Electrode Design for Durable and Energy-Dense Rechargeable Zinc-Air Batteries

by

Zachary Paul Cano

A thesis

presented to the University of Waterloo

in fulfillment of the

thesis requirement for the degree of

Doctor of Philosophy

in

Chemical Engineering (Nanotechnology)

Waterloo, Ontario, Canada, 2020

Examining Committee Membership

The following served on the Examining Committee for this thesis. The decision of the Examining Committee is by majority vote.

External Examiner	Dr. Steen B. Schougaard Professor
Supervisor	Dr. Michael Fowler Professor
Internal Member	Dr. Zhongwei Chen Professor
Internal Member	Dr. Michael Pope Professor
Internal-external Member	Dr. Feridun Hamdullahpur Professor

Author's Declaration

This thesis consists of material all of which I authored or co-authored: see Statement of Contributions included in the thesis. This is a true copy of the thesis, including any required final revisions, as accepted by my examiners.

I understand that my thesis may be made electronically available to the public.

Statement of Contributions

The body of this thesis is based upon a combination of published and unpublished works.

Chapter 1 and **Chapter 3** of this thesis contain parts of a review paper that was co-authored by myself, my supervisor, Dr. M. Fowler, two collaborators, Drs. A. Yu and Z. Chen, and two PhD students, Dr. J. Fu and M. Park. Dr. Fu and I contributed equally to the data collection and primary manuscript writing, and M. Park assisted with data collection and manuscript writing. All authors reviewed the manuscript.

"Electrically rechargeable zinc-air batteries: progress, challenges and perspectives", *Advanced Materials*, 29 (7) (2017) 1604685.

Chapter 2 and the introduction to **Chapter 3** were adapted from a review paper that was co-authored by myself, my supervisor (Dr. M. Fowler), and five collaborators (Dr. D. Banham, Dr. S. Ye, Dr. A. Hintennach, Dr. J. Lu and Dr. Z. Chen). I created the manuscript synopsis, collected and analyzed data from the literature, and primarily wrote the manuscript. Dr. Fowler and Dr. Chen assisted with the manuscript synopsis and manuscript writing. Drs. Banham, Ye, Hintennach and Lu assisted with manuscript writing. Dr. Hintennach provided additional battery and fuel cell data courtesy of Daimler, AG. All authors reviewed the manuscript.

"Batteries and fuel cells for emerging electric vehicle markets", *Nature Energy*, 3 (4) (2018) 279-289.

Chapter 4 of this thesis is adapted from a paper that was co-authored by myself, my supervisor, Dr. M. Fowler, three PhD students, M. Park, Dr. J. Fu, and H. Liu, one post-doctoral fellow, Dr. D. Lee, and one collaborator, Dr. Z. Chen. I designed and carried out the experiments, collected and analyzed the data, and primarily wrote the manuscript. M. Park assisted with X-ray diffraction analysis and manuscript writing. H. Liu, Dr. Fowler, and Dr. Chen assisted with the experimental design and discussion. Dr. Lee and Dr. Fu assisted with discussion and manuscript writing. All authors reviewed the manuscript.

"New Interpretation of the Performance of Nickel-Based Air Electrodes for Rechargeable Zinc–Air Batteries", *Journal of Physical Chemistry C*, 122 (35) (2018) 20153-20166.

Chapter 5 of this thesis consists of previously unpublished work by myself, my supervisor, Dr. M. Fowler, two PhD students, M. Park, and H. Liu, and one collaborator, Dr. Z. Chen. I designed and carried out the experiments, collected and analyzed the data, and wrote all parts of the chapter. M. Park assisted with X-ray diffraction analysis. H. Liu, Dr. Fowler, and Dr. Chen assisted with the experimental design and discussion.

Abstract

Energy storage has become an increasingly important topic due to the need for rapid deployment of intermittent renewable energy sources and electric vehicles (EVs) around the world. Today's EVs, which have entered mass-market production over the past decade, are almost exclusively powered by lithium-ion batteries. However, there is a long way to go before EVs become dominant in the global automotive market. In addition to global government policy support, widespread deployment of EVs will likely require high-performance and low-cost energy storage technologies including both batteries and fuel cells. Zinc-air batteries have been proposed as a low-cost and energy-dense candidate to replace or supplement lithium-ion batteries in EVs; however, an electrically rechargeable zinc-air battery with a sufficient combination of energy density, cycle life and calendar life for this application has yet to be developed. In an effort to address this research gap, this thesis (i) explores the viability of zinc-air battery technology in EVs with a thorough and evaluative literature review and (ii) experimentally investigates the use of nickel-based air electrodes for durable and energy-dense rechargeable zinc-air batteries.

This work begins with a comprehensive evaluation of various batteries and hydrogen fuel cells possessing the greatest potential to benefit future EVs. Three sectors that are not well served by current lithium-ion powered EVs, namely the long-range, low-cost and high-utilization transportation markets, are discussed. The technology properties which must be improved upon to fully enable these EV markets include specific energy, cost, safety and power grid compatibility. Six energy storage and conversion technologies which possess varying combinations of these

improved characteristics are compared and separately evaluated for each market. Then, the technological status of these battery and fuel cells are briefly reviewed, emphasizing barriers which must be overcome. Zinc-air batteries are identified as one of the technologies which could enable lower-cost and longer-range EVs, particularly when used as a range extender in conjunction with another battery with complementary properties.

Next, a detailed review of the current status and technological barriers of zinc-air batteries is provided. The limited cycle life and calendar life of these batteries is mainly caused by dendritic growth and shape change of the zinc electrode in addition to corrosion and carbonate formation at the air electrode. A variety of zinc electrodes and air electrodes designed to mitigate these issues are evaluated, with a specific focus on the potential of these electrodes to be used in long-lasting energy-dense zinc-air batteries.

The next part of the thesis focuses on nickel-based air electrodes, which have shown promise as a corrosion-resistant substitute for conventional carbon-based air electrodes but have not previously undergone an in-depth study of their performance in zinc-air batteries. Specifically, the effect of the nickel (oxy)hydroxide passivating film on the electrode's catalytic performance and durability requires investigation. To fill this research gap, a method involving electrochemical estimation of the nickel (oxy)hydroxide film capacity was used to correlate the growth of the film to performance losses experienced on the air electrode after battery cycling. The main cause of voltage loss was determined to be the nickel (oxy)hydroxide film growing overtop of and inside the catalyst-coated nickel aggregates. This resulted in significant activation and mass transfer losses, where the latter losses were caused by the film growing overtop of the catalyst and

accounted for at least 65% of the total voltage degradation at 10 mA cm^{-2}. Potential modifications to the electrode structure which could mitigate these voltage losses are discussed, including reducing the nickel particle aggregate size, using high-aspect ratio catalysts, and physically separating the catalyst and nickel particles with non-film-forming conductive additives.

Finally, a new nickel-based air electrode having both improved cycle life and substantially lower mass and volume than previous designs is presented. The thin nickel foam-based electrode can provide more than 1100 charge-discharge cycles during over 700 hours of operation with a discharge potential over 1.0 V vs. Zn at a current density of 10 mA cm^{-2}, or more than 500 charge-discharge cycles during over 340 hours of operation with a discharge potential over 1.0 V vs. Zn at a current density of 20 mA cm^{-2}. Estimates of the specific energy and energy density of rechargeable zinc-air batteries incorporating this air electrode paired with various reversible zinc electrodes from the literature are calculated. From these results, the potential viability of this electrode and future work needed to successfully develop an energy-dense rechargeable zinc-air battery for EVs are discussed.

Acknowledgements

I would first like to thank my supervisor, Professor Michael Fowler, for the guidance and dependable support he provided to me during my PhD degree work. His enthusiasm and openness always made me feel comfortable to work on several different projects during my studies. I also want to thank my committee member, Professor Zhongwei Chen, for providing additional guidance and support as well as the opportunity to work in his lab and collaborate with members of his research group. I also want to thank my entire examining committee for their time in reviewing my proposed work and thesis and for the feedback they gave me.

I would also like to thank all the students and researchers in Dr. Fowler's and Dr. Chen's groups for helping me with setting up experiments, giving me suggestions for new things to try, giving me feedback on my writing and presentations, and most importantly for their friendship and kindness. In particular, Moon Gyu Park, Hao Liu, Dr. Dong Un Lee, Dr. Jing Fu, and Dr. Yining Zhang greatly helped me with my work. I would also like to thank the National Sciences and Engineering Research Council of Canada (NSERC) and the University of Waterloo for providing additional financial support during my studies.

Finally, I would like to thank my family and friends for their patience and support over the past four-plus years. Most of all, I want to thank my partner Catherine Silva not only for pointing me to some literature that I missed, including a reference that was very useful for improving the performance of the nickel-based air electrode, but also for making me laugh and for being my best friend over the past decade.

Table of Contents

Examining Committee Membership ..... **ii**

Author's Declaration ..... **iii**

Statement of Contributions ..... **iv**

Abstract ..... **vi**

Acknowledgements ..... **ix**

List of Figures ..... **xiii**

List of Tables ..... **xvii**

List of Abbreviations ..... **xx**

Chapter 1: Introduction **1**

1.1 Motivation 1

1.2 Thesis Objectives and Structure 5

Chapter 2: Evaluation of Batteries and Fuel Cells for Emerging Electric Vehicle Markets 6

2.1 Introduction 6

2.2 Energy Storage Barriers in Emerging Electric Vehicle Markets 8

2.2.1 Long-Range Transport 8

2.2.2 Low-Cost Transport 11

2.2.3 High-Utilization Transport 13

2.3 Evaluation of Electrochemical Technology Candidates 15

2.3.1 Commercial Rechargeable Batteries 22
2.3.2 Emerging Rechargeable Batteries 23
2.3.3 Hydrogen Fuel Cells 27
2.4 Conclusions 33

Chapter 3: Challenges and Strategies for Designing Energy-Dense Rechargeable Zinc-air Battery Electrodes 35

3.1 Introduction 35
3.2 Zinc-Air Battery Operation and Configuration 36
3.3 Reversible Zinc Electrode 41
3.3.1 Performance-Limiting Phenomena 41
3.3.2 Strategies for Improving Performance 44
3.4 Electrolyte and Separator 48
3.5 Bifunctional Air Electrode 53
3.4.1 Electrode Design 54
3.4.2 Oxygen Reaction Catalysts 59

Chapter 4: Performance and Failure Mechanism of Nickel-Based Air Electrodes for Rechargeable Zinc-Air Batteries 62

4.1 Introduction 62
4.2 Experimental Methods 64
4.2.1 Electrode Preparation and Characterization 64
4.2.2 Cell Design 67
4.2.3 Electrochemical Testing 68
4.3 Results and Discussion 73
4.4 Conclusions 96

Chapter 5: Design and Feasibility of Thin Nickel Foam-Based Air Electrodes for Rechargeable Zinc-Air Batteries 98

5.1 Introduction 98

5.2 Experimental Methods 99

5.3 Results and Discussion 104

5.3.1 Physical Characterization 104

5.3.2 Electrochemical Cycling Evaluation 113

5.3.3 Specific Energy and Energy Density Estimation 128

5.4 Conclusions 130

Chapter 6: Conclusions and Future Work 132

6.1 Conclusions 132

6.2 Future Work 135

Letters of Copyright Permission 138

1. John Wiley and Sons / Advanced Materials 138

2. Springer Nature / Nature Energy 144

3. American Chemical Society / The Journal of Physical Chemistry C 146

References 147

Appendix 159

Theoretical Specific Energy Calculation 159

Theoretical Metal-Air Battery Parameters 161

Supplementary Tables for Chapter 2 162

List of Figures

Figure 1.1. Theoretical specific energies, volumetric energy densities and nominal cell voltages for various metal anodes in aqueous and non-aqueous metal-air batteries. 3

Figure 2.1. Evolution of cumulative EV sales and EV market share prescribed in the International Energy Agency's Beyond 2 Degrees Scenario. [37] 8

Figure 2.2. 2017 model EV ranges and price premiums. 10

Figure 2.3. Consumer vehicle purchasing habits in the United States versus emerging countries. 13

Figure 2.4. Characteristics of rechargeable batteries and hydrogen fuel cells. 16

Figure 2.5. Vehicle cost and cost of additional range as a function of driving range. 19

Figure 2.6. Sensitivity plots of midsize vehicle cost and range. 21

Figure 2.7. Vehicle cost as a function of driving range for Li-ion battery and hydrogen fuel cell EVs. 30

Figure 2.8. Suitability of alternative batteries and fuel cells to emerging EV markets. 34

Figure 3.1. Schematic operating mechanism of a rechargeable Zn-air battery. 37

Figure 3.2. Schematic representation of prismatic Zn-air battery configuration. 39

Figure 3.3. Multi-cell Zn-air battery configuration with molopolar arrangement and bipolar arrangement. 40

Figure 3.4. Schematic representation of performance-limiting phenomena that may occur on the Zn electrode: dendrite growth, shape change, passivation, hydrogen evolution. 41

Figure 3.5. Electrolyte conductivity, Zn/Zn^{2+} exchange current density and ZnO solubility as a function of KOH concentration 51

Figure 3.6. Example of discharge and charge voltages, power density and energy efficiency as a function of current density for a rechargeable zinc-air battery. 54

Figure 3.7. General architecture of fuel cell or metal-air battery air electrode. 56

Figure 3.8. Schematic representations of pore structures within AL composed of catalyst-coated carbon powders and PTFE particles. 57

Figure 4.1. Schematic depiction of single-layer nickel-based gas diffusion electrode, and schematic representations of three-electrode cells for performance evaluation of nickel-based gas diffusion electrode and nickel-based thin-layer electrode 66

Figure 4.2. Graphical demonstration of two-step reduction and two-step oxidation cycles and the dominant reactions occurring at each step. 71

Figure 4.3. SEM images of the nickel particle morphology, the Ni/PTFE slurry-deposited side of the electrode, the non-slurry side of the electrode and the deposited $NiCo_2O_4$ catalyst. 74

Figure 4.4. Galvanostatic cycling results for nickel-based gas diffusion electrode. 76

Figure 4.5. SEM images of the nickel-based gas diffusion electrode before cycling and after 100 galvanostatic oxidation/reduction cycles. 78

Figure 4.6. XRD spectra of the nickel-based gas diffusion electrode surface before cycling and after 10 and 100 galvanostatic oxidation/reduction cycles. 79

Figure 4.7. XPS analysis of the nickel-based gas diffusion electrode before and after 10 and 100 galvanostatic oxidation/reduction cycles. 81

Figure 4.8. Galvanostatic EIS plots for nickel-based gas diffusion electrode. 85

Figure 4.9. Cyclic potentiodynamic polarization results for nickel-based gas diffusion electrode. 86

Figure 4.10. Magnified ORR polarization curves from **Figure 4.9**a. 90

Figure 4.11. Cyclic potentiodynamic polarization for nickel-based thin-layer electrode..... 93

Figure 4.12. Schematic representation of an electrolyte-flooded agglomerate of catalyst-coated nickel particles showing the nickel oxy(hydroxide) film growth resulting from prolonged oxidation. 95

Figure 5.1. SEM images of thin nickel-foam based air electrode..... 105

Figure 5.2. SEM images of the thin nickel foam-based air electrode after various stages of preparation. 108

Figure 5.3. XRD spectra of the nickel foam-based air electrode after various stages of preparation. 109

Figure 5.4. SEM images of $[Ni_{1/3}Co_{2/3}](NO_3)_2$/PTFE-dipped and pre-heat-treated electrode... 110

Figure 5.5. Galvanostatic cycling at 10 mA cm^{-2} for thin-nickel foam-based air electrode with $NiCo_2O_4$ catalyst. 115

Figure 5.6. Galvanostatic cycling at 10 mA cm^{-2} for thin-nickel foam-based air electrode with Co_3O_4 catalyst. 117

Figure 5.7. Galvanostatic cycling potentials for thin-nickel foam-based air electrode with Co_3O_4 catalyst at 20 mA cm^{-2} and 50 mA cm^{-2}. 119

Figure 5.8. Initial ORR potential vs. Zn and cycle-life of thin nickel foam-based air electrodes at 20 mA cm^{-2} with the following three preparation factors: pre-heat/no pre-heat, calcination temperature/time, duration of heat-treatment after PTFE soaking. 121

Figure 5.9. Initial ORR potential vs. Zn and cycle-life of thin nickel foam-based air electrodes at 20 mA cm^{-2} with the following two preparation factors: $Co(NO_3)_2$ concentration of precursor mixture for electrode dipping and dip/pre-heat-treat/calcine sequence. 124

List of Tables

Table 3.1. Strategies for improving Zn electrode performance. 46

Table 3.2. Performance metrics of selected Zn electrodes disclosed in the literature. 47

Table 4.1. Galvanostatic Cycling Procedure for Nickel-Based Gas Diffusion Electrode..... 70

Table 4.2. Galvanostatic Cycling and EIS Procedure for Nickel-Based Gas Diffusion Electrode. 72

Table 4.3. Cyclic Potentiodynamic Polarization Procedure for the Nickel-Based Gas Diffusion Electrode (GDE) and Thin-Layer Electrode (TLE). 73

Table 5.1. Preparation parameters for the investigated thin nickel foam-based air electrodes.. 101

Table 5.2. Galvanostatic cycling procedure at 10 mA cm^{-2} for thin nickel foam-based electrode. 102

Table 5.3. Galvanostatic cycling procedure at 20 mA cm^{-2} for thin nickel foam-based electrode. 103

Table 5.4. Galvanostatic cycling procedure at 50 mA cm^{-2} for thin nickel foam-based electrode. 103

Table 5.5. Basic physical properties of the thin nickel foam-based air electrode compared to the thick nickel-based air electrode from **Chapter 4**. 112

Table 5.6. Means and variances of initial ORR potential (vs. Zn at 20 mA cm^{-2}) for thin nickel foam-based electrodes grouped by the following three preparation factors: pre-heat/no pre-heat, calcination temperature/time, duration of heat-treatment after PTFE soaking. 122

Table 5.7. Three-factor ANOVA of initial ORR potential statistics in **Table 5.6**..... 122

Table 5.8. Means and variances of cycle-life (at 20 mA cm^{-2}) for thin nickel foam-based electrodes grouped by the following three preparation factors: pre-heat/no pre-heat, calcination temperature/time, duration of heat-treatment after PTFE soaking. 123

Table 5.9. Three-factor ANOVA of cycle-life statistics in **Table 5.8**. 123

Table 5.10. Means and variances of initial ORR potential (vs. Zn at 20 mA cm^{-2}) for thin nickel foam-based electrodes grouped by the following two preparation factors: $Co(NO_3)_2$ concentration of precursor mixture for electrode dipping and dip/pre-heat-treat/calcine sequence. 125

Table 5.11. Two-factor ANOVA of initial ORR potential statistics in **Table 5.10**..... 125

Table 5.12. Means and variances of cycle-life (at 20 mA cm^{-2}) for thin nickel foam-based electrodes grouped by the following two preparation factors: $Co(NO_3)_2$ concentration of precursor mixture for electrode dipping and dip/pre-heat-treat/calcine sequence. 126

Table 5.13. Two-factor ANOVA of cycle-life statistics in **Table 5.12**. 126

Table 5.14. Means and variances of initial ORR potential (vs. Zn at 20 mA cm^{-2}) for thin nickel foam-based electrodes prepared using 15 wt.% and 30 wt.% PTFE emulsions for outer PTFE-coating. 127

Table 5.15. Two-sample two-tail t-test assuming unequal variance of initial ORR potential statistics in **Table 5.14**. 127

Table 5.16. Means and variances of cycle-life (at 20 mA cm^{-2}) for thin nickel foam-based electrodes prepared using 15 wt.% and 30 wt.% PTFE emulsions for outer PTFE-coating. 127

Table 5.17. Two-sample two-tail t-test assuming unequal variance of cycle-life statistics in **Table 5.16**..... 128

Table 5.18. Nominal voltage and air electrode, separator and electrolyte properties used for **Equations 5.1-5.5**..... 129

Table 5.19. Zinc electrode properties (from **Table 3.2**) and calculation of specific energy and energy density of rechargeable zinc-air batteries containing each zinc electrode paired with a thin nickel foam-based air electrode in an energy-dense configuration. 131

List of Abbreviations

AFC – Alkaline fuel cell

AL – Active layer

ANOVA – Analysis of variance

CE – Counter Electrode

EV – Electric vehicle

FCEV – Fuel cell electric vehicle

GDL – Gas diffusion layer

ICEV – Internal combustion engine vehicle

OER – Oxygen evolution reaction

ORR – Oxygen reduction reaction

PTFE - Polytetrafluoroethylene

RE – Reference electrode

SEM – Scanning electron microscopy

WE – Working electrode

XPS – X-ray photoelectron spectroscopy

XRD – X-ray diffraction

Chapter 1: Introduction

1.1 Motivation

Increasing energy demand in combination with volatile energy prices and climate change awareness has accelerated the transition from fossil fuels to renewable energy. However, even with the levelized energy cost for renewable energy sources approaching or headed below that of fossil fuels, their intermittent nature remains a challenge to widespread adoption in the global energy mix.[1,2] With this in mind, the task of developing new energy storage systems is more urgent than ever. Batteries, which operate by storing and converting chemical energy into electrical energy, are a well-known solution. One of their biggest advantages over traditional forms of energy storage is the ability to be scaled down to small sizes, which has made them indispensable for portable electronic devices.

Electric vehicles (EVs), which are expected to replace internal combustion engine vehicles (ICEVs) in the coming years, are another industry where batteries have the potential to be the dominant form of energy storage. Most EVs today use lithium (Li)-ion batteries, which have dominated the rechargeable battery market since their advent in the late 1990s. The main disadvantages of Li-ion batteries are their high cost and concerns regarding both their safety and the supply of Li and cobalt (Co) (the latter of which is most commonly used in the positive electrode). Their energy density is also limited by the fundamental capacity of the electrode materials.[3,4] As a result, some believe that widespread consumer adoption of EVs could still be decades away due to the issues of range anxiety and high upfront cost.[5–7]

Metal-air batteries display considerably high energy densities, because oxygen (O_2) is used as the reactant at the positive electrode and is stored outside of the battery until it is discharged. Primary and secondary metal-air batteries with metals such as Li, potassium (K), sodium (Na), magnesium (Mg), aluminum (Al), zinc (Zn) and iron (Fe) have attracted much attention.[8–11] The theoretical specific energies (i.e. gravimetric energy densities), volumetric energy densities and nominal cell voltages of various metal anodes in metal-air batteries are shown in **Figure 1.1**. For secondary metal-air batteries, Li metal has received the most attention in academia since it has the highest theoretical specific energy (5928 Wh kg^{-1}) and a high cell voltage (nominally 2.96 V). However, Li in the metallic form is plagued by its inherent instability when exposed to air and aqueous electrolytes.[12] Mg and Al-air batteries are both compatible with aqueous electrolytes and have energy densities comparable to Li-air; however, their low reduction potentials typically lead to rapid self-discharge and poor coulombic charging efficiency.[8] Zn and Fe are more stable and can be charged more efficiently in aqueous electrolytes; out of these two, Zn is more promising due to its greater energy and cell voltage within an aqueous metal-air battery. Zn metal within a metal-air battery has a high volumetric energy density (6136 Wh L^{-1}) comparable to that of Li-air; this is particularly desirable for EVs due to the limited volume for mounting the batteries.[13] Moreover, the inherent safety of Zn means that Zn-air batteries can be employed with relatively little protective components and placed in the front hood of an automobile, where provision for air access is already well established in today's vehicles.

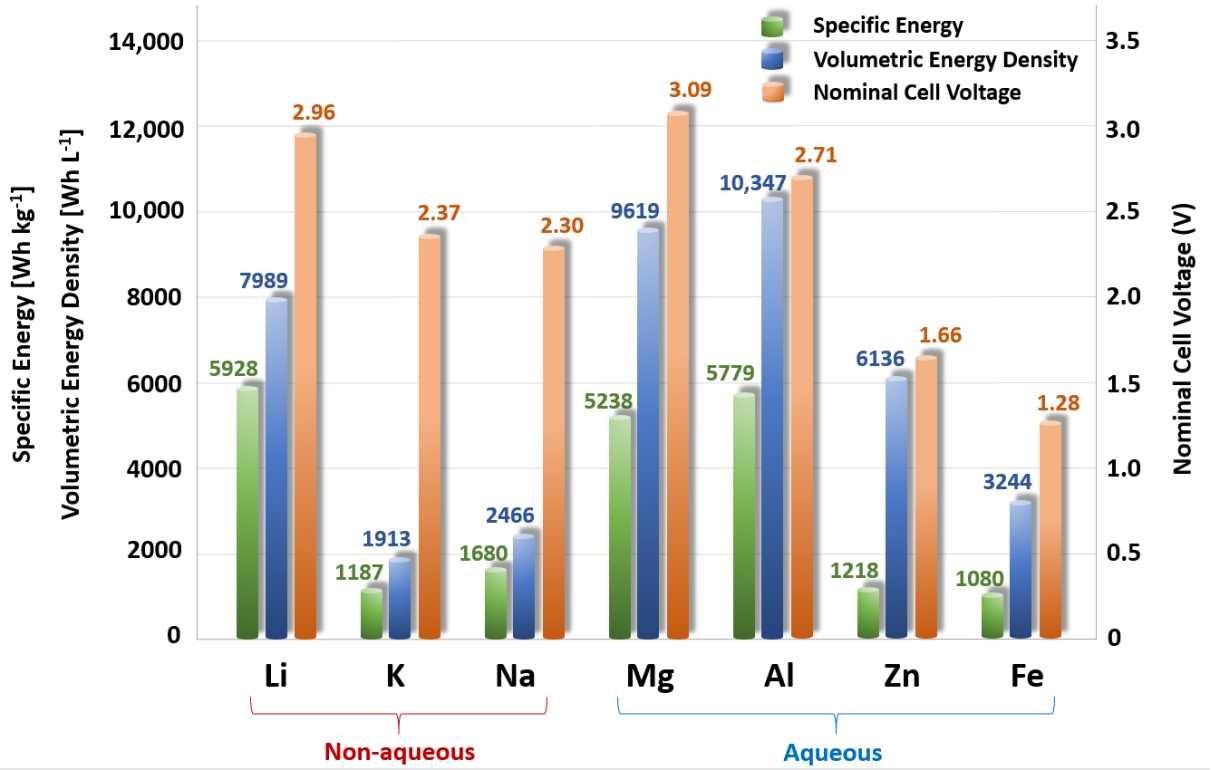

Figure 1.1. Theoretical specific energies, volumetric energy densities and nominal cell voltages for various metal anodes in aqueous and non-aqueous metal-air batteries. Specific energy values account for O_2 uptake in the battery by numeric integration between the fully charged and fully discharged states. Volumetric energy densities were calculated using the density of the anode in the fully discharged state. (Refer to the Appendix for calculations and further explanations.)

Due to its low cost, high capacity and safe nature, zinc is the most common anode material in primary metal-air batteries, which are often better known as disposable hearing-aid batteries. Rechargeable Zn-air batteries for EVs were heavily investigated by the industry between circa 1975-2000,[14–27] but the rise of lithium-ion batteries likely caused a pause in these efforts until around the start of this decade. EOS Energy Storage, NantEnergy (formerly Fluidic Energy) and ZincNyx have recently introduced flowing electrolyte-based Zn-air systems which claim to offer

lower costs than lithium-ion batteries due to the use of more inexpensive materials and less need for safety design considerations.[28–30] However, no electrically rechargeable zinc-air batteries with a static electrolyte, which are most appropriate for EV applications due to their higher energy density, have yet reached the market.

Despite their compelling cost and energy density advantages, electrically rechargeable Zn-air batteries are unlikely to fully replace Li-ion batteries in EVs within the foreseeable future. This is because of their relatively low energy efficiency (70% or less) and limited cycle life (hundreds of full charge-discharge cycles at most).[31] However, Zn-air batteries have recently been proposed as a range-extender in EVs containing both Li-ion and Zn-air battery packs.[32,33] In this concept, the Li-ion battery is designed to provide enough capacity for a relatively short driving distance (for example: 100 km, which a typical U.S. driver only surpasses approximately 15 days per year[34]). The high-capacity Zn-air battery pack in this concept is only activated when the Li-ion battery's state of charge falls below a specified value on long-range vehicle trips. This dual-battery operation thus takes advantage of the high cycle life and energy efficiency of a relatively low-capacity Li-ion battery, while also benefitting from the high energy density and cost-effectiveness of a high-capacity Zn-air battery. An EV with a dual-battery pack as such could offer an enticing combination of a relatively low price and a high driving range, which is not currently available in the market. The end-goal of this research thus lies in contribution to the development of an electrically rechargeable Zn-air battery suitable for use in EV applications.

1.2 Thesis Objectives and Structure

The objectives of this thesis are to (i) evaluate the specific opportunities and scientific challenges for zinc-air batteries to improve the performance of electric vehicles, (ii) contribute to the understanding of air electrode design issues for this application, and (iii) develop and demonstrate a new air electrode design that closes the technological gap needed to achieve a durable and energy-dense electrically rechargeable battery. **Chapter 2** places zinc-air batteries in the context of other commercial and emerging rechargeable batteries and hydrogen fuel cells, thus highlighting their specific strengths and most likely technological role in enabling new electric vehicle markets. **Chapter 3** provides a detailed overview of the scientific mechanisms and issues associated with rechargeable zinc-air batteries, with a specific focus on the material research directions needed to obtain durable and energy-dense cell designs. **Chapter 4** aims to close an identified research gap by investigating the performance and uncovering the failure mechanism of corrosion-resistant nickel-based air electrodes for rechargeable zinc-air batteries. Next, **Chapter 5** details a new thin nickel foam-based air electrode design which mitigates and withstands the nickel oxidation issue identified in the previous chapter, and also can more easily enable a high-energy density zinc-air battery in comparison to previously reported nickel-based electrode designs. Finally, **Chapter 6** summarizes the major findings from each chapter and offers some future research suggestions which should aid in the further development of energy-dense rechargeable zinc-air batteries.

Chapter 2: Evaluation of Batteries and Fuel Cells for Emerging Electric Vehicle Markets

2.1 Introduction

Although first introduced as early as the 1800s,[35] electric vehicles (EVs) have only begun to experience significant adoption since the start of the present decade. Global EV sales have escalated from less than 10,000 in 2010 to 774,000 in 2016, surpassing a total of 2 million cumulative sales.[36] Vehicle electrification is now seen as the major decarbonization pathway for nearly all road-based transportation.[37] Worsening urban air quality has also led several countries to announce intentions to ban sales of internal combustion engine vehicles (ICEVs),[38] which will need to be replaced by EVs.

The growing success of EVs can be attributed, from a technological perspective, to advancements in electrochemical energy storage technology. The specific energy of lithium-ion (Li-ion) batteries, which increased from approximately 90 Wh kg^{-1}_{cell} in the 1990's to over 250 Wh kg^{-1}_{cell} today,[39,40] has allowed full-size automobiles to travel sufficient distances for typical driving patterns.[41] Meanwhile, the cost of Li-ion battery packs has decreased from over 1,000 US$ kWh^{-1} to approximately 250 US$ kWh^{-1},[39,42–45] allowing EV prices to fall to a price that early adopters are willing to pay.

Figure 2.1 displays the evolution of cumulative EV sales and EV market share that is needed to conform to the International Energy Agency's scenario for limiting global temperature increase

to 1.75°C.[37] Referred to as the Beyond 2 Degrees Scenario (B2DS), this pathway calls for cumulative EV sales of 1.8 billion and an EV market share of 86% by 2060. The inset within **Figure 2.1**, displaying cumulative vehicle sales of ~2 million and a market share of 0.2% in 2016, demonstrates the extremely early stage of current global EV adoption and the large amount of future adoption that is needed. EV adoption to date has been heavily dictated by government policy instruments, such as financial incentives, sales mandates and free vehicle charging.[46,47] Although these policies are likely to spur further adoption, it could become financially unsustainable or undesirable to scale them up to the level needed to facilitate the market share prescribed in **Figure 2.1**. Moreover, it is not certain that EVs powered by Li-ion batteries will be suitable for every vehicle market due to inherent limits in their energy storage capacity, safety and achievable cost. Alternative technologies which can power EV drivetrains are therefore an important focus.

In this chapter, the potential of batteries and hydrogen fuel cells for improving the performance and reducing the cost of EVs is evaluated. First, three automotive markets which have not seen significant penetration by Li-ion powered EVs are outlined, and the energy characteristics which require improvement for EVs to succeed in these markets are discussed. Then, the properties of five battery types which are commonly discussed as candidates to power new EVs are compared and evaluated. Finally, brief status reviews of each battery as well as hydrogen fuel cells are provided and the potentials of each technology in fulfilling requirements for emerging EV markets are discussed.

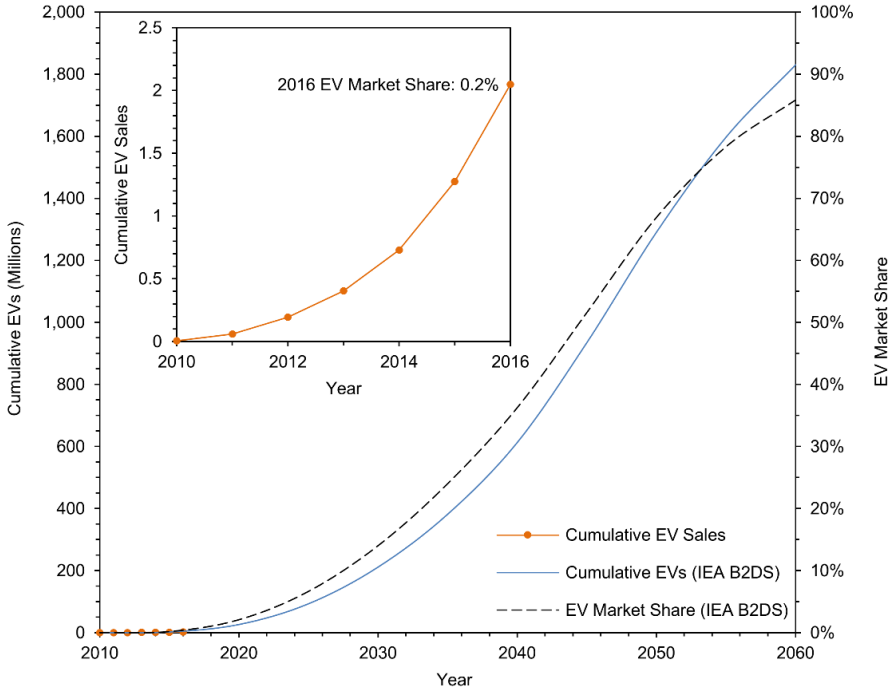

Figure 2.1. Evolution of cumulative EV sales and EV market share prescribed in the International Energy Agency's Beyond 2 Degrees Scenario. Cumulative EV sales up to 2016[36] are shown in the inset. Battery, plug-in hybrid and hydrogen fuel cell EVs are all included in these data. The Scenario data is from ref. [37].

2.2 Energy Storage Barriers in Emerging Electric Vehicle Markets

2.2.1 Long-Range Transport

Inadequate driving range, or so-called "range anxiety", is frequently reported as a key technological barrier preventing consumers from purchasing EVs.[48,49] Longer EV ranges are particularly desired in the United States,[50] which may be attributed to longer potential travel distances and less reliance on public transit than other developed regions.[51] Over one half (54%) of U.S. consumers in a 2016 survey required a range of at least 175 miles (282 km) to consider purchasing an EV, while over one quarter (29%) required a range of 375 miles (604 km).[48] When

considering an EV that could reduce fuel costs by one-third, 52% of respondents were unwilling to spend more than 5,000 US$ above a gasoline-powered vehicle, while 29% would not spend above a 1,000 US$ premium.

In **Figure 2.2**, the driving ranges for EVs currently available in the U.S. market are compared to their price premium relative to average vehicle prices in the same size segment. Notably, each EV is at least $5,000 US$ more expensive than the average vehicle price in its respective vehicle size class. While other factors such as low manufacturing volumes and extra vehicle features may contribute to high prices, the positive correlation between EV range and price premium indicates the significant cost contribution of the batteries. A range-dependent willingness-to-pay model for U.S. consumers[50] was used to expand the aforementioned consumer survey results into boundaries of requirement, where 52-54% of U.S. consumers require an EV with a price premium and range below the upper requirement boundary, while 29% of U.S consumers require an EV with a price premium and range below the lower requirement boundary. This figure shows that without government incentives, none of the currently available EVs would satisfy the requirements of over 50% of U.S. consumers.

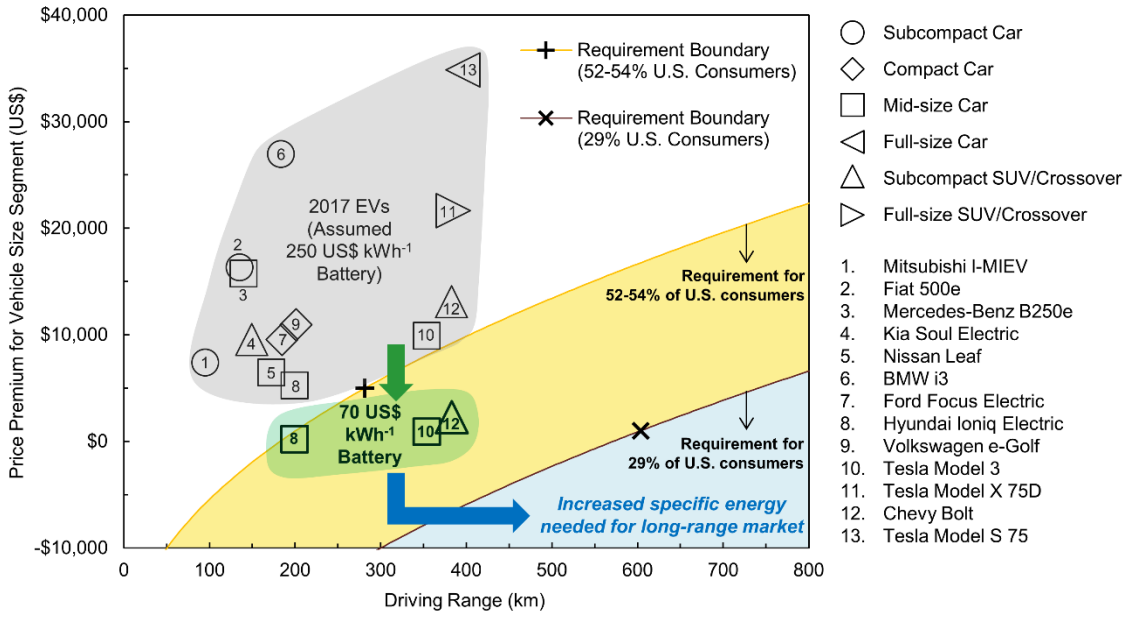

Figure 2.2. 2017 model EV ranges and price premiums. Price premiums are defined relative to average transaction price for vehicle size segment (including ICEVs and excluding luxury vehicles). Selected 2017 model EVs are also re-plotted in the green area with their price adjusted for a battery cost of 70 US$ kWh^{-1} (initial battery cost assumed to be 250 US$ kWh^{-1}). The '+' and '×' coordinates represent the range and price requirements for 52-54% and 29% of U.S. consumers, respectively.[48] These data points are expanded into requirement boundaries using a range-dependent willingness-to-pay model for U.S. consumers.[50] Note that the price premiums of luxury-class EVs were not measured relative to other luxury-class vehicles; this was chosen so that each vehicle price premium could be compared to the price requirements of typical consumers for whom cost is a primary concern. Further vehicle data provided in **Supplementary Table 1**.

Recent forecasts predict lithium-ion battery pack costs will fall to near 70 US$ kWh^{-1} by 2030 or 2040 as manufacturing efficiency is further improved.[43,52] If 2017 EV prices are adjusted to reflect this value, three models (Chevrolet Bolt, Hyundai Ioniq Electric and Tesla Model 3) appear to pass the 50% U.S. consumer requirement threshold (**Figure 2.2**). However, EVs with these adjusted prices would remain far short of meeting the requisites of nearly 30% U.S. consumers, and likely many other consumers in highly automobile-dependent countries. Even if

energy storage costs are removed from the vehicle prices, none of the current EV models would provide a driving range that 30% of U.S. consumers would be willing to pay for. Therefore, substantially improving EV ranges without increasing cost appears to be the only way to satisfy the long-range transportation market. This requires reducing vehicle weight by increasing the specific energy (Wh kg^{-1}) stored in the vehicle. However, with Li-ion batteries, substantially increasing the specific energy likely requires metallic lithium anodes, increased cell voltages or reduced safety components, all of which may involve an unacceptable trade-off for safety.[53–55] Solid-state Li-ion batteries are one of the most promising pathways for safely incorporating lithium metal and higher voltage materials; however, reported cells to date have either unacceptably low areal capacities (less than 1 mAh cm^{-2}, which would translate to lower specific energy than state-of-the-art Li-ion batteries[56]) or unacceptably low cycle life (20 cycles or less).[57] Even a highly optimized Li-ion cell with a lithium metal anode may not practically surpass 350 Wh L^{-1}_{cell}.[56] Consequently, alternative battery chemistries and energy storage technologies with higher specific energy, lower cost and improved safety are needed to enable electrification of the long-range transportation market.

2.2.2 Low-Cost Transport

The cost of EVs, as opposed to their range, is likely the primary concern for a large, increasing percentage of future vehicle owners. **Figure 2.3** displays results of a discrete choice model fitted to vehicle registration data (for both EVs and conventional vehicles) from a selection of countries.[58] U.S. consumers were willing to pay an additional 21 US$ per one additional kilometre of range (21 US$ km^{-1}), while consumers in emerging countries (China, India, Brazil

and Indonesia) were only willing to pay an average of 8.4 US$ km^{-1}. **Figure 2.3** also displays the negative logit coefficient for vehicle price fitted to each country, which measures the degree to which a price increase reduces the probability a consumer will purchase a vehicle.[58,59] The negative coefficient for emerging countries was, on average, significantly higher than that of the U.S. China was the one exception, with a negative value indicating that a higher price surprisingly increased the probability of a vehicle purchase. Nevertheless, high Chinese sales figures for cheaper and smaller low speed EVs, two-wheelers and three-wheelers versus those for conventional EVs (over 200 million vs. 0.6 million in total as of 2016[47]) indicate the high market desire for low-cost transportation in China alongside India, Brazil and Indonesia.

EVs available in emerging markets such as China have a similar price premium to the developed countries.[60] The low-cost transportation market, which is expected to grow quickly as emerging countries continue to industrialize, is thus underserved by current Li-ion powered EVs. If the battery energy of the compact and subcompact cars in **Figure 2.2** are plotted against vehicle ranges, a slope of 0.19 kWh km^{-1} (representing energy consumption per additional kilometre of range) is obtained. The average willingness to pay for emerging countries (8.4 \$ km^{-1}) is divided by 0.19 kWh km^{-1} to obtain an energy storage cost target of approximately 45 US$ kWh^{-1}. Development of an electrochemical storage technology costing below 45 US$ kWh^{-1} is therefore a worthwhile goal for enabling electrified transportation in emerging markets. Alternatively, technologies with a higher specific energy and similar cost to Li-ion batteries can also help this market by reducing the energy consumption value used in the above calculation.

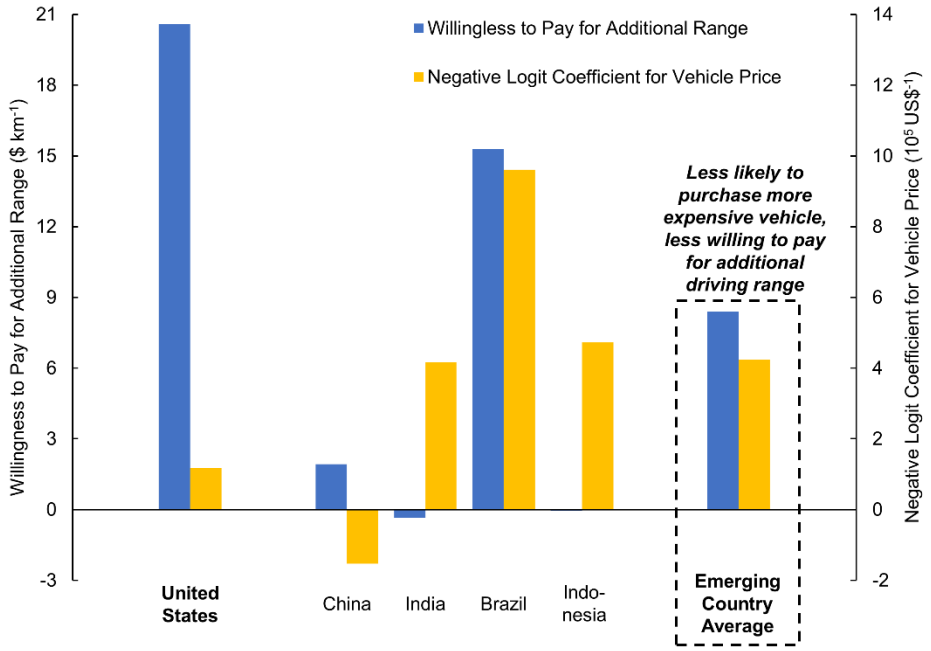

Figure 2.3. Consumer vehicle purchasing habits in the United States versus emerging countries. Willingness to pay for additional range and the negative of the logit coefficient for vehicle price are compared for consumers in the U.S. and selected emerging countries.[58] Readers are referred to ref. 24 for the calculation methods. A higher magnitude for the negative logit coefficient indicates that an increased vehicle price causes a greater reduction of the probability a consumer will purchase the vehicle. Note that the average willingness to pay for emerging countries is not the mean of the given willingness to pay values; this was calculated from the mean logit coefficients for vehicle price and vehicle range for each emerging country.

2.2.3 High-Utilization Transport

Vehicles which experience higher utilization – i.e., the percentage of time they are in operation – than consumer vehicles are a significant contributor to climate change and poor air quality. For instance, road freight vehicles accounted for approximately one-third of carbon dioxide emissions from the global transportation industry in 2015, and this share is increasing in industrialized countries as passenger vehicles become more fuel efficient.[61] Therefore, the unique

challenges of transitioning to high-utilization EVs for public transportation and goods transportation is a crucial topic to address.

High utilization has important implications for the requirements of the energy storage technology used in EVs. Firstly, the capability for fast charging (e.g. less than one hour) becomes a more important consideration, since the time required to charge the vehicle should not disrupt the operating schedule of the vehicle. Li-ion batteries are capable of fast charging, and electric busses designed for quick partial recharging at bus stops have been deployed in several countries;[62] however, this can cause enhanced cell degradation and safety issues.[63–65] Simultaneous fast-charging of several EVs can also put excessive stress on the components of power grids, thus necessitating expensive upgrades.[66,67] Therefore, an important aspect to consider for high-utilization EVs is their ability to quickly recharge while smoothly integrating with power grids.

Another key characteristic of many high-utilization vehicles such as trucks, busses and trains is their larger weights relative to personal transport vehicles. Li-ion battery packs must be proportionally scaled to larger sizes for these vehicles to travel an equivalent distance. However, the lower surface-to-volume ratios of larger battery packs means that heat dissipation is slower, often resulting in increased degradation and safety concerns and the need for complex cooling techniques with expensive or toxic chemicals.[63] Therefore, energy storage and conversion technologies which have higher specific energies and safer characteristics (e.g. non-flammable materials) are particularly attractive for high-utilization EVs.

2.3 Evaluation of Electrochemical Technology Candidates

The previous section specified that increased specific energy or lower energy storage cost (in comparison to Li-ion batteries) is essential for EVs with longer driving ranges and lower cost, while fast-charging, power grid compatibility and safe operation are crucial for high-utilization EVs. Of course, Li-ion batteries possess several other characteristics which other electrochemical technologies need to compete with. Characteristics of the technologies regarded as candidates for new EVs, in addition to those of Li-ion batteries, are compared in **Figure 2.4**. Qualitative safety ratings were determined by the type of electrolyte (flammable or non-flammable), potential for over-heating, and potential for toxic or corrosive material release. Fast-charging capability for each battery was rated semi-quantitatively from its specific power, while each battery's power grid compatibility was rated semi-quantitatively from its energy efficiency. Hydrogen fuel cells have the highest fast-charging and power grid compatibility due to the ability to quickly transfer hydrogen gas without disrupting power grids.

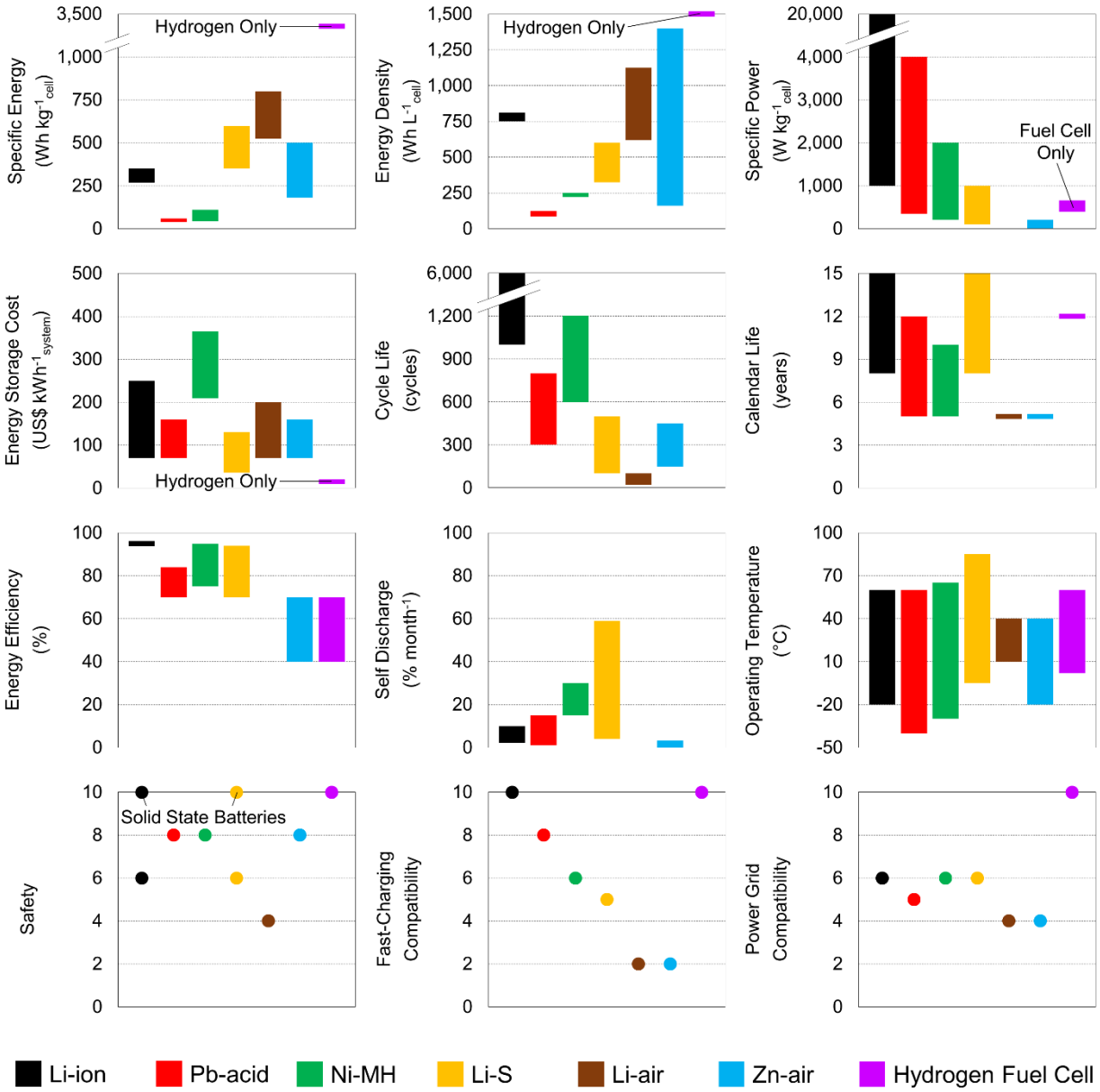

Figure 2.4. Characteristics of rechargeable batteries and hydrogen fuel cells. The upper bounds of the specific energy, energy density and specific power ranges represent estimates of what can be practically achieved (refer to references in **Supplementary Table 2** for details), while the lower bounds indicate what has already been achieved (vice versa for energy storage cost). Cycle life, calendar life, energy efficiency, self-discharge and operating temperature ranges represent upper and lower values observed in commercial or prototype cells. Energy storage cost refers to the cost of the battery pack or system, while specific energy, energy density and specific power refer to cell-level values. Energy storage cost refers to the cost of the battery pack or system,

while specific energy, energy density and specific power refer to cell-level values. Literature information was not sufficient to confidently specify upper and lower bounds/values for the specific power, energy efficiency and self-discharge rate of Li-air batteries. For hydrogen fuel cells, energy-related characteristics apply only to hydrogen within a typical hydrogen storage tank (i.e. not including the fuel cell) and specific power applies only to the fuel cell (i.e. not including hydrogen storage). Cycle life and self-discharge rates are not applicable to hydrogen fuel cells, and thus are not included. Safety, fast-charging compatibility and power grid compatibility are qualitative ratings between 0 (worst) and 10 (best). Separate safety ratings are assigned to the solid-state versions of lithium-based batteries due to the replacement of flammable, liquid electrolytes with solid, non-flammable electrolytes. Numeric values and references for each characteristic are provided in **Supplementary Table 2**.

Note that the energy characteristics of hydrogen storage in **Figure 2.4** (specific energy, energy density and energy storage cost) should not be directly compared to those of the various battery chemistries without accounting for the mass, volume and cost of a coupled fuel cell system. Unlike batteries, the total energy of a hydrogen fuel cell combination (i.e. amount of stored hydrogen) can be increased separately from the total power of the fuel cell. Due to this fundamental difference, hydrogen fuel cells are not included in the analysis below; they are evaluated relative to Li-ion batteries in a separate section.

Certain metrics for the batteries in **Figure 2.4**, namely specific energy, energy density and energy storage cost, can be evaluated more practically by using them in approximating calculations of vehicle range (R_V), total vehicle cost ($C_{V,T}$) and battery pack volume (Vol_B). Each of these are a function of the battery pack energy (E_B), and can be calculated from **Equation 2.1**,[68] **Equation 2.2** and **Equation 2.3** respectively:

$$R_V = \frac{E_B}{ECE_V\left(W_V + \frac{E_B k_{w,B}}{SE_{BC}}\right)} \quad \textbf{(Equation 2.1)}$$

$$C_{V,T} = C_v + C_B E_B \quad \textbf{(Equation 2.2)}$$

$$Vol_B = \frac{E_B \times k_{vol,B}}{ED_{BC}} \quad \textbf{(Equation 2.3)}$$

where ECE_V (Wh km^{-1} kg^{-1}) is the energy consumption efficiency of the vehicle, W_V and C_V are the vehicle weight and vehicle cost not including the battery pack, C_B is the battery pack cost, SE_{BC} and ED_{BC} are the specific energy and energy density of the battery cell, and $k_{W,B}$ and $k_{Vol,B}$ are factors for the battery pack weight and volume overheads, respectively. The overhead factors assigned to each battery (**Supplementary Table 2**) reflect the level of safety equipment or air management equipment (for metal-air batteries) needed to operate each battery.

Results for a mini vehicle (common in markets which demand low-cost vehicles), a midsize vehicle (common in markets demanding long-range vehicles) and a semi-trailer truck (representing the high-utilization market) are exhibited in **Figure 2.5**a,b, **Figure 2.5**c,d and **Figure 2.5**e,f respectively. Vehicle cost as a function of driving range is plotted in **Figure 2.5**a,c,e until the battery volume exceeds an assigned space limit within each vehicle. Here, the low energy densities of lead-acid (Pb-acid) and nickel-metal hydride (Ni-MH) batteries are clearly recognized as a large drawback. The potential for lithium-sulfur (Li-S), lithium-air (Li-air) and zinc-air (Zn-air) batteries to enable long-range EVs at a significantly lower cost than Li-ion batteries is also apparent. The cost of adding additional range (US\$ km^{-1}), which may be compared to investigations of consumers' willingness to pay for additional range,[50,58] is plotted against vehicle range in **Figure 2.5**b,d,f. **Figure 2.5**b shows that Li-S, Li-air and Zn-air batteries can bring the cost of additional range of a mini vehicle substantially closer to the average willingness to pay value for emerging countries identified in **Figure 2.3**.

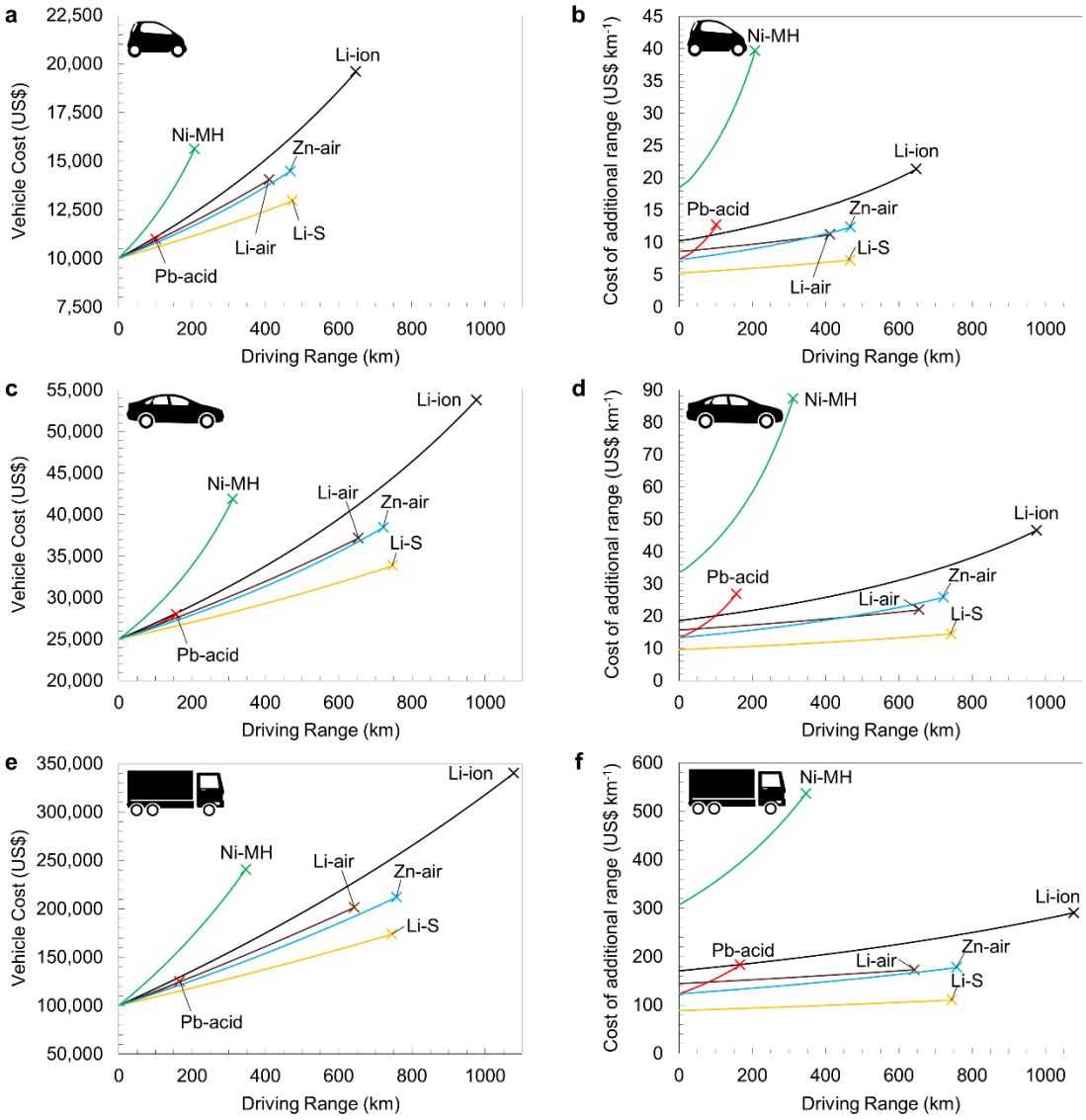

Figure 2.5. Vehicle cost and cost of additional range as a function of driving range. Curves are plotted for (a,b) mini vehicle (C_V = 10,000 US$, W_V = 650 kg, ECE_V = 0.0985 Wh km^{-1} kg^{-1} (**Supplementary Table 1**)), (c,d) midsize vehicle (C_V = 25,000 US$, W_V = 1500 kg, ECE_V = 0.0777 Wh km^{-1} kg^{-1} (**Supplementary Table 1**)) and (e,f) semi-trailer truck (C_V = 100,000 US$, W_V = 24,000 kg, ECE_V = 0.0445 Wh km^{-1} kg^{-1} [69]). Curves in a,c,e are calculated with **Equations 2.1** and **2.2**, and are plotted until the battery volume (**Equation 2.3**) exceeds a chosen maximum. Curves in b,d,f are plotted by calculating the respective tangents of curves from **a,c,e**. Midpoint values of the specific energy, energy density, energy storage cost and battery system overhead ranges (**Figure 2.4**, **Supplementary Table 2**) were used for each curve.

Figure 2.6 displays the approximate span of vehicle cost and range combinations which could be achieved for a midsize vehicle using the upper and lower bounds of the energy and cost characteristics of each battery in **Figure 2.4**. It can be seen here that Zn-air batteries have the potential to enable the longest range EV, while Li-S batteries could enable the lowest cost EV. However, this evaluation does not dictate whether each battery has sufficient power, cycle/calendar life, efficiency, and self-discharge rate to function reliably in an EV. Therefore, Figures 5 and 6 only demonstrate the basic potential of each battery chemistry to lower costs and increase driving ranges. Details regarding the practicality of implementing these technologies in consumer, commercial and public transportation applications are discussed below.

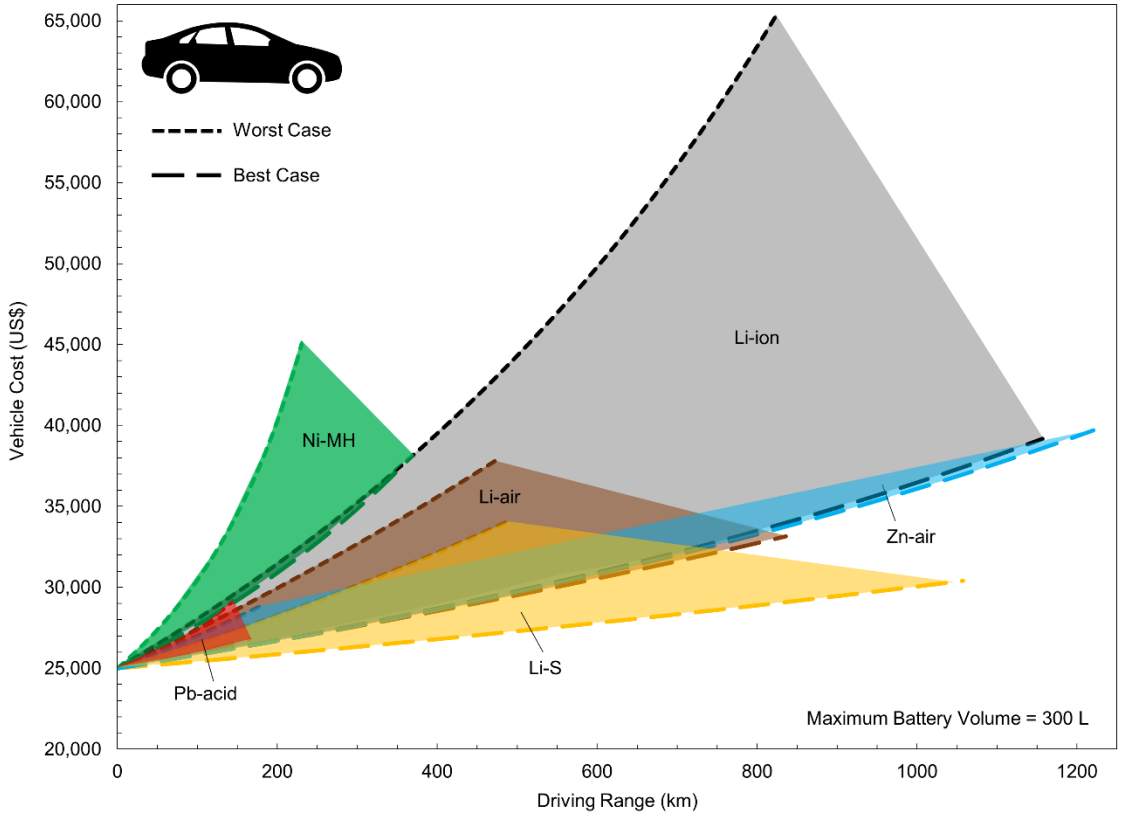

Figure 2.6. Sensitivity plots of midsize vehicle cost and range. Curves show sensitivity to minimum specific energy, minimum energy density, maximum cost and maximum system overheads (defined as the worst-case characteristics) and maximum specific energy, maximum energy density, minimum cost and minimum system overheads (defined as the best-case characteristics) for each battery. The area between the two curves shows the span of possible costs and driving ranges that could be enabled by each battery.

2.3.1 Commercial Rechargeable Batteries

2.3.1.1 Lead-acid Batteries

Pb-acid batteries are currently the lowest-cost and most-used rechargeable batteries in the world.[43,70] However, due to their low specific energy and energy density, they are only more cost-effective than Li-ion batteries for low-range EVs (**Figure 2.5**). Also, their larger volume and lower cycle life, specific power and energy efficiency tends to make them less preferred than Li-ion batteries in newer low-cost and low-speed bikes and vehicles.[71] Nevertheless, Pb-acid batteries have some advantages that make them attractive for assistive roles in vehicle electrification. Besides their low cost, these include low-temperature operation (as low as -40 °C[72]), better charging safety[73] and potentially very low self-discharge rates.[74]

Most work on Pb-acid batteries is thus now aimed at making them capable of regenerative brake charging and motor assist in hybrid vehicles.[75,76] This requires batteries which can survive up to hundreds of thousands of high-power "micro-cycles" at partial states of charge.[77] A major problem when subjecting conventional Pb-acid batteries to high discharge rates is irreversible growth of large, insulating lead sulphate crystals on the negative electrode, which subsequently harms its ability to accept fast recharges.[76] Various carbon additives were discovered to mitigate this problem by improving conductivity, promoting smaller sulphate crystal growth, and introducing capacitive behaviour to buffer high charge and discharge rates.[75,78] These "Pb-carbon" batteries have shown promise in low-cost hybrid EV concepts,[79] and with further power improvements, could be attractive for fully electrified low-cost vehicles with dual energy sources.

2.3.1.2 Nickel-Metal Hydride Batteries

The Ni-MH battery, commercially introduced in 1989, is the most common nickel-based battery and offers significantly better performance than Pb-acid batteries across most metrics.[80] They were the default battery choice for hybrid EVs until very recently, and therefore the technology is already well-optimized for regenerative brake charging and full-electric traction.[77] However, the higher cost of nickel and hydride storage metals also makes them more expensive than Pb-acid batteries; in fact, they are now more expensive than Li-ion batteries following the latter's rapid cost reduction.[43]

Since Li-ion batteries have higher specific energy, energy density and cycle life, while Pb-acid batteries are cheaper, Ni-MH batteries do not appear to provide any distinct advantages for emerging EV markets. However, the aqueous electrolyte and lower reactivity metals used in Ni-MH batteries makes them inherently safer to operate, while their better low temperature performance could make them useful for vehicle start-up in cold climates.[80] Their safer operation also allows them to be placed in more impact-exposed areas of a vehicle, such as the front end, which would be too dangerous for lithium-based batteries. Substitution of structural components and energy absorption materials with Ni-MH batteries has been advocated as a creative method to reduce vehicle weight, thus offering the potential for longer range EVs.[68]

2.3.2 Emerging Rechargeable Batteries

2.3.2.1 Lithium-sulfur Batteries

Li-S batteries have received elevated attention owing to the 4.5 times higher theoretical lithium capacity and much lower cost of sulfur cathodes relative to typical Li-ion insertion

cathodes.[81] Unfortunately, sulfur cathodes have several challenging characteristics such as high volume change upon cycling, low conductivity of the sulfur and lithium sulfide phases, and relatively high solubility of sulfur species in common lithium battery electrolytes.[81,82] These issues lead to low cycle life and high self-discharge rates, which are both problematic for EV energy storage technologies. Li-S batteries must also incorporate a lithium metal anode to provide an appreciable specific energy advantage over Li-ion batteries.[56] Lithium metal anodes have several challenges including poor cycle life and fast-charging ability (due to lithium dendrite formation and irreversible electrolyte consumption), high self-discharge (due to unwanted side reactions) and increased safety concerns for both manufacturing and operation.[55,83,84]

To address the above difficulties, researchers have reported electrodes incorporating sulfur intertwined with porous carbon or conductive polymer "containers", which inhibit sulfur dissolution while accommodating volume expansion, improving conductivity and allowing reversible lithium ion migration during charging and discharging.[81,83,85] Regarding the lithium metal anode, most strategies to reduce dendrite formation and mitigate side reactions involve protecting the anode with a passivation layer, coating, separator or solid-state electrolyte.[84] Developments such as these must result in higher cycle life and higher allowable currents without sacrificing specific energy and energy density,[86] which has proven difficult as demonstration cells in the literature thus far have not achieved more than 500 cycles at practical charge rates and specific energies.[85]

The maximum practically achievable specific energy (600 Wh kg^{-1}_{cell}) and estimated minimum cost (36 US$ kWh^{-1}) for Li-S batteries would be a significant improvement over Li-ion

batteries, making them attractive for all three emerging EV markets discussed earlier. However, unless their cycle life is substantially improved, Li-S batteries appear to be a poor choice for high-utilization EVs. A consumer vehicle that is driven long distances occasionally, on the other hand, could be practical because the battery would rarely be subjected to full discharge cycles. Very few drivers travel long distances (greater than 200 km) necessary to cause deep discharges of moderately sized Li-S batteries on a frequent basis;[41] thus, anxiety over battery degradation from frequently driving long distances should be much less likely than conventional range anxiety (i.e. inability to drive long distances). Therefore, Li-S batteries are a strong candidate to succeed Li-ion batteries in consumer EVs, since they can lower costs and reduce range anxiety at a relatively affordable cost (**Figure 2.5**).

2.3.2.2 Lithium-air Batteries

Li-air batteries offer a further improvement in specific energy and energy density above Li-S batteries due to their use of atmospheric oxygen to produce power. However, their demonstrated cycle life has thus far been much lower, with a maximum around only 100 cycles.[87,88] Improving their cycle life has proven difficult due to several issues such as air electrode clogging from lithium discharge products, catalyst degradation from high-voltage charging, lithium metal side-reactions from atmospheric moisture and irreversible electrolyte decomposition.[89,90] In addition, while reliable estimates of specific power and energy efficiency are not available for Li-air batteries, these metrics are likely to be much poorer than the previously discussed batteries due to sluggish oxygen kinetics at the air electrode.[91]

Moreover, the maximum energy density of Li-air batteries at an automotive system level has been projected to be only 384 Wh L^{-1}_{system} after accounting for equipment to protect the battery from atmospheric carbon dioxide and moisture.[92] This places a volumetric limit on the ability of Li-air batteries to enable substantially longer driving ranges than Li-ion batteries (**Figure 2.6**). On the other hand, their combined low cost and high specific energy are still attractive for long-range and low-cost consumer EVs (**Figure 2.5**). Unlike Li-S batteries, however, Li-air batteries would require a complimentary high-power battery for practical operation due to their likely poor specific power.

2.3.2.3 Zinc-air Batteries

Zn-air batteries, despite having a lower specific energy relative to Li-air batteries, are more likely to be used in future EVs due to their greater laboratory progress thus far (i.e. higher demonstrated cycle life and current operability) and higher practically-achievable energy density.[93] Rechargeable Zn-air batteries were identified as a promising candidate for vehicle electrification in the decades prior to the emergence of Li-ion batteries.[94] Similarly to Li-air batteries, their poor specific power and energy efficiency, as well as relatively poor cycle life compared to lithium-ion batteries, will likely prevent them from being used as a primary energy source for EVs; however, they could be promising when used in a dual-battery configuration. They could be combined with high-power Pb-carbon batteries to produce a low-cost EV,[95] although they would likely need a higher cycle life to provide a long vehicle lifetime. Alternatively, they could be implemented as range-extenders for an EV primarily powered by Li-ion batteries, in order to enable long-range EVs; this makes their short cycle life and low efficiency relatively

unimportant, assuming the driver only occasionally needs to travel long distances.[96] While dual-battery concepts can significantly increase cost and complexity,[97] the inherent safety of Zn-air batteries[25,98] also makes them well-suited for a dual-battery configuration because (similarly to Ni-MH batteries) there are fewer constraints in their physical location within a vehicle.

2.3.3 Hydrogen Fuel Cells

Hydrogen is an energy carrier that can be produced from low-carbon sources and stored with a high specific energy relative to most batteries (**Figure 2.4**). Therefore, hydrogen fuel cells have been targeted for their potential to contribute to decarbonization in the transportation sector.[99,100] The first mass-produced fuel cell electric vehicles (FCEVs), which use polymer electrolyte membrane (PEM) fuel cells, were introduced in 2013-2014 by Hyundai, Toyota and Daimler. The advantages of these vehicles relative to current battery electric vehicles (BEVs) include higher driving ranges (over 500 km) and faster refuelling (3-5 minutes to re-fill the hydrogen storage tank). However, cumulative FCEV deployments represent a small fraction of total EV sales through 2016 (less than 10,000[101,102] or 0.5%), and they must overcome several challenges to achieve significant market uptake.

FCEVs have higher purchase prices than conventional vehicles, and similarly to BEVs, this is attributed to their electrochemical power supply. The hydrogen storage tank and fuel cell system are the most expensive components due to the inclusion of expensive materials and equipment such as platinum, carbon fibre, humidifiers and heat exchangers.[103–105] The cost of nearly all these components will significantly decline with increased manufacturing volumes, with the main exception being platinum group metal (PGM) catalysts due to their scarcity. To reach a similar

total PGM content to ICEVs, FCEVs must reduce PGM loadings to approximately one quarter of their current state-of-the-art levels.[106] This highlights the importance of research efforts to develop catalysts with reduced levels of PGMs and improved efficiency and durability.[107–109]

Cost comparisons for BEV and FCEV versions of an electric midsize vehicle and an electric semi-trailer truck are displayed in **Figure 2.7**a and **Figure 2.7**b, respectively. The range and cost of the conventional FCEV and the total volume of its energy storage and conversion system were approximated by adapting **Equations 2.1-2.3**, with the hydrogen consumption efficiency replacing the energy consumption efficiency and the extra mass, volume and cost of the hydrogen tank and fuel cell system accounted for. The resulting equations for FCEV range, total vehicle cost and the total volume of its battery pack, fuel cell system and hydrogen tank (the former necessary for supplemental power) are provided in **Equations 2.4, 2.5 and 2.6** respectively:

$$R_V = \frac{M_{H2}}{HCE_V\left(W_V + \frac{E_B k_{w,B}}{SE_{BC}} + M_{H2} + M_{FC}P_{FC} + M_{HT}\right)} \quad \textbf{(Equation 2.4)}$$

$$C_{V,T} = C_v + C_B E_B + C_{FC}P_{FC} + C_{HT}SE_{H2}M_{H2} \quad \textbf{(Equation 2.5)}$$

$$Vol_{B,FC,HT} = \frac{E_B \times k_{vol,B}}{ED_{BC}} + V_{FC} + V_{HT} \quad \textbf{(Equation 2.6)}$$

where M_{H2} is the mass of stored hydrogen, HCE_V (kg_{H2} km^{-1} kg^{-1}) is the hydrogen consumption efficiency of the vehicle, SE_{H2} is the specific energy of hydrogen, M_{FC}, P_{FC}, C_{FC} and V_{FC} are the mass, power, cost and volume of the fuel cell system and M_{HT}, C_{HT} and V_{HT} are the mass, cost and volume of the hydrogen tank, respectively (refer to **Supplementary Table 3** for details). FCEV costs are less sensitive to increased driving range because increasing the range only requires increasing the size, quantity or pressure of hydrogen storage tanks, which are lighter and less

expensive than Li-ion battery packs on a per-kWh basis. However, the high present cost of fuel cell systems makes current conventional FCEVs more expensive than BEVs for consumer vehicles (**Figure 2.7**a). Previous estimates projected the equal-cost crossing point for consumer FCEVs and BEVs to occur at lower driving ranges;[56,110] however, the steep decline of Li-ion battery costs in recent years and their even lower long-term projected costs have significantly increased the equal-cost point. Semi-trailer trucks, on the other hand, appear to be well suited to electrification by a fuel cell system rather than Li-ion batteries at most practical driving ranges (**Figure 2.7**b). This is particularly true when considering that the additional weight of the battery system (required to achieve long driving ranges) reduces the total payload that the battery-powered semi-trailer truck can haul.

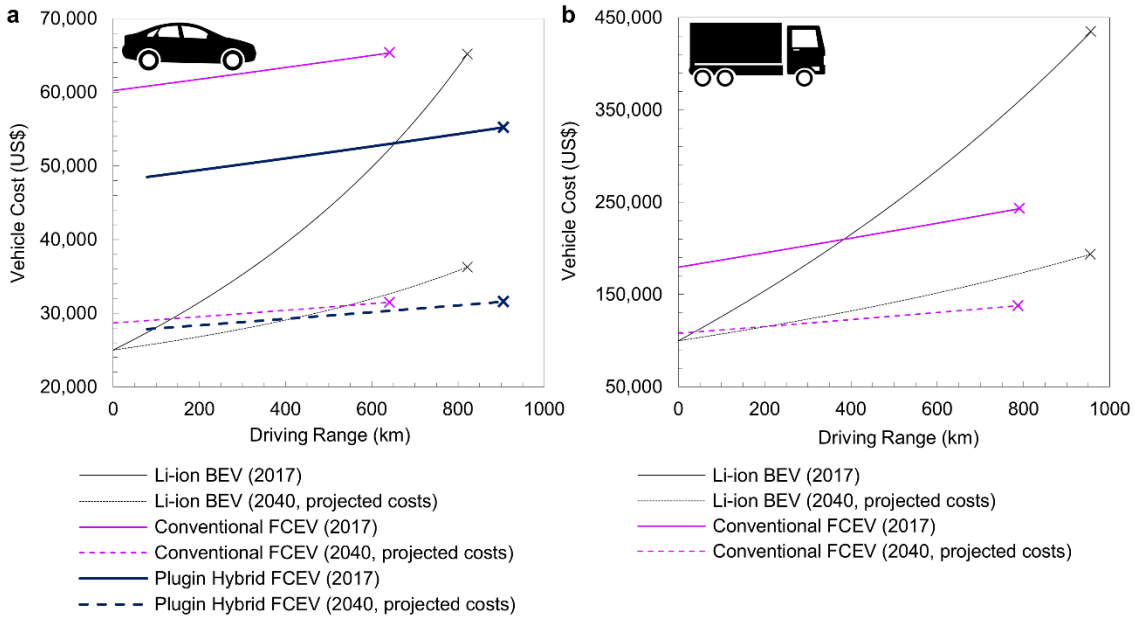

Figure 2.7. Vehicle cost as a function of driving range for Li-ion battery and hydrogen fuel cell EVs. Curves for BEVs and FCEVs plotted for (a) midsize vehicle and (b) semi-trailer truck. Curves are calculated from **Equations 2.4-2.7** using the variables in **Supplementary Table 3**. Note that the differences between 2017 and 2040 only account for projected price reductions, and do not account for specific energy improvements of Li-ion batteries nor specific power and efficiency improvements of hydrogen fuel cells. Minimum values of specific energy and energy density and maximum values for energy storage cost and overhead factors (**Supplementary Table 2**) were used for the Li-ion batteries in each vehicle. The '×' on each curve indicates the point at which the total volume of the battery pack, hydrogen tank and fuel cell system surpasses 300 L (midsize vehicle) or 2,500 L (semi-trailer truck).

Some new FCEVs incorporate a larger Li-ion battery that provides (i) pure battery-powered propulsion for short-range trips and (ii) greater power-assisting to the fuel cell, which allows for a smaller fuel cell system.[111] The range of these plug-in hybrid FCEVs may be approximated with **Equation 2.7**, which were adapted from a combination of **Equations 2.1** and **2.4**:

$$R_V = \frac{E_B}{ECE_V\left(W_V + \frac{E_B k_{w,B}}{SE_{BC}} + M_{H2} + M_{FC}P_{FC} + M_{HT}\right)} + \frac{M_{H2}}{HCE_V\left(W_V + \frac{E_B k_{w,B}}{SE_{BC}} + M_{H2} + M_{FC}P_{FC} + M_{HT}\right)}$$

(**Equation 2.7**)

Plotting **Equation 2.7** as a function of stored hydrogen mass (other parameter assumptions in **Supplementary Table 3**) results in lower vehicle costs and significantly longer achievable ranges due to the smaller size of the fuel cell system (**Figure 2.7**a). Using long-term projected costs and 800 km of range, a midsize plug-in hybrid FCEV could be 5,000 US$ less expensive than a midsize Li-ion BEV and 6,000 US$ more expensive than an average midsize ICEV, making them more attractive to a sizeable portion of U.S. consumers (**Figure 2.2**). Hybrid FCEV trucks enabling ranges of nearly 2,000 km are also in development.[112]

A more significant barrier to FCEV adoption is the current lack of infrastructure for hydrogen transportation and distribution.[100,113] The capital cost of a hydrogen refilling station (including hydrogen delivery or on-site production) can range from 1 to 10 million US$,[114,115] which is significantly larger than that for an EV fast-charging station (less than 0.2 million US$[116]). Therefore, in the near-term, FCEVs and hydrogen infrastructure development are best suited to the high-utilization commercial vehicle sector, where a small number of strategically located hydrogen stations could service pre-planned high-utilization driving routes to justify their high investment cost.[100] However, at large scales it may actually be more expensive to upgrade the electrical grid to accommodate the charging demands of BEVs vs. installing a hydrogen refuelling network.

Another consideration for significant FCEV adoption is their energy efficiency relative to batteries. The entire "green mobile hydrogen cycle", which includes storing energy as hydrogen gas via electrolysis of water, compression (and transportation if necessary) of the hydrogen gas, and conversion of hydrogen back to power in a FCEV is typically around 25-30% efficient (without heat recovery and utilization).[100,117] Industrial hydrogen is presently available with higher efficiency, albeit with higher carbon emissions.[118] For comparison, the total efficiency for charging and driving a BEV is around 80-85%,[119] meaning a FCEV could require about 2.5-3.5 times more energy from the power grid to drive the same distance. However, the full cost comparison between FCEV and BEV operation must include (i) the cost of upgrading the current power grid versus building a hydrogen infrastructure and (ii) how excess energy, required to meet peak demand, will be stored during times of low electricity demand. One such study of the United Kingdom indicated that an "electrification" strategy relying only on electricity for powering end-use technologies (such as BEVs) would be ~ 3 times more expensive than a "full contribution" model in which hydrogen is the primary energy carrier for end-use technologies.[120] It should also be noted that alkaline electrolysis combined with hydrogen storage has the lowest capital costs of any other commercialized utility-scale technology, on a per-kWh basis.[43]

Finally, the durability of PEM fuel cells is an important factor to be considered for their potential success.[121,122] Particularly for the high-utilization market, a significant challenge for PEM fuel cells is to demonstrate high enough durability to achieve a similar lifetime to incumbent ICEVs. Encouragingly, two PEM fuel cell-powered buses (one of which utilizes Ballard's FCveloCity®-HD6 module) have recently achieved over 25,000 h of operation,[123,124] which is

equivalent to 4 to 6 years and meets the U.S. Department of Energy and Federal Transit Administration targeted lifetime for a fuel cell powertrain.[125] Consumer FCEVs are also near their target of 5,000 hours of operation,[126] while plugin-hybrid FCEVs can provide greater reliability due to optimized power shifting between the fuel cell and a larger battery.[111]

2.4 Conclusions

Batteries and fuel cells with improved specific energy, energy density, cost, safety and grid compatibility are necessary to electrify the long-range, low-cost and high-utilization transportation sectors. While no technology is suitable for every application, each one discussed in this Review can help to enable at least one of the emerging EV markets (**Figure 2.8**). High-power Pb-acid (Pb-carbon) batteries can supplant a low-power, high-specific energy battery within a low-cost EV, while Ni-MH batteries could improve the range of lithium battery-powered EVs by simultaneously acting as structural or energy adsorption components. Li-S batteries could completely replace Li-ion batteries to enhance the long-range and low-cost EV markets, while Zn-air and Li-air batteries could serve as range-extenders to succeed in these sectors as well. Finally, fast-refuelling and grid-compatible hydrogen fuel cells are a natural fit for high-utilization transportation, while the high specific energy and energy density of hydrogen also makes them attractive for long-range consumer EVs. Li-ion batteries possess the best combination of properties for certain electric mobility applications; however, targeted adoption of a diverse mix of battery and fuel cell-powered EVs will increase the chance of a full transition to clean, low-carbon transportation.

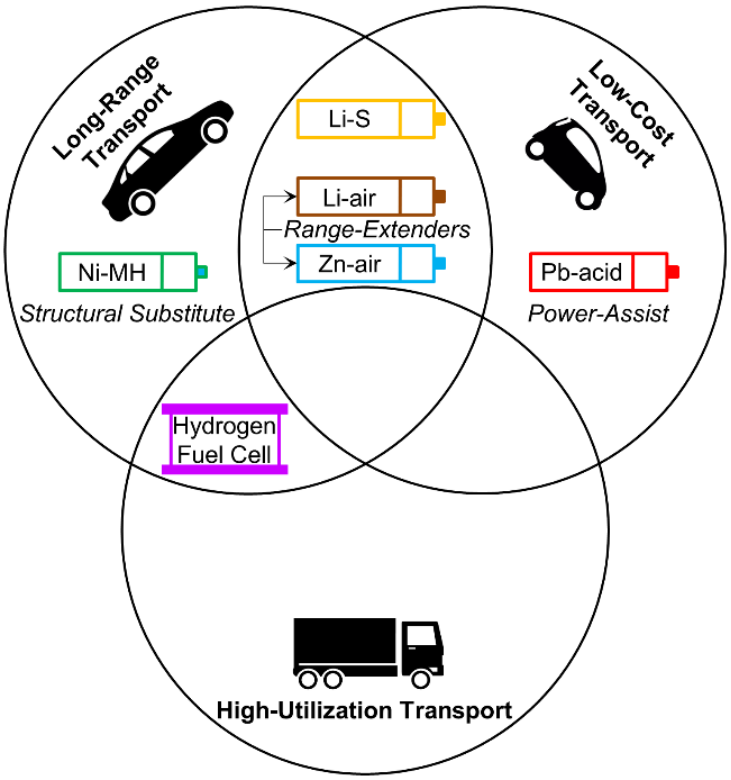

Figure 2.8. Suitability of alternative batteries and fuel cells to emerging EV markets. Pb-acid (Pb-carbon) batteries can provide supplementary power for low-cost EVs due to their low cost and high specific power, but they must be paired with a complementary high-energy battery due to their low specific energy and energy density. Ni-MH batteries, although having a higher cost and lower specific energy and energy density than lithium-based batteries, may be implemented in place of structural or energy adsorption components in long-range EVs due to their safer internal chemistry. Li-S batteries can offer higher specific energy and lower cost than Li-ion batteries, and are therefore attractive to both the long-range and low-cost transportation markets. Li-air and Zn-air batteries have similarly attractive characteristics for both of these markets, but their relatively low cycle life, calendar life and specific power make them better suited as range-extenders to be paired with a more durable and higher-power battery. Hydrogen fuel cells are a fundamentally different technology with decoupled energy and power characteristics, which can make them more cost-effective than pure battery-powered vehicles in long-range applications. Additionally, the flexibility of hydrogen production powered by intermittent renewable energy, low cost of hydrogen storage and quick fuelling of hydrogen into FCEVs make them attractive to high-utilization transportation markets.

Chapter 3: Challenges and Strategies for Designing Energy-Dense Rechargeable Zinc-air Battery Electrodes

3.1 Introduction

In **Chapter 1** and **Chapter 2**, the many advantages of zinc-air batteries (low projected cost, high specific energy and energy density, and inherently safe operation) were discussed particularly regarding their potential application as EV range-extenders. The success of this application mainly depends on making rechargeable Zn-air batteries more durable. Improving the cycling stability of bifunctional oxygen catalysts and zinc electrodes, while maintaining high specific energy and energy density, will be necessary to achieve greater cycle life.[127,128] Reducing or eliminating carbon in the air electrode[129] can also improve the calendar life of Zn-air batteries, since carbon-based air electrodes are subjected to corrosion by the alkaline electrolyte,[130] even when the battery is at rest. However, the only commercial rechargeable zinc-air battery systems to have overcome many of these issues require a circulating electrolyte, electrolyte filtering or three or four-electrode designs to maintain long-term performance,[131–135] which increases complexity and limits the system-level energy density. Zinc-air batteries with a compact cell design and static electrolyte, on the other hand, could meet the energy storage needs for electric vehicles. This chapter therefore provides a review of specific challenges and strategies in designing electrodes for such energy-dense rechargeable zinc-air batteries.

3.2 Zinc-Air Battery Operation and Configuration

The major components and operating mechanism of a Zn-air battery are displayed in **Figure 3.1**. A negative Zn electrode is coupled to a positive air electrode through an external circuit, while an electrochemical pathway between the two electrodes is provided by an ionically conductive electrolyte (typically an aqueous alkaline solution). When the battery is discharged, the Zn electrode is oxidized according to the forward reactions in **Equations 3.1-3.3**, providing a flow of electrons to the external circuit in the process. After travelling across the load in the external circuit, the electrons are consumed at the air electrode by the O_2 reduction reaction (ORR, forward reaction of **Equation 3.4**), with O_2 supplied by the outside ambient atmosphere. Charge balance within the electrolyte is maintained by the diffusion of hydroxide (OH^-) ions produced at the air electrode (**Equation 3.4**) and consumed at the Zn electrode (**Equation 3.3**). The overall chemical reaction, as provided in **Equation 3.5**, results in a nominal cell voltage of 1.66 V. When a rechargeable Zn-air battery is charged by an external power source, the flow of electrons is reversed and the reactions as written in **Equations 3.1-3.5** occur in the reverse direction, releasing O_2 back into the outside atmosphere. An ionically permeable separator is placed between the two electrodes in order to prevent direct physical contact between them.

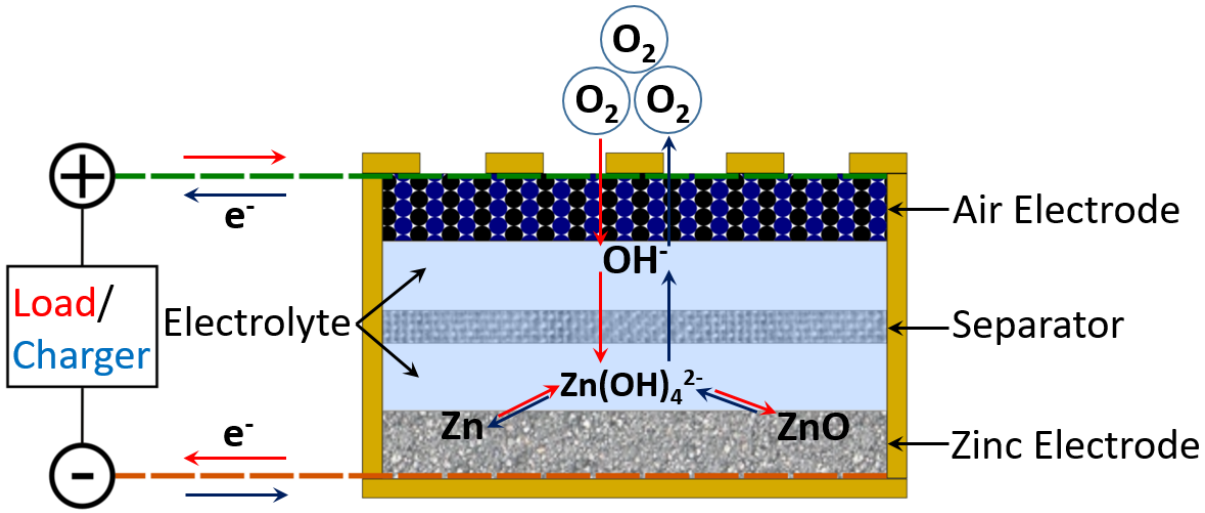

Figure 3.1. Schematic operating mechanism of a rechargeable Zn-air battery. Red arrows and blue arrows represent the direction of movement during discharging and charging, respectively.

Zn electrode reactions:

$$Zn + 4OH^- \Leftrightarrow Zn(OH)_4^{2-} + 2e^- \quad \textbf{(Equation 3.1)}$$

$$Zn(OH)_4^{2-} \Leftrightarrow ZnO + 2OH^- + H_2O \quad \textbf{(Equation 3.2)}$$

Overall:

$$Zn + 2OH^- \Leftrightarrow ZnO + H_2O + 2e^-,\ E° = -1.26\ V\ \text{vs. SHE} \quad \textbf{(Equation 3.3)}$$

Air electrode reaction:

$$O_2 + 2H_2O + 4e^- \Leftrightarrow 4OH^-,\ E° = 0.40\ V\ \text{vs. SHE} \quad \textbf{(Equation 3.4)}$$

Overall cell reaction:

$$2Zn + O_2 \Leftrightarrow 2ZnO,\ E°_{cell} = 1.66\ V \quad \textbf{(Equation 3.5)}$$

Most Zn-air batteries are designed with a planar arrangement; this configuration is presumably favoured over a spiral-wound design, which would lower the amount of direct contact with outside air needed to provide oxygen to the air electrode, although the latter design has received some consideration.[136] In small primary button cells employed for hearing aids, the Zn electrode compartment is composed of atomized Zn powder intermixed with a gelled KOH electrolyte. This compartment is separated from the air electrode by an electrically isolating and ionically conducting separator layer. In order to maximize the energy density, the button cell's casing and cap also act as the current collectors.[137] Larger and multi-cell primary Zn-air batteries (historically used for railroad signaling, underwater navigation and electric fencing) employ a prismatic configuration,[95] as shown in **Figure 3.2**. Besides the shape, this configuration differs from the button cell by including conductive current collectors within a plastic casing, in addition to external tabs from the positive and negative electrodes. The prismatic design is also the most common configuration used in electrically rechargeable Zn-air battery research, where many research groups use a combination of plastic plates and gaskets fastened together with bolts and nuts to assemble the cell.[138–141]

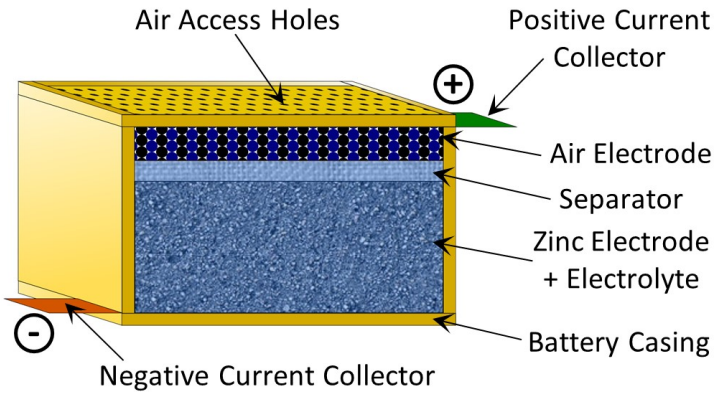

Figure 3.2. Schematic representation of prismatic Zn-air battery configuration.

Several Zn-air cells can be stacked in series in order to raise the battery voltage to a required level for its application. The cells can be stacked using two possible arrangements, referred to as monopolar and bipolar.[142] In the monopolar arrangement (**Figure 3.3**a), the Zn electrode is sandwiched in between two externally connected air electrodes and this basic unit is repeated over multiple cells. To connect the cells in series, external connections are made between the Zn electrode of one cell to the air electrode of the adjacent cell. In the bipolar arrangement (**Figure 3.3**b), each Zn electrode is paired with a single air electrode on only one of its sides. A series connection is made between the air electrode and the Zn electrode of an adjacent cell through an electrically conductive bipolar plate with air flow channels rather than through an external connection.

A large advantage of the bipolar arrangement is that cells can be packaged more efficiently due to the absence of external wiring. In addition, current distribution is more evenly distributed across the electrodes of a bipolar arrangement versus a monopolar arrangement, since the latter

uses external connections to collect current from the electrode edges. However, it is known that edge current collection can generally be employed without significant current distribution effects in alkaline fuel cells (AFCs) with electrode areas less than 400 cm^2.[143] Therefore, this advantage for the bipolar arrangement is likely to be minimal in Zn-air batteries, which typically operate at lower current densities than fuel cells. A disadvantage of the bipolar arrangement is that the air electrode must be electrically conductive across its entire thickness. This means that the air-facing side of the air electrode cannot be composed of a pure polytetrafluoroethylene (PTFE) layer, which is often preferred in order to maximize hydrophobicity and minimize flooding or leakage of the liquid electrolyte from the cell. The bipolar arrangement also requires that a certain pressure be maintained in order to provide sufficient interfacial contact between the electrodes and bipolar plates.[143]

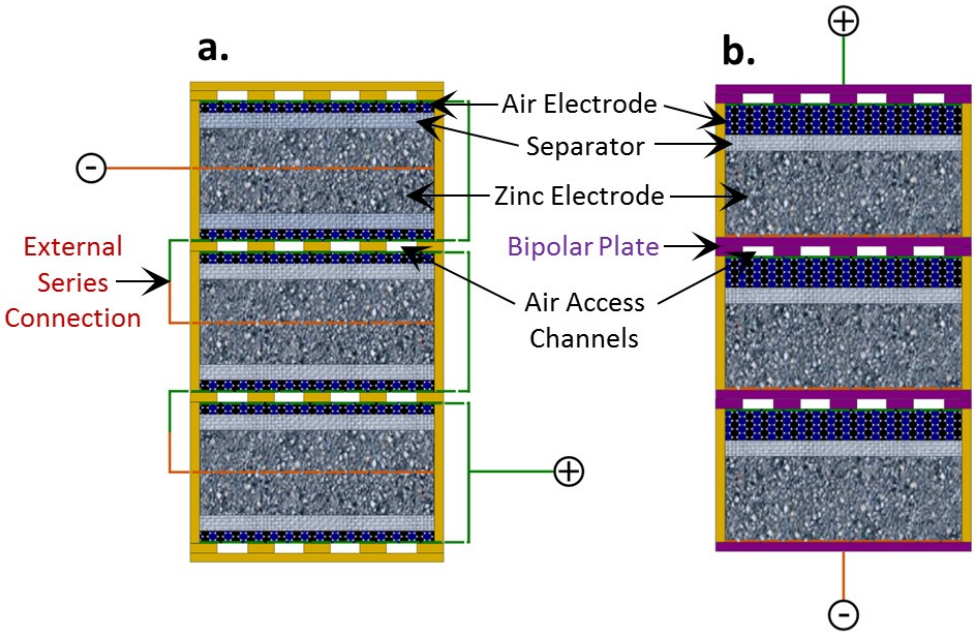

Figure 3.3. Multi-cell Zn-air battery configuration with (a) molopolar arrangement and (b) bipolar arrangement. Air access channels are depicted as going into the page.

3.3 Reversible Zinc Electrode

Given that the Zn-air battery is supplied with an unlimited source of O_2, the Zn electrode is solely responsible for the battery's capacity. A successful Zn electrode should have a high proportion of utilizable active material, be capable of high efficiency recharging and sustain its capacity over long time periods and several hundred charge and discharge cycles. The following two sub-sections detail the scientific phenomena that constrain the achievement of these goals and the strategies that battery developers have used to battle and overcome these constraints.

3.3.1 Performance-Limiting Phenomena

The performance of the Zn electrode is limited by four major phenomena that occur during operation in a Zn-air battery: (i) dendrite growth (**Figure 3.4**a), (ii) shape change (**Figure 3.4**b), (iii) passivation and internal resistance (**Figure 3.4**c) and (iv) hydrogen evolution (**Figure 3.4**d).

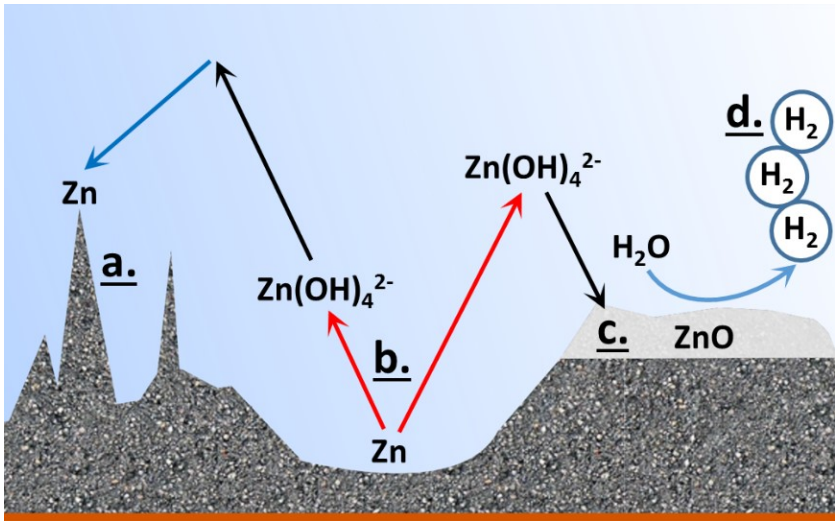

Figure 3.4. Schematic representation of performance-limiting phenomena that may occur on the Zn electrode: (a) dendrite growth, (b) shape change, (c) passivation, (d) hydrogen evolution. Red and blue arrows represent anodic and cathodic processes, respectively.

Zn dendrites, which are defined as sharp, needle-like metallic protrusions, are well-known to form under certain conditions during electrodeposition.[144–147] In secondary alkaline Zn-based batteries, Zn dendrites may form during the charging process and can fracture and disconnect from the electrode (resulting in capacity losses), or more critically, can puncture the separator and make contact with the positive electrode (resulting in a short circuit). Dendritic morphologies arise as a result of concentration-controlled Zn electrodeposition, whereby a positively-sloped concentration gradient of $Zn(OH)_4^{2-}$ ions is established as a function of distance from the Zn electrode surface. Under this condition, $Zn(OH)_4^{2-}$ ions are deposited preferentially at raised surface heterogeneities such as screw dislocations which are higher up the concentration gradient.[144] Upon continued deposition, these deposits grow past the boundary of diffusion-limited region, giving rise to dendrites rapidly growing under nearly pure activation control.[148] Therefore, dendritic growth is more likely to occur at higher deposition overpotentials where diffusion-limited conditions are more prevalent.

Shape change is observed in Zn-air and other alkaline-Zn batteries when Zn is dissolved in the electrolyte during the discharge reaction and then deposits at a different location on the Zn electrode during charging. Over many charge-discharge cycles, this leads to densification of the electrode and a loss of usable capacity.[149–151] In general, modelling and mechanistic investigations have attributed shape change to uneven current distribution within the Zn electrode, uneven reaction zones and convective flows caused by electro-osmotic forces across the battery.[138,149,150,152–157] Many investigators use a KOH electrolyte that is pre-saturated with $Zn(OH)_4^{2-}$ ions (usually by dissolving ZnO powder).[158–165] This is intended to minimize shape

change by inducing the formation of a solid ZnO discharge product at the Zn electrode at an earlier point during discharge. However, the precipitation of ZnO from anodically-discharged $Zn(OH)_4^{2-}$ can occur slowly even in $Zn(OH)_4^{2-}$-saturated KOH solutions.[166,167]

Passivation is the term used to describe an electrode that cannot be further discharged due to the formation of an insulating film on its surface that blocks migration of the discharge product and/or OH^- ions. When a Zn electrode is discharged and the $Zn(OH)_4^{2-}$ discharge product has reached its solubility limit, ZnO is precipitated on the electrode surface. In the case of a porous Zn electrode, passivation is precluded by the reduction of the pore size due to precipitation of ZnO (which takes up more volume than Zn) and finally occurs when freshly discharged $Zn(OH)_4^{2-}$ is far above the solubility limit, causing it to immediately precipitate and fully plug the remaining pore volume.[155,168] This helps to explain why rechargeable Zn electrodes typically require a porosity of 60-75% (in the metallic or charged form),[150,159,169,170] while the theoretical porosity required to physically accommodate the volume expansion from Zn to ZnO is only 37%. The non-conductive property of ZnO also increases the internal resistance of the Zn electrode, which naturally leads to voltage losses during discharging and voltage increases during charging. Zn utilization, defined as the percentage of the theoretical capacity of the Zn mass that is actually used when the electrode is fully discharged, is limited by the point at which the Zn electrode becomes completely passivated or its internal resistance becomes too high to maintain a sufficient operating voltage. The Zn utilization for conventional powder-based electrodes can range from 60-80%,[169–171] while novel developments that will be discussed below can push this value up to 90% or above.

The hydrogen evolution reaction (**Equation 3.6)** has a Standard Reduction Potential (-0.83 V vs. SHE at pH 14) above that of Zn/ZnO (-1.26 V vs. SHE at pH 14). Therefore, hydrogen evolution is thermodynamically favored and a Zn electrode at rest will be corroded over time (**Equation 3.7,** referred to as self-discharge in a battery context, or simply corrosion). This also means that a Zn electrode cannot be charged with 100% coulombic efficiency, since the hydrogen evolution reaction will consume some of the electrons provided to the Zn electrode during charging. The actual rate of hydrogen evolution is defined by its exchange current density and Tafel slope on a Zn electrode surface, which has been measured at 8.5×10^{-7} mA cm^{-2} and 0.124 V $decade^{-1}$, respectively in 6 M KOH.[172] Therefore, at the Zn/ZnO standard reduction potential, the hydrogen evolution current on a Zn surface is on the order of 1×10^{-5} mA cm^{-2}.[172] However, the hydrogen evolution overpotential is significantly reduced on a ZnO surface,[173] which means that the self-discharge rate will increase as ZnO forms on the discharging Zn electrode.

$$H_2O + 2e^- \Leftrightarrow 2OH^- + H_2 \qquad \textbf{(Equation 3.6)}$$

$$Zn + 2H_2O \rightarrow ZnO + H_2 \qquad \textbf{(Equation 3.7)}$$

3.3.2 Strategies for Improving Performance

A number of modifications to the Zn electrode have been investigated to increase its performance, in terms of cycle life (measured by capacity retention as a function of cycle number), capacity (determined by Zn utilization, among other factors) and coulombic efficiency (determined by extent of hydrogen evolution). These strategies have been organized into six methods and are summarized in **Table 3.1**. More detailed information on each strategy can be found in the listed references within the table, as well as the review paper[174] this chapter was adapted from. To

summarize, structural modification through electrodeposition and advanced casting techniques, as well as compositional modification by means of additives and/or chemical doping have been demonstrated to be feasible solutions. The most promising additives are those which are effective in small quantities, since a larger proportion of additives reduces the overall Zn capacity. **Table 3.2** contains performance metrics, including capacity densities, Zn utilization and the number of cycles with over 80% retained capacity, of some Zn electrodes that have employed these strategies. The areal capacities are also calculated, which highlights the difficultly in achieving both a high cycle life and high areal capacity

Table 3.1. Strategies for improving Zn electrode performance.

Strategy	Direct influence on			
	Dendritic Growth	**Shape Change**	**Passivation and Internal Resistance**	**Hydrogen Evolution**
(1) High Surface Area/ 3-D Electrode Structure[15,160,175–177]	**Minimized** (Decreases charging overpotential)	**Minimized** (3-D Structure improves current distribution)	**Minimized** (High surface area minimizes ZnO film thicknesses)	**Increased** (Higher surface area causes more intense hydrogen evolution)
(2) Polymeric Binders[149,178,179]	-	**Minimized** (Improves mechanical strength)	**Increased** (Increases electrode resistance)	-
(3) Carbon-Based Electrode Additives[180–185]	-	**Minimized** (Improves current distribution)	**Minimized** (Improves electrode conductivity)	-
(4) Heavy Metal Electrode Additives[180,186–190]	**Minimized** ("Substrate effect" promotes denser deposits)	**Minimized** (Improves current distribution)	**Minimized** (Improves electrode conductivity)	**Minimized** (Increases hydrogen overpotential)
(5) Discharge-Trapping Electrode Additives [150,158,161,165,171,191–195]	**Minimized** ($Zn(OH)_4^{2-}$ concentration gradient is reduced)	**Minimized** (Discharge product migration is reduced)	Possibly minimized (If trapped discharge product conductivity higher than ZnO)	-
(6) Electrode Coatings[162,196–201]	**Minimized** ($Zn(OH)_4^{2-}$ concentration gradient is reduced)	**Minimized** (Discharge product migration is reduced)	-	-

Table 3.2. Performance metrics of selected Zn electrodes disclosed in the literature.

Reference	Strategies ( )	Electrode, Electrolyte Composition	Electrode Thickness [mm]	Specific Capacity [Ah kg^{-1}][a)]	Volumetric Capacity Density [Ah L^{-1}][b)]	Zn Utilization [%]	Cycling Conditions[c)]	# Cycles with >80% Retained Capacity[d)]	Areal mass (g cm^{-2})	Areal Capacity (mAh cm^{-2})
Theoretical	-	100% Zn	-	820	5846	100	-	-	-	-
	-	100% ZnO	-	658	3694	100	-	-	-	-
Yan 2015[176]	1,6	Zn-electroplated Cu Foam, 8 M KOH + 0.5 M ZnO	2	754	39	92	100 mA cm^{-2} 100% DOD	9000+	0.010	7.9
Chamoun 2015[177]	1	3D Hyper-dendritic Zn sponge electrodeposited onto Ni mesh, 8.9 M KOH	[e)]	719	1282-2051	88	C/5 Rate 40% DOD	100+	-	-
Parker 2014[175]	1,2,4	3D Zn sponge + 300ppm In + 300ppm Bi, 6 M KOH	1-4	728	928	89	5 mA cm^{-2} (discharge) 3 mA cm^{-2} (charge) 20% DOD	~25	0.13-0.51	92.8-371.2
Wang 2014[195]	1,2,3,5,6	Calcium zincate powder + 5 wt.% Zn + 10 wt.% acetylene black + 5 wt.% PTFE, 6M KOH + Sat'd ZnO	0.2	385	338-540	98	2C Rate 100% DOD	250+	0.018-0.028	6.8-10.8
Huang 2015[165]	1,2,3,5,6	Zn-Al-layered double oxide powder + 10 wt.% acetylene black + 5 wt.% PTFE, 6 M KOH + Sat'd ZnO	0.2	469	552-883	87	1C Rate 100% DOD	1000+	0.024-0.038	11.0-17.7
Yuan 2011[198]	1,2,4,6,7	Bi-based nanoparticle-coated ZnO powder + 4.8 wt.% PTFE + 0.6 wt.% CMC, 4.5 M KOH + 1.6 M K_2BO_3 + 0.9 M KF + 0.1 M LiOH	0.3	656	1025-1640	90	C/5 Rate 100% DOD	50+	0.047-0.075	30.7-49.2
Zeng 2011[163]	1,2,3,4,6	In-doped ZnO powder + 8.3 wt.% PTFE + 8.3 wt.% graphite, 4.5 M KOH + 1.0 M NaOH + 0.5 M LiOH + Sat'd ZnO	0.28	586	727-1164	92	~C/4 Rate 100% DOD	73+	0.035-0.056	20.4-32.6

[a)]Includes mass of additives and based on mass of charged (non-oxidized) electrode with the exception of 100% Solid ZnO; [b)]If the necessary information to calculate volumetric capacity density was not reported, a range is calculated based on the electrode material densities and a typical charged electrode porosity of 60-75%[48, 55-57]; [c)]Depth of Discharge abbreviated as DOD;

[d]"+" indicates that the electrode provided >80% of its initial capacity when cycling was terminated; [e]Not reported.

3.4 Electrolyte and Separator

Aqueous alkaline electrolytes are most commonly employed in Zn-based battery chemistries for several reasons, which include cost effectiveness, high ionic conductivity and Zn electrode stability.[202–204] Sufficient OH^- concentrations within the electrolyte are also necessary to avoid high overpotentials for the O_2 reactions at the air electrode, and further allow the use of non-precious metal catalysts.[31,205] KOH-based electrolytes are the most common in comparison to NaOH or LiOH electrolytes, due to the former's superior ionic conductivity.[12,206] Unfortunately, issues that arise with using aqueous alkaline electrolytes within a Zn-air battery include evaporation or moisture uptake (depending on relative humidity conditions) and carbon dioxide (CO_2) poisoning from the outside atmosphere. Electrolyte evaporation reduces the ionic pathway between the battery electrodes, while moisture uptake lowers the alkalinity and can cause swelling of the cell.[31,137,207] Diffusion of CO_2 into the electrolyte lowers its alkalinity and eventually leads to the precipitation of solid carbonates (e.g. potassium carbonate (K_2CO_3)) which clog the pores of the air electrode.[31,142,207]

Room temperature ionic liquids (RTILs) have received increased attention in recent years as an alternative to aqueous-based electrolytes for rechargeable Zn-air batteries. RTILs are molten salts with melting temperatures at or below room temperature, and are stable at a wide range of electrochemical potentials.[204] They have the advantage of being largely immune to both CO_2 poisoning and evaporation,[208] and have also been reported to suppress dendrite growth of the Zn

electrode.[209] However, most RTILs that have been considered for Zn-air batteries have ionic conductivities approximately 10-100 times lower than concentrated KOH solutions.[208] In addition, the ORR mechanism in RTILs typically involves several electron transfer steps,[210] unlike ORR in alkaline media which is typically close to the 4-electron mechanism (**Equation 3.4**) with the appropriate catalyst. Both of these factors lead to large cell voltage decreases with increasing currents,[208] which does not make them well suited for high-power applications such as EVs.

Aqueous electrolytes are often "gelled" by mixing in polymers such as polyvinyl alcohol, poly(acrylic acid) and polyethylene oxide.[207,211,212] Gelled, or "quasi-solid state", electrolytes are used extensively in primary Zn-air batteries in order to prevent leakage and slow down evaporation.[95] Successful gelled electrolytes have conductivities on the same order of magnitude as conventional aqueous alkaline electrolytes.[204] However, it is generally difficult to recharge Zn electrodes in gelled electrolytes due to their low solubility for $Zn(OH)_4^{2-}$, which leads to difficulties in transforming ZnO back to the intermediate $Zn(OH)_4^{2-}$ before reduction to Zn metal.[204] Recent work on flexible Zn-air[183] and Ni-Zn[213] batteries has shown that rechargeability is possible using gelled electrolytes; however, the Zn electrode thicknesses and currents demonstrated were likely too low for an EV application.

Therefore, it appears that primarily aqueous alkaline electrolytes may be the best choice for EV applications, despite the above-mentioned problems of CO_2 poisoning and evaporation/moisture uptake. Various battery designs have been proposed to alleviate these problems, such as incorporating an electrolyte dispenser system[214], moisture control system[215]

or a CO_2 air scrubber[216,217] into the battery pack. Additionally, mechanical[16] or load-responsive[218] air electrode seals have been proposed in order to limit ingress of CO_2 and ingress or egress of water when the cell is not in use.

If aqueous alkaline electrolytes are employed in rechargeable Zn-air batteries, the Zn electrode shape change issue (**Section 3.3.1**) will certainly be a concern. It can be observed in **Figure 3.5** that this problem is exasperated by the properties of the maximum conductivity KOH electrolyte (6-7 M or 25-30 wt.% KOH) that is most typically used in alkaline-Zn batteries. Zn redox kinetics (indicated by the Zn/Zn^{2+} exchange current density) are near their maximum at this concentration, and the solubility of the ZnO discharge product increases with increasing concentration. Therefore, during battery operation a large amount of Zn is expected to be dissolving, migrating and re-depositing under non-uniform conditions caused by the reasons described in **Section 3.3.1**.

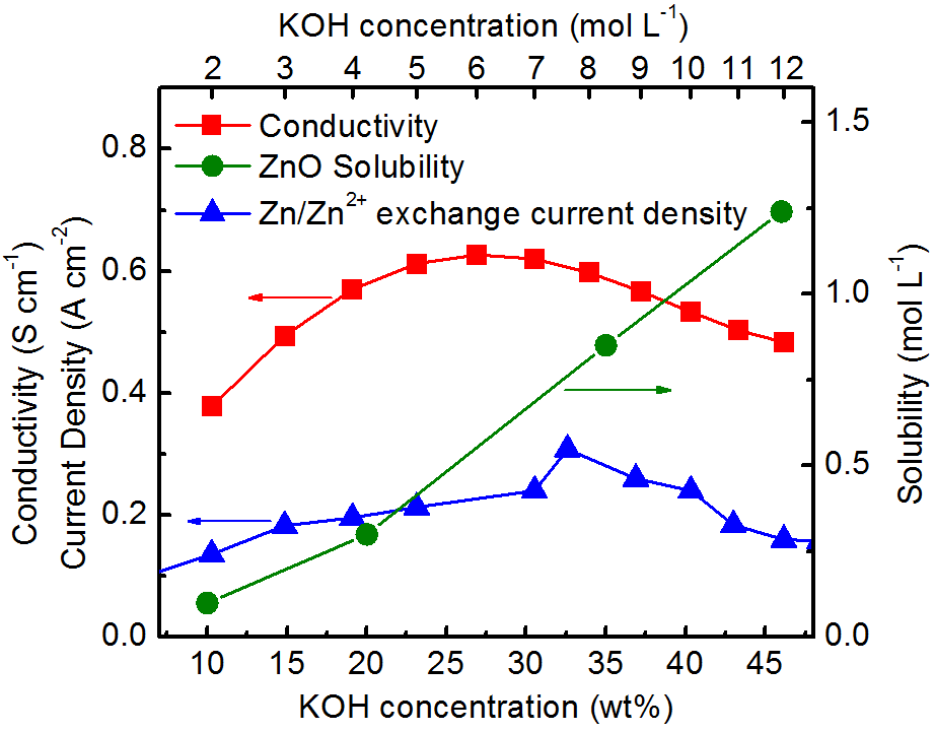

Figure 3.5. Electrolyte conductivity, Zn/Zn^{2+} exchange current density and ZnO solubility as a function of KOH concentration (data from [202,219,220])

As shown in **Figure 3.5**, the solubility of ZnO is reduced at lower KOH concentrations, which will reduce the tendency for Zn electrode shape change.[221,222] Therefore, a clever approach (borrowed from rechargeable Ni-Zn battery research) to improve the Zn electrode lifetime involves lowering the KOH concentration as much as possible without substantially reducing the catalytic performance of the air electrode, and then adding other ionic compounds such as KF, K_2CO_3, K_3BO_3 and K_3PO_4 to restore the electrolyte conductivity.[150] With this strategy, the $Zn(OH)_4^{2-}$ solubility can be reduced to less than half of its original value (in 7 M KOH) while maintaining above 75% of the original electrolyte conductivity.[166] Adler et al.[159,223] found that an electrolyte

composed of 3.2–4.5 M KOH, 2 M KF, 2M K_2CO_3, saturated ZnO and a suspension of 0.5 M LiF resulted in optimal performance and cycle life of a Ni-Zn battery (the Li^+ additive is beneficial to the $NiOOH/Ni(OH)_2$ electrode[150]). However, CO_3^- additives are not appropriate for aqueous electrolytes of Zn-air batteries, since this will lead to quicker saturation and precipitation of K_2CO_3 in the air electrode pores as CO_2 enters from the outside environment. K_3BO_3 and K_3PO_4 additives, which have also shown promise for Ni-Zn batteries,[166,224] thus seem to be a better choice for Zn-air batteries and deserve a thorough investigation.

In order to prevent short-circuits in rechargeable Zn-air cells, several stringent properties are required from the chosen separator. It must be electronically insulating, ionically conductive, chemically resistant to the alkaline electrolyte and also electrochemically stable at the wide range of charging and discharging voltages experienced in the battery. Microporous polypropylene membranes produced by Celgard LLC, such as Celgard 5550, possess these properties and are extensively employed in rechargeable Zn-air battery research.[31,225] However, $Zn(OH)_4^{2-}$ ions can also pass through the micropores of these separators, potentially leading to precipitation of ZnO on the air electrode surface, and subsequent interference of the catalyst sites or blockage of the air electrode pores.[226] Thus, anion exchange membranes (which allow hydroxide ion passage while blocking $Zn(OH)_4^{2-}$ ions) are currently an active area of research for rechargeable Zn-air batteries.[184,227–230]

3.5 Bifunctional Air Electrode

While the Zn electrode is the determining factor of the Zn-air battery's capacity, its power performance and energy efficiency are largely dependent not only on the electrolyte, but also on the air electrode. This stems from the fact that the ORR during discharging and the O_2 evolution reaction (OER, reverse reaction in **Equation 3.4**) during charging both have much larger energy barriers to overcome than the Zn electrode reactions. Energy barriers in a battery result in potential (i.e. voltage) losses, which can be separated into activation polarization, ohmic resistance and concentration (i.e. mass transfer) polarization. The sum of these losses equates to the difference between the battery's operating voltage and open circuit voltage. The example discharge and charge polarization plots in **Figure 3.6** show the importance of minimizing voltage losses in the zinc air battery, since large polarization can cause substantial losses in energy efficiency and also (for discharging) can lower the specific energy or energy density of the zinc-air battery. This highlights the importance for the air electrode to be engineered with suitable catalysts to minimize activation barriers for the ORR and OER in addition to an appropriate structure enabling efficient transport of O_2 and OH^- to and from the catalyst sites.

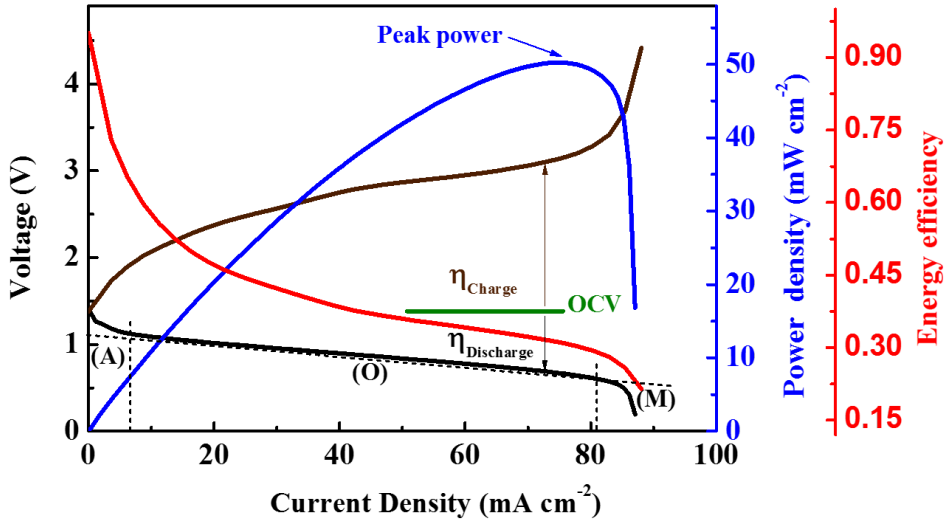

Figure 3.6. Example of discharge (black line) and charge (brown line) voltages, power density (blue line) and energy efficiency (red line) as a function of current density for a rechargeable zinc-air battery. The activation, ohmic and mass transfer-dominated polarizaton regions are identified by A, O and M labels, respectively.

3.4.1 Electrode Design

Designing an appropriate structure for the air electrode is particularly challenging in comparison to other battery electrodes due to the requirement for providing sufficient three-phase interfacial sites. As seen in **Equation 3.4**, the ORR requires the gas phase (O_2), liquid phase (H_2O) and solid phase (electron conductor) to all be in close proximity in order to proceed at certain reaction site. While the OER only strictly requires a two-phase interface (liquid and solid), the air electrode structure must allow efficient removal of O_2 gas; otherwise O_2 bubbles will appear in the electrolyte reduce the size of the solid/liquid interfacial area. Extensive research has been conducted on air electrode design for both polymer electrolyte membrane (PEM) and alkaline fuel cell (AFC) applications. However, similar work has not been carried out on the air electrode design

for rechargeable metal-air batteries; in fact, a large amount of research on catalysts for rechargeable zinc-air batteries has been conducted using commercial carbon-based air electrode supports designed for PEM fuel cells.[141,185,231–234] Given the lack of work on bifunctional air electrode structures and designs, it is important to review the literature on fuel cell air electrodes (particularly AFCs).

As shown in **Figure 3.7**, the air electrode architecture generally consists of three layers.[235] The gas diffusion layer (GDL) facilitates the transfer of the air or oxygen reactant to the catalyst sites within the active layer, while the active layer (AL) contains the oxygen reaction catalysts and interfaces with the electrolyte to provide the three-phase reaction zone. The backing material or backing layer provides structural support to the other layers; it may also act as the current collector and is not necessarily located behind the GDL as indicated in **Figure 3.7**.[236] In fuel cell air electrodes, the GDL and AL have traditionally been composed of mixtures of PTFE and carbon or graphite powders, with the AL additionally containing ORR catalysts. PTFE is chosen for its ability to bind the other powder components together and its highly hydrophobic property which allows for the establishment of gas phase channels within the electrode.[237] PTFE also exhibits relatively good chemical stability in a wide range of environments, including alkaline electrolytes.[237,238] Carbon and graphite powders are typically chosen as the conductive component of the air electrode due to their low cost, activity for the ORR and their widely tunable surface area and porosity.[143,237,239–241] The GDL and AL are most often formed by rolling or pressing a wet slurry of the chosen carbon, PTFE and catalysts onto the backing layer.[235]

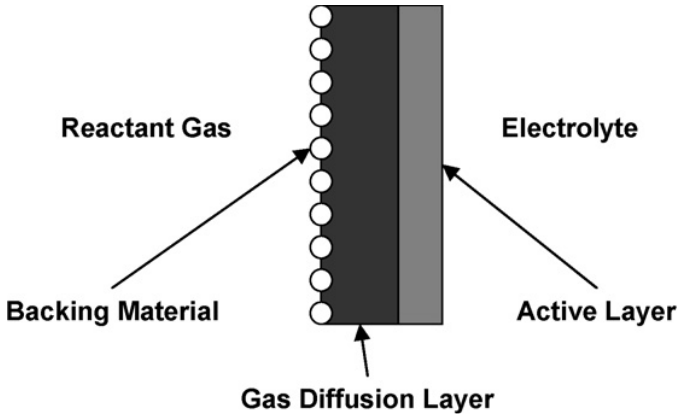

Figure 3.7. General architecture of fuel cell or metal-air battery air electrode.[235]

For AFCs with a monopolar design (**Figure 3.3**a), the GDL is typically composed entirely of PTFE in order to minimize the potential for flooding. Pores in the PTFE layer are produced by mixing PTFE with a low decomposition-temperature additive such as ammonium carbonate, which is burned off during a heat-treatment.[235] A current collector, typically a metal mesh or foam, must be placed in front of the 100% PTFE GDL layer (e.g. between the GDL and AL) in this case. In a bipolar design (**Figure 3.3**b), the GDL must be hydrophobic and conductive; therefore, the GDL is usually fabricated using a mixture of PTFE and a hydrophobic carbon powder such as acetylene black, with a PTFE content ranging from 25-60%.[143,235,237] The AL, which must be conductive and slightly hydrophilic in order to establish three-phase reaction zones, is typically composed of high-surface area carbons and a lower PTFE content ranging from 2-25%.[235]

The establishment of three-phase reaction zones is highly dependent on the pore structure of the AL and is most often explained by the "flooded agglomerate" model described by Giner and Hunter.[242] In this model, carbon particles are tightly packed in to agglomerates with electrolyte

filling the inter-particle voids (**Figure 3.8**a), and the agglomerates are held together by a hydrophobic network of PTFE particles (**Figure 3.8**b).[235,242–244] The reactant gas arriving from the GDL diffuses through these hydrophobic channels, dissolves into the electrolyte film surrounding the agglomerates and further diffuses to the catalyst sites within flooded agglomerate pores. The three-phase reaction zone in the AL layer can be enhanced by selecting hydrophobic carbon particles with extensive interconnected micropores (**Figure 3.8**a), which are not flooded by the electrolyte and thus provide better dispersion of gas channels to the catalyst sites.[237]

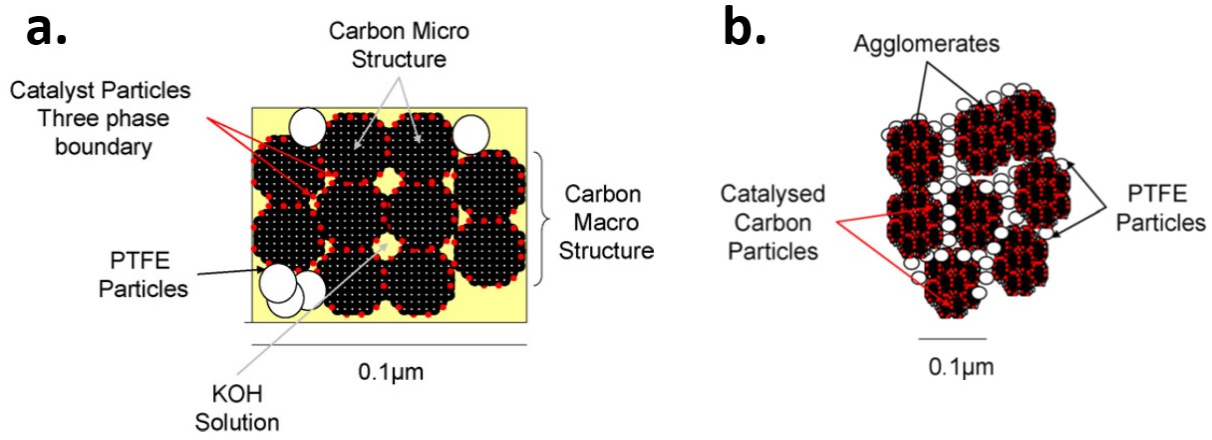

Figure 3.8. Schematic representations of pore structures within AL composed of catalyst-coated carbon powders and PTFE particles; (a) single flooded agglomerate, (b) group of agglomerates held together by a network of PTFE particles.[235]

Unfortunately, carbon-based GDLs and ALs are not considered to be appropriate for use in the air electrodes for rechargeable zinc-air batteries. This is due to the fact that carbon is susceptible to corrosion at the high oxidizing potentials experienced at the air electrode during charging, and further does not have to ability to form a passivating layer.[130,245] When subjected

to high anodic potentials in an alkaline electrolyte, carbon produces carbon monoxide gas in addition to carbonate (CO_3^{2-}) ions;[130] the latter of these can combine with CO_2 poisoning from the outside atmosphere to hasten the precipitation of K_2CO_3 in the air electrode pores. The standard potential of carbon oxidation in alkaline electrolyte (pH of 14) is -0.78 V vs. SHE (0.48 V vs. Zn/ZnO), which is much lower than the ORR/OER equilibrium potential (0.40 V vs. SHE, 1.66 V vs. Zn/ZnO).[246,247] Therefore, although graphitization of carbon improves its corrosion resistance,[248–253] corrosion is thermodynamically favored even at the open circuit voltage of zinc-air batteries. Graphitization of carbon powders improves their corrosion resistance,[248,249], and bifunctional air electrodes with hundreds of charge-discharge cycles have been demonstrated using graphitized carbon-based air electrodes (albeit at modest currents).[250,251,253]. However, the formation of CO_3^{2-} ions is likely inevitable even when they are graphitized; this is an increasingly severe problem in commercially-relevant cell designs (e.g. **Figure 3.2**), since the CO_3^{2-} saturation point would be quickly reached with a minimum volume of electrolyte. Therefore, it appears that metal-based air electrodes that are largely free of carbon components are more suitable for rechargeable zinc-air batteries.

However, relatively few investigations have focussed on metal-based air electrodes for rechargeable metal-air batteries. Silver (Ag)-based air electrodes with increased stability relative to carbon-based air electrodes have been demonstrated for AFCs and Li-air batteries;[236,254,255] however, the high cost of Ag makes it impractical for inexpensive Zn-air batteries. A promising air electrode based on less expensive nickel (Ni) metal was recently demonstrated by Price and coworkers[129,256] for flow-based rechargeable zinc-air batteries. Their fabrication technique

involved the pressing of a slurry composed of Ni powder and PTFE onto a Ni foam substrate followed by dip-coating in a catalyst precursor solution. The resulting bifunctional air electrode demonstrated stable potentials after 50 charge-discharge cycles at a relatively high current density (50 mA cm^{-2}), which is near the maximum required for a zinc-air battery EV range extender that was recently modeled.[257] An 1981 report by Armstrong[258] for Canada's Department of National Defence also documented a nickel-based air electrode produced by dip-coating a 0.71 mm-thick, 84.7% porous sintered nickel plaque in a catalyst precursor solution, which displayed over 200 charge-discharge cycles at a relatively high current density (50 mA cm^{-2})

3.4.2 Oxygen Reaction Catalysts

The development of bifunctional catalysts that can efficiently facilitate the oxygen reduction reaction (ORR) and the oxygen evolution reaction (OER) with low overpotentials, while also remaining stable over hundreds of charge-discharge cycles in alkaline electrolytes, is currently the most intense area of research involving rechargeable zinc-air batteries.[31,128,259,260] Traditionally, noble metals such at platinum (Pt) have been employed for their high ORR activities while noble metal oxides such as ruthenium(IV) oxide (RuO_2) and iridium(IV) oxide (IrO_2) are known for their high OER activities. However, these catalysts are prohibitively expensive for low-cost zinc-air batteries, and further, metal catalysts including Pt are unstable towards oxidation at the high potentials that the OER operates at.[260,261] Therefore, most research is currently focussed on bifunctional non-noble metal oxides; these are usually oxides with mixed valence states such as spinels and perovskites.[31,128,260] Nanostructured carbon materials have also been heavily studied, often in combination with metal oxides, due to their enhanced conductivity relative to metal

oxides.[31,128,260] However, as mentioned in Section 2.4.1, carbon materials are generally detrimental to the lifetime of rechargeable zinc-air batteries due to their instability propensity to form poisoning CO_3^{2-} ions.[262] Therefore, carbon-free catalysts are exclusively focused on in the brief discussion below.

Manganese oxides (MnO_x), are well known for their strong ORR activity in addition to being inexpensive, and are thus the primary choice for primary zinc-air batteries (particularly as MnO_2).[95,137,202] This is due to the ability of Mn to possess and transform between multiple valences, allowing it to assist electron transfer by switching between an oxygen acceptor and donor.[259] However, when acting as a bifunctional catalyst, MnO_x have been found to switch between different crystal structures during cycling between ORR and OER operation.[263] This suggests that this catalyst may not display sufficient long-term stability in a rechargeable zinc-air battery.

Mixed-metal perovskite oxides, with the general chemical formula ABO_3, have traditionally been a popular choice as a bifunctional catalyst for rechargeable zinc-air batteries.[250,262,264,265] In the normal perovskite structure, the A sites are relatively large rare earth or alkali metal cations while the B sites are relatively small transition metal cations.[262] By substituting the either or both of the A and B sites with cations with other valence states, oxygen vacancies can be created and the compound's electronic structure can be widely tuned. Suntivich et al. have developed design principles for optimizing the ORR[266] and OER[267] catalytic activity of perovskites based on altering specific electron orbitals. Appropriately designed perovskites have excellent ORR and

OER activities and stability; however, they have a disadvantage of relatively difficult preparation and generally require heat treatment at 600°C or above.[250,264,266,268,269]

Spinel oxides, with the general chemical formula AB_2O_4, are another common choice as bifunctional catalysts.[129,256,270–275] The A and B sites are both transition metal cations with +2 and +3 valences, respectively, and can either be represented by the one element (e.g. Co_3O_4) or multiple elements (e.g. $NiCo_2O_4$). Co_3O_4 is the most heavily studied spinel oxide bifunctional catalyst, which is known to facilitate good activity for ORR on the Co^{2+} sites and OER activity on the Co^{3+} sites.[275] While a vast number of binary element-spinel oxides have been investigated, $NiCo_2O_4$ has emerged as a widespread bifunctional catalyst due the improved 4-electron reaction ORR pathway and lower OER overpotential imposed by the Ni^{2+} lattice sites.[271,273] Spinel oxides can be synthesized relatively easily and at moderate temperatures between 300-480°C.[271] They are already used in many industrial applications,[271] and are thus a logical choice for use rechargeable zinc-air batteries. Both Price and coworkers[129,256,273] and Armstrong[258] chose $NiCo_2O_4$ as the most suitable catalyst for their Ni-based air electrodes due to the ease of synthesis using the dip-coating/co-precipitation method.

Chapter 4: Performance and Failure Mechanism of Nickel-Based Air Electrodes for Rechargeable Zinc-Air Batteries

4.1 Introduction

Due to the kinetically slow oxygen reduction reaction (ORR) and oxygen evolution reaction (OER), the power and energy efficiency of a rechargeable zinc-air battery is highly dependent on the catalytic performance of the air electrode.[12] Most research has focused on surface and structure engineering of bifunctional catalysts to optimize their oxygen binding energies and cohesive strength for efficient and stable ORR and OER.[275–278] However, relatively little attention has been paid to the support and/or current-collector materials of the air electrode, and as detailed in **Section 3.4.1**, carbon-based gas diffusion electrodes as well as carbon and graphite powders are often used as the conductive catalyst support even though they are susceptible to carbon corrosion. Therefore, rechargeable zinc-air batteries with high energy density, long cycle life and long calendar life require more corrosion-resistant materials in the air electrode.

Metal-based air electrodes can offer much higher corrosion resistance due to their ability to form a passivating film on their surface, which greatly reduces the metal oxidation rate. Due to their relatively high stability and low cost, nickel-based air electrodes have been adopted by some research groups for demonstration of novel bifunctional catalysts.[274,279,280] The dip-coated nickel-based electrodes mentioned at the end of **Section 3.4.1** have also shown promising performance. An interesting electrochemical phenomenon in these electrodes is that the oxidized nickel metal in

the (oxy)hydroxide passivating layer alternates between the 2+ and 3+ states ($Ni(OH)_2$ and NiOOH) during the start of discharging and charging, respectively, which was reported as beneficial to its efficiency due to the lower overpotential of these reactions relative to the ORR and OER.[256]

However, the degradation mechanism of nickel-based air electrodes after extended cycling has not been discussed in the literature. This is an important consideration, since voltage losses after battery cycling might be mistakenly attributed to degradation of the catalyst particles instead of possible material changes on the supporting nickel electrode. The electrode structure is presumed to resemble the "flooded agglomerate" model of typical carbon-based air electrodes (**Figure 3.8**), with electrolyte-flooded agglomerates of catalyst-coated nickel particles bound by a network of hydrophobic channels established by the PTFE binder. However, a key dynamic which does not apply to carbon-based air electrodes is the influence of the (oxy)hydroxide passivating layer on this mechanism. Whether this dynamic contributes to voltage losses of zinc-air batteries with nickel-based air electrodes, and if so to what extent, needs to be understood for extending battery durability.

To address this question in this work, nickel-based air electrodes were fabricated and investigated with a series of cyclic galvanostatic and potentiodynamic polarization experiments. The structure of the electrode before and after cycling was characterized to confirm the presence of a passivating nickel (oxy)hydroxide film. A multi-step discharge method was used to estimate the growth of the nickel (oxy)hydroxide passivating film, which was linked to dynamic potential losses at the air electrode. Relative contributions of ohmic, activation and mass transfer potential

losses were evaluated at a current density of 10 mA cm^{-2}, which is commonly used for evaluation of static-electrolyte rechargeable zinc-air batteries. The results provide strong evidence of a degradation mechanism for nickel-based air electrodes which is distinct from degradation of the catalyst itself. This insight will aid in the design of more robust bifunctional metal-based air electrodes for long-lasting rechargeable zinc-air batteries.

4.2 Experimental Methods

4.2.1 Electrode Preparation and Characterization

The preparation procedure for the nickel-based gas diffusion electrode was adapted from Price et al.[129] Nickel foam (110 pores per inch, 42 mg cm^{-2}, 1.7 mm thick) was used as the electrode support and current collector. Prior to electrode rolling, the nickel foam was ultrasonically treated in acetone for 20 min, etched in 1 mol L^{-1} HCl at 80°C for 1 h, rinsed and ultrasonically treated in deionized water for 15 min, rinsed with isopropyl alcohol (IPA) and finally dried in air. To prepare the electrode slurry, nickel powder (Sigma Aldrich, Product #266981) with an average particle size of approximately 3 μm was added to a vial together with a 50/50 mixture of IPA and deionized water. 60 wt.% PTFE emulsion (Sigma Aldrich, Product #665800) was then added dropwise to the vial while stirring and the slurry was ultrasonically mixed for 30 min. The slurry was blended in a planetary mixer for 5 min to bind the nickel powder with the PTFE. After pouring out excess liquid, the blended mass was placed onto aluminum foil and rolled into a flat sheet with the same area as the nickel foam. The nickel/PTFE sheet was then pressed into the nickel foam and rolled to a combined thickness of 1000 μm using fixed-width rollers. The dried

nickel/PTFE slurry had a PTFE content of 30%, and the slurry mass loading in the nickel foam was approximately 180 mg cm^{-2}. After allowing the rolled electrode to dry overnight, the electrode was heated at 350°C in air for 30 min and then immersed in a cobalt/nickel nitrate precursor solution for 5 min. The precursor solution consisted of 2 mol L^{-1} cobalt (II) nitrate (Sigma Aldrich, Product #239267) and 1 mol L^{-1} nickel (II) nitrate (Sigma Aldrich, Product #72253) dissolved in a 60/40 mixture of H_2O/IPA. The electrode was dried in air at room temperature for approximately 3 h and finally was heated at 350°C in air for 3 h to convert the nitrates into the nickel cobalt oxide ($NiCo_2O_4$) spinel phase.

The final gas diffusion electrode (depicted in **Figure 4.1**a) had a diameter of 1.9 cm and included an approximately 2 cm long extended piece of the nickel foam current collector which acted as the working electrode connection. A thin-layer electrode was also fabricated by rolling an identical nickel/PTFE mixture down to 150 μm (dry slurry mass of approximately 75 mg cm^{-2}), pressing it onto a nickel foil current collector and carrying out the same heating and dip-coat treatment as described above. Morphological characterization of the gas diffusion electrode was conducted with a Zeiss LEO 1530 field emission scanning electron microscope (SEM). X-ray diffraction (XRD) was conducted on a MiniFlex 600 Rigaku instrument, and X-ray photoelectron spectroscopy (XPS) was conducted on a Thermal Scientific K-Alpha XPS spectrometer.

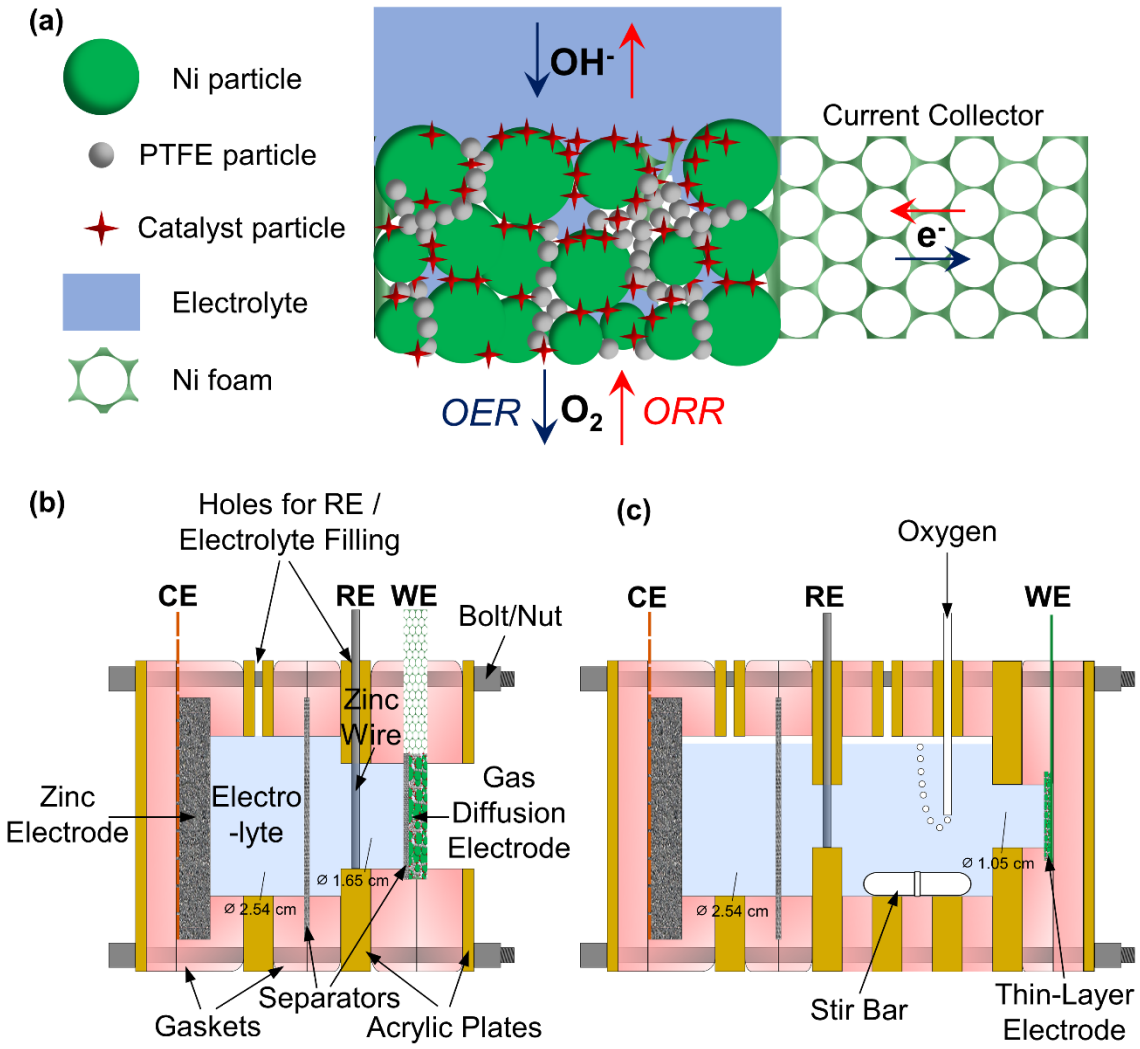

Figure 4.1. (a) Schematic depiction of single-layer nickel-based gas diffusion electrode (particles enlarged relative to the nickel foam pores for clarity), and schematic representations (side-view) of three-electrode cells for performance evaluation of (b) nickel-based gas diffusion electrode and (c) nickel-based thin-layer electrode as the working electrode (WE). A porous zinc electrode and zinc wire were employed as the counter electrode (CE) and reference electrode (RE), respectively.

4.2.2 Cell Design

Two cell designs (**Figure 4.1**b,c) containing a combination of acrylic plates and silicone gaskets fastened together with bolts and nuts were employed for electrochemical testing. Each design utilized a three-electrode configuration including a porous zinc counter electrode and zinc wire reference electrode. Unlike a two-electrode configuration, the cells employed here ensured that any possible degradation of the porous zinc electrode during cycling would not affect the potential measurement at the air electrode. The electrolyte in each experiment was an aqueous solution of 6 mol L^{-1} KOH prepared from distilled and deionized water. The electrolyte was also pre-saturated with zinc oxide (ZnO) to improve cyclability of the zinc electrode and to ensure that the potential of the zinc wire reference electrode maintained a stable equilibrium potential. Porous zinc electrodes were prepared via cathodic electrodeposition from a fresh electrolyte with the same composition as above onto a Cu mesh current collector at a potential of -300 mV vs. Zn/ZnO.[177] The capacities of these zinc electrodes were at least 10 times the capacity required for discharge (i.e. ORR) steps in the cycling procedures described below.

The cell depicted in **Figure 4.1**b was employed for electrochemical testing of the gas diffusion electrode. The electrode was exposed to the electrolyte on the inner side and ambient air on the outer side through 1.65 cm diameter circular holes in the adjacent gaskets and plates. The Ni/PTFE slurry-deposited side of the electrode faced the air and the non-slurry-deposited side faced the electrolyte. A microporous polypropylene separator (Celgard 5550) separated the zinc counter electrode from the gas diffusion electrode. An additional microporous separator was also placed directly adjacent to the gas diffusion electrode on the electrolyte side; this ensured that

oxygen gas evolved during OER exited through the air-side of the cell rather than bubbling into the electrolyte. However, it should be noted that this separator placement caused slightly higher OER potentials (approximately 0.1 V higher) to be observed, possibly due to some oxygen bubbles becoming stuck between the electrode surface and separator and reducing electrolyte coverage of the electrode. The distance between the zinc wire reference electrode and gas diffusion electrode was approximately 2 mm.

The cell depicted in **Figure 4.1**c was used for electrochemical testing of the thin-layer electrode. The electrode in this cell was not exposed to the air; oxygen exposure was instead provided via dissolved oxygen in an oxygen-saturated electrolyte. A magnetic stir bar in the cell was rotated at 500 rpm to facilitate electrolyte wetting and oxygen transport to the electrode, which was exposed to the electrolyte through a 1.05 cm diameter opening. As will be discussed in more detail, this design was mainly employed to avoid time-sensitive potential losses caused by electrolyte flooding into the gas pores of the thicker gas diffusion electrode. A distance over 1 cm separated the zinc wire reference electrode and thin-layer electrode in this cell; however, IR-compensation was employed for polarization experiments using both designs to negate any associated potential drops in the electrolyte.

4.2.3 Electrochemical Testing

Galvanostatic charge/discharge cycling of the gas diffusion electrode was conducted on a Neware BTS3000 battery tester, while galvanostatic electrochemical impedance spectroscopy (EIS) and potentiodynamic polarization experiments were conducted on a Bio-Logic VSP potentiostat. All potentials herein are reported relative to the zinc wire reference electrode

(Zn/ZnO). Several reactions occurred on the air electrodes in each experiment, including ORR and OER (**Equation 4.1**), NiOOH reduction and $Ni(OH)_2$ oxidation (**Equation 4.2**) and nickel metal oxidation (**Equation 4.3**). Each reaction and its standard equilibrium potential[247,281] relative to Zn/ZnO in alkaline electrolyte is provided below.

$$O_2 + 2H_2O + 4e^- \leftrightarrow 4OH^-, \quad E° = 1.66\ \text{V vs. Zn/ZnO} \qquad \textbf{(Equation 4.1)}$$

$$NiOOH + H_2O + e^- \leftrightarrow Ni(OH)_2 + OH^-, \ E° = 1.75\ \text{V vs. Zn/ZnO} \qquad \textbf{(Equation 4.2)}$$

$$Ni + 2OH^- \rightarrow Ni(OH)_2 + 2e^-, \quad E° = 0.54\ \text{V vs. Zn/ZnO} \qquad \textbf{(Equation 4.3)}$$

Galvanostatic cycling was used to evaluate the rechargeability of the nickel-based gas diffusion electrode at 10 mA cm^{-2}. The exact test sequence is shown in **Table 4.1** and is also demonstrated graphically in **Figure 4.2**. Unlike a typical cycling experiment, two-step reduction (corresponding to battery discharge) and two-step oxidation (battery charge) cycles were employed to separately evaluate the oxygen reactions (**Equation 4.1**) and the NiOOH/$Ni(OH)_2$ reactions (**Equation 4.2**). This was possible due to the relatively smaller overpotentials of the NiOOH/$Ni(OH)_2$ reactions, which enabled cut-off potentials used in the first step of the reduction or oxidation cycle to indicate when these reactions were approximately completed. Since the ORR potential was never higher than 1.3 V vs. Zn and the OER potential was never lower than 1.95 V vs. Zn at 10 mA cm^{-2}, cut-off potentials of 1.3 V and 1.95 V vs. Zn were used respectively during reduction and oxidation to determine the approximate capacity of **Equation 4.2**. This capacity is assumed to be proportional to the volume or thickness of the nickel (oxy)hydroxide film in each

cycle. Therefore, changes of the $NiOOH/Ni(OH)_2$ capacity could be compared with changes of the ORR or OER overpotentials to determine if there is a correlation between the film growth and the electrode's catalytic performance. After the electrode potential passed these cut-off voltages, reduction continued for 15 minutes to evaluate the ORR potential or 17 minutes to evaluate the OER potential. Extra time was allocated to the oxidation step to ensure the Zn counter electrode's capacity did not rapidly drop during cycling, since some of the deposition current at the Zn electrode is lost to hydrogen evolution. While the hydrogen quantity evolved from the Zn electrode during this step was not quantified, 2 extra minutes was determined to be suitable based on visual observation that the Zn electrode's size did substantially change after the cycling procedure. During the rest steps in this procedure, the gradual recovery of the open circuit potential as shown in **Figure 4.2** can be attributed to the slow rebalancing of the oxygen and/or hydroxide concentration gradients established during oxidation or reduction steps.[282,283]

Table 4.1. Galvanostatic Cycling Procedure for Nickel-Based Gas Diffusion Electrode.

Step	Operation	Duration/End Condition	Dominant Reaction
1	Rest	5 min	
2	Reduction @ 10 mA cm^{-2}	Cut-off @ 1.3 V	Eq. 4.2 (forward)
3	Reduction @ 10 mA cm^{-2}	15 min or cut-off @ 0.1 V	Eq. 4.1 (forward)
4	Rest	5 min	
5	Oxidation @ 10 mA cm^{-2}	Cut-off @ 1.95 V	Eq. 4.2 (reverse), Eq. 4.3
6	Oxidation @ 10 mA cm^{-2}	17 min	Eq. 4.1 (reverse)
7	Loop to Step 1		

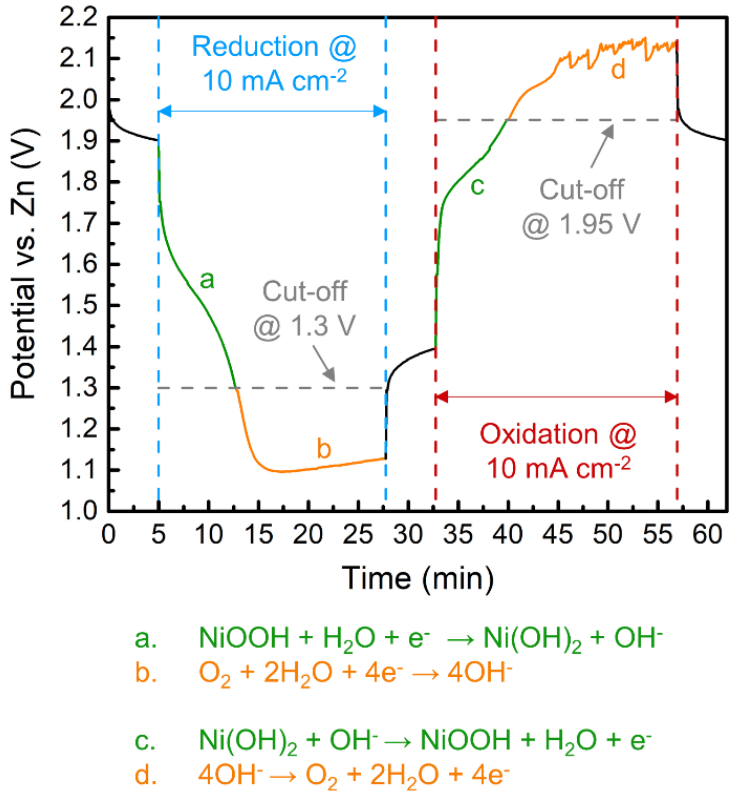

Figure 4.2. Graphical demonstration of two-step reduction and two-step oxidation cycles and the dominant reactions occurring at each step.

In the next electrochemical experiment, galvanostatic cycling was employed together with galvanostatic EIS on the gas diffusion electrode (**Table 4.2**). This was used to measure changes of the ohmic resistance of the cell and impedance characteristics of the ORR as cycling progressed. For each cycle, a 60-minute reduction step at 10 mA cm^{-2} was used prior to each EIS measurement to ensure the NiOOH film was fully reduced to $Ni(OH)_2$ and that the air electrode had reached a stable potential. The galvanostatic EIS measurement was conducted at 10 mA cm^{-2} with a frequency range from 100 kHz to 10 mHz and an amplitude of 2 mA cm^{-2}.

Table 4.2. Galvanostatic Cycling and EIS Procedure for Nickel-Based Gas Diffusion Electrode.

Step	Operation	Duration	Dominant Reactions
1	Rest	5 min	
2	Reduction @ 10 mA cm^{-2}	60 min.	Eq. 1 (forward), Eq. 2 (forward)
3	Reduction @ 10 mA cm^{-2} with EIS	~ 30 min.	Eq. 1 (forward)
4	Rest	5 min.	
5	Oxidation @ 10 mA cm^{-2}	90 min.	Eq. 1 (reverse), Eq. 2 (reverse), Eq. 3
6	Loop to Step 1		

Cyclic potentiodynamic polarization experiments were then conducted on the gas diffusion and thin-layer electrodes according to the protocol outlined in **Table 4.3**. To evaluate the effect of (oxy)hydroxide film growth on the ORR kinetics, the polarization curves were recorded after various cumulative times of oxidation at 2.2 V vs. Zn. Like the previous experiments, multi-step oxidation and reduction reactions were applied to distinguish the oxygen reactions from the $NiOOH/Ni(OH)_2$ reactions. An additional galvanostatic reduction step at 1 mA cm^{-2} with an appropriate cut-off voltage and a following potentiostatic reduction step at the cut-off voltage were applied to ensure that NiOOH reduction and any associated capacitive currents[284] were fully completed prior to recording the ORR polarization curves. IR-correction to the polarization curves was applied using ohmic resistance measurements at the starting potential and 85% correction to the applied potentials. The remaining 15% correction was applied to the polarization data afterwards.

Table 4.3. Cyclic Potentiodynamic Polarization Procedure for the Nickel-Based Gas Diffusion Electrode (GDE) and Thin-Layer Electrode (TLE).

Step	Operation	Duration/End Condition	Dominant Reaction
1	Rest	5 min.	
2	Reduction @ 10 mA cm^{-2}	Cut-off @ 1.3 V (GDE), @ 1.2 V (TLE)	Eq. 2 (forward)
3	Reduction @ 1 mA cm^{-2}	Cut-off @ 1.35 V (GDE), @ 1.325 V (TLE)	Eq. 2 (forward)
4	Reduction @ 1.35 V vs. Zn (GDE), @ 1.325 V vs. Zn (TLE)	60 min.	Eq. 1 (forward), Eq. 2 (forward)
5	IR-corrected potentiodynamic polarization	1.35 V to 0.875 V @ 0.25 mV s^{-1} (GDE), 1.325 V to 0.8 V @ 0.1 mV s^{-1} (TLE)	Eq. 1 (forward)
6	Rest	5 min.	
7	Oxidation @ 10 mA cm^{-2}	Cut-off @ 1.95 V vs. Zn	Eq. 2 (reverse)
8	Oxidation @ 2.2 V vs. Zn	Variable duration	Eq. 1 (reverse), Eq. 2 (reverse), Eq. 3
9	Loop to Step 1		

4.3 Results and Discussion

The morphology of the nickel particles used to fabricate the nickel-based air electrodes are shown in **Figure 4.3**a. Carbonyl nickel particles were selected due to their rough texture which provided a high surface area for catalyst deposition. The Ni/PTFE slurry-deposited side of the electrode is shown at low magnification in **Figure 4.3**b, revealing a smooth surface with several

micropores allowing for gas diffusion. The higher magnification SEM image in **Figure 4.3**c shows the PTFE-bonded nickel particles more clearly. **Figure 4.3**d,e show the nickel foam morphology at low and high magnification on the non-slurry side of the electrode. After the Co/Ni nitrate dip-coating procedure, the $NiCo_2O_4$ catalyst particles displayed a nanoflake structure (**Figure 4.3**f).

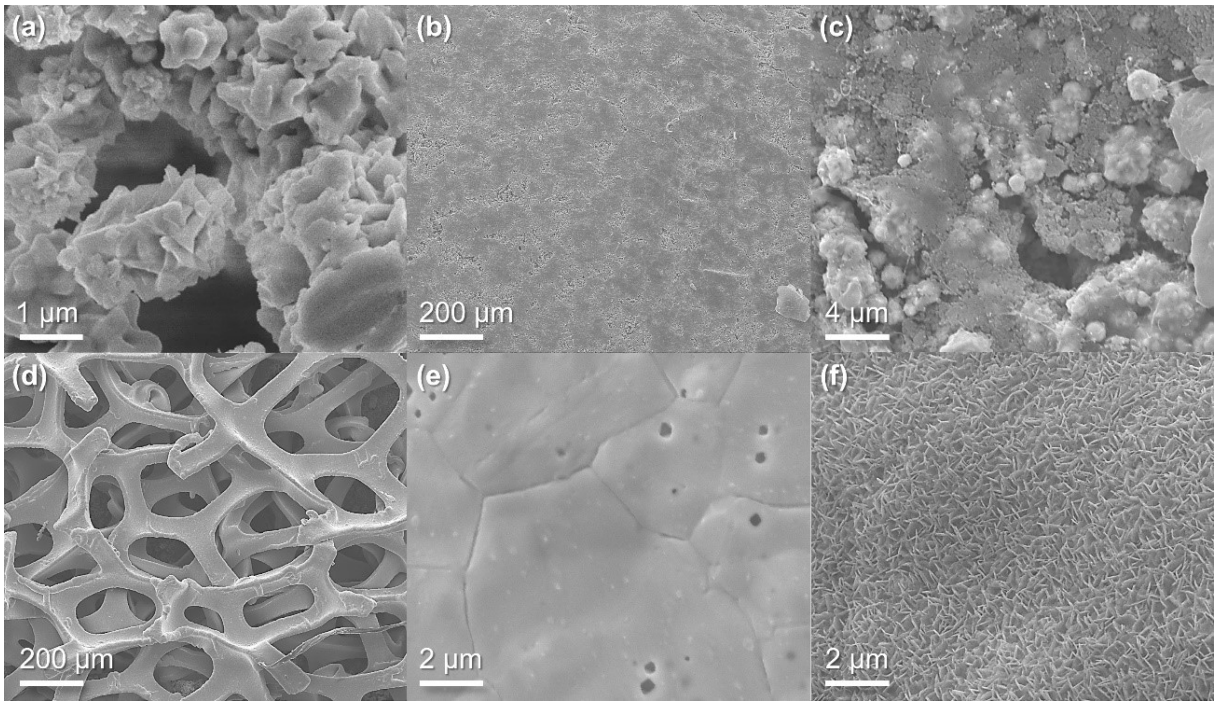

Figure 4.3. SEM images of (a) the nickel particle morphology; the Ni/PTFE slurry-deposited side of the electrode at (b) low magnification and (c) high magnification; the non-slurry side of the electrode at (d) low magnification, (e) high magnification and (f) high magnification after deposition of the $NiCo_2O_4$ catalyst.

Galvanostatic cycling test results for the gas diffusion electrode are provided in **Figure 4.4**. The electrode was subjected to 100 cycles of the test protocol outlined in **Table 4.1**, with the potential variations for cycles 1-10, 51-60 and 91-100 shown in **Figure 4.4**a. The ORR potential

at the end of each cycle decreased from 1.24 V to 1.17 V vs. Zn within the first ten cycles, and fell further to 1.04 V by the end of the 50th cycle. After the 50th cycle, the ORR potential started to decline more rapidly, and after approximately 75 cycles it consistently fell below the lower cut-off voltage of 0.1 V vs. Zn. The OER potential displayed fluctuating potentials within each cycle, which has been previously observed[129,273] and could be explained by the growth and detachment of oxygen bubbles disrupting the solid/electrolyte interface. However, the OER potentials remained relatively consistent throughout the 100 cycles. Therefore, the remainder of the investigation was focused on uncovering the origin(s) of ORR kinetic losses.

Figure 4.4b displays oxidation and reduction transients at various cycle numbers. For the first reduction and oxidation cycles, the electrode potential quickly attained stable values in the expected potential ranges for ORR and OER, indicating that very little nickel oxidation had yet occurred. However, subsequent cycles displayed an initial period of lower overpotentials before a stabilized ORR or OER potential was established. The profiles for the 10th, 40th and 100th cycles show that this low-overpotential period became increasingly longer as cycling progressed, indicating a continual increase of the conversion capacity between $Ni(OH)_2$ and NiOOH. This demonstrates the importance of using sufficiently long cycles for ORR/OER evaluation of nickel-based air electrodes, since the NiOOH/$Ni(OH)_2$ conversion reactions must be completed before measuring the oxygen reaction potentials.

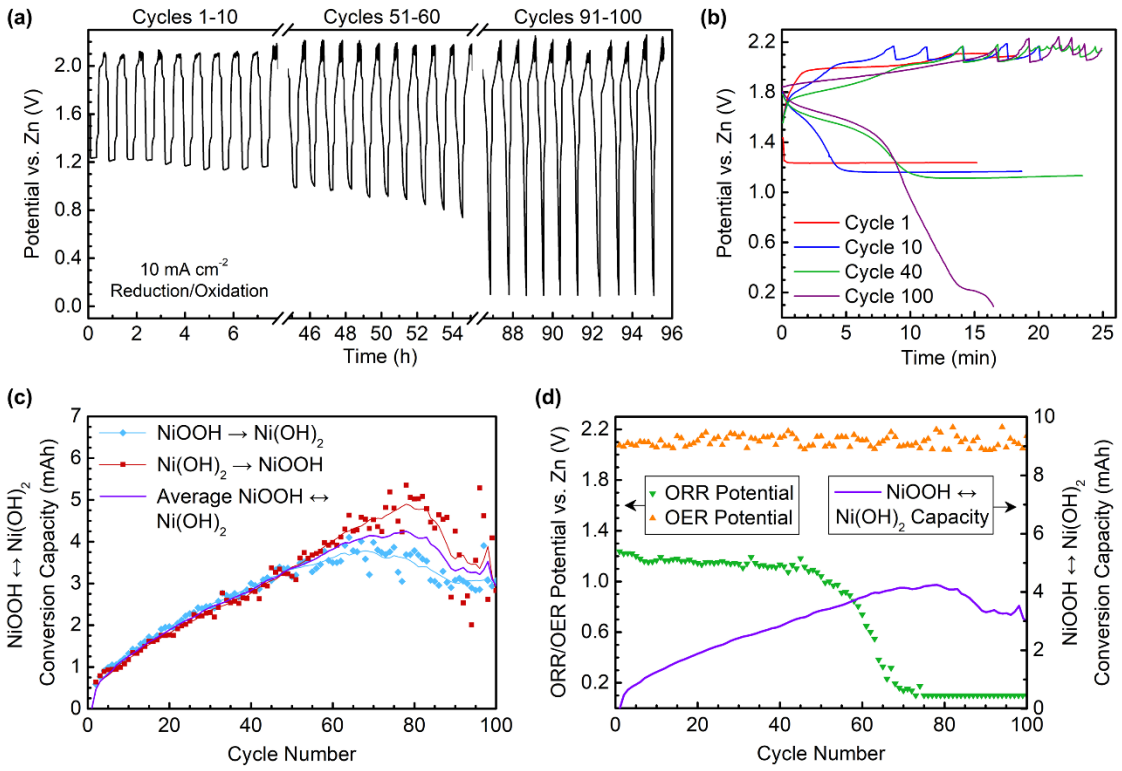

Figure 4.4. Galvanostatic cycling (procedure per **Table 4.1**) for nickel-based gas diffusion electrode: (a) Galvanostatic cycling potentials, (b) oxidation and reduction transients at different cycle numbers, (c) NiOOH→$Ni(OH)_2$ and $Ni(OH)_2$→NiOOH conversion capacities with 10-point adjacent-average smoothed lines, (d) ORR/ OER potentials and average NiOOH/$Ni(OH)_2$ capacity as a function of cycle number.

The capacities of the NiOOH→$Ni(OH)_2$ conversion reaction (measured by the capacity of the reduction step before the potential fell below 1.3 V vs. Zn) and the $Ni(OH)_2$→NiOOH conversion reaction (measured by the capacity of the oxidation step before the potential rose above 1.95 V vs. Zn) are shown as a function of cycle number in **Figure 4.4**c. Both capacity measurements rose quickly above an assumed initial value of zero during the first 5 cycles, and then continued to rise almost linearly at a more gradual rate. After the 50th cycle, the measured

capacities started to diverge, with the $NiOOH \rightarrow Ni(OH)_2$ conversion reaction displaying apparently lower values. This was likely caused by the rapidly decreasing ORR activity, since the potential above 1.3 V (although mainly attributable to the $NiOOH \rightarrow Ni(OH)_2$ conversion reaction) may be partially dictated by the ORR activity. After the 80^{th} cycle, both measured capacities appeared to reach a maximum, suggesting that Ni (oxy)hydroxide growth stopped at this point. The ORR and OER potentials observed at the end of each cycle, along with the average measured $NiOOH/Ni(OH)_2$ capacity during each cycle, are plotted together in **Figure 4.4**d. Although the ORR potential decreased and the $NiOOH/Ni(OH)_2$ capacity increased during the 100 cycles, no direct correlation between the two measurements as a function of cycle number was evident here.

To view morphological changes which may have contributed to the steep drop in ORR activity, SEM images of the gas diffusion electrode were taken before and after 100 cycles of the protocol outlined in **Table 4.1**. **Figure 4.5**a and **Figure 4.5**b respectively show the non-slurry and slurry-deposited side of the electrode before cycling, and **Figure 4.5**c and **Figure 4.5**d respectively show the non-slurry and slurry-deposited side of the electrode after 100 cycles. Before cycling, the $NiCo_2O_4$ catalyst flakes are clearly visible on both sides of the electrode. However, after 100 cycles, both sides of the electrode appeared to be covered by a spongey film and the $NiCo_2O_4$ flakes were no longer visible, suggesting the film grew overtop of the catalyst.

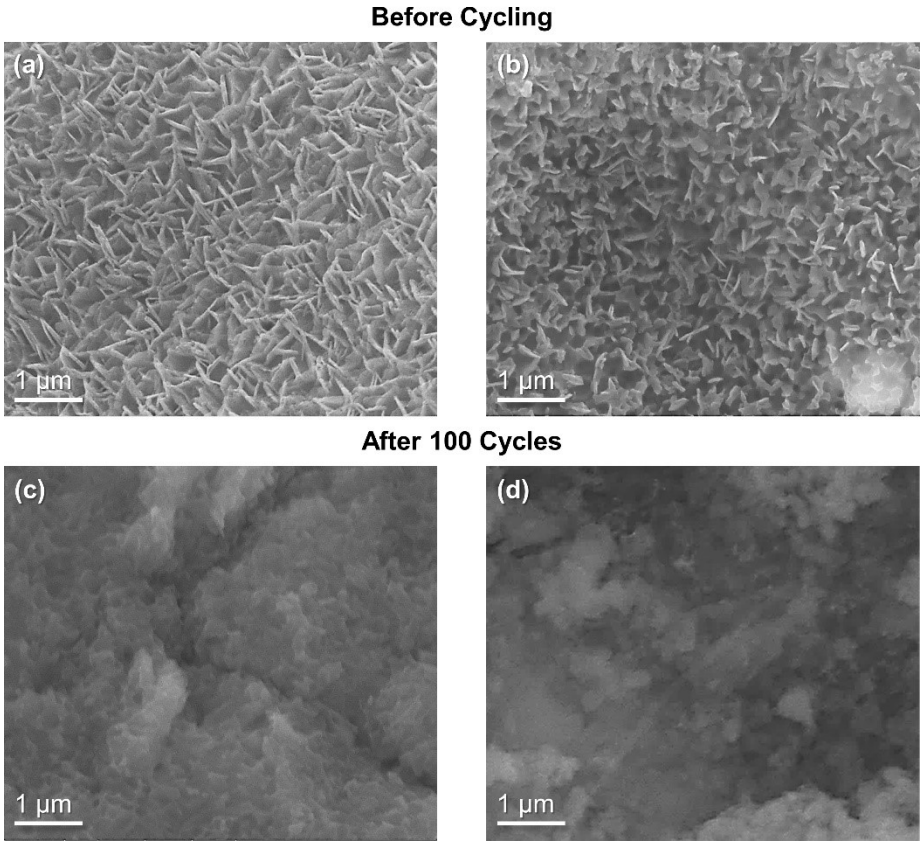

Figure 4.5. SEM images of the nickel-based gas diffusion electrode: (a) non-slurry side and (b) slurry-deposited side before cycling; (c) non-slurry side and (d) slurry-deposited side after 100 galvanostatic oxidation/reduction cycles (**Table 4.1**).

XRD spectra of the electrode surface before cycling and after 10 and 100 cycles were recorded to try to identify the material phases observed visually in SEM. The largest peaks observed on all samples were those of metallic nickel (JCPDS # 04-0850), as shown in **Figure 4.6**. Smaller peaks corresponding to $NiCo_2O_4$ (JCPDS # 20-0781) were also observed on each sample, and their intensities became progressively smaller after cycling, which is consistent with observation in **Figure 4.5** of the $NiCo_2O_4$ catalyst becoming covered by the overlying film.

However, diffraction peaks corresponding to the $Ni(OH)_2$ or NiOOH phases which were expected to constitute the film observed in SEM were not detected. This could be explained by previous observations that nickel (oxy)hydroxides grown electrochemically have poor crystalline ordering.[285] After 100 cycles, new peaks corresponding to the metastable ε-$Zn(OH)_2$ phase were observed. This phase likely resulted from precipitation of the $Zn(OH)4^{2-}$ ion from the electrolyte.[286,287]

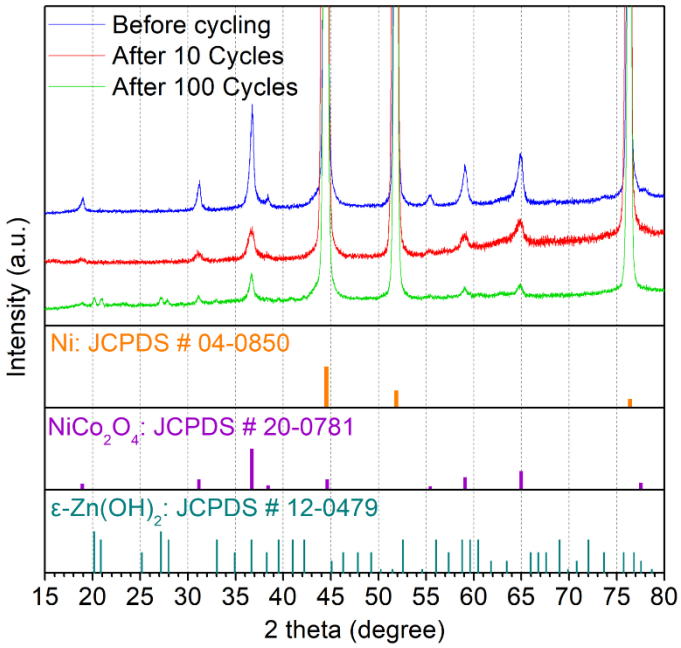

Figure 4.6. XRD spectra of the nickel-based gas diffusion electrode surface before cycling and after 10 and 100 galvanostatic oxidation/reduction cycles (**Table 4.1**).

To further study the chemical changes of the nickel-based air electrode surface, XPS was performed before and after 10 and 100 cycles of the protocol outlined in **Table 4.1**. As shown in the survey spectra (**Figure 4.7**a), peaks corresponding to Co, Ni and O (from the $NiCo_2O_4$ catalyst)

and C and F (from the PTFE binder) were observed before cycling. After cycling, the Co peaks became progressively weaker while the Ni peaks became stronger especially after 100 cycles. Peaks corresponding to residual Zn from the ZnO-saturated electrolyte were also present after cycling. **Figure 4.7**b shows the evolution of the electrode surface's elemental composition before and after cycling. The most important observation was a dramatic reduction of the Co content after cycling, indicating a reduced presence of the $NiCo_2O_4$ catalyst flakes on the surface which is consistent with the SEM and XRD results. Concurrently, the Ni content increased after 100 cycles, and would have also increased after 10 cycles if the quantification of residual Zn from the electrolyte was ignored. This, together, with the progressively increased O content after cycling, indicates the growth of an oxidized and/or hydrated Ni film overtop of the $NiCo_2O_4$ catalyst. The reduction of C and F were likely caused by the growing Ni-rich film overtop of the PTFE binder. Also, the fact that the Zn content only slightly increased between 10 to 100 cycles means that it was unlikely to have played a major role in the severe ORR potential losses observed between cycles 50 to 70 in **Figure 4.4**d, even if it had precipitated on the electrode surface during cycling and not after removal of the electrode from the cell.

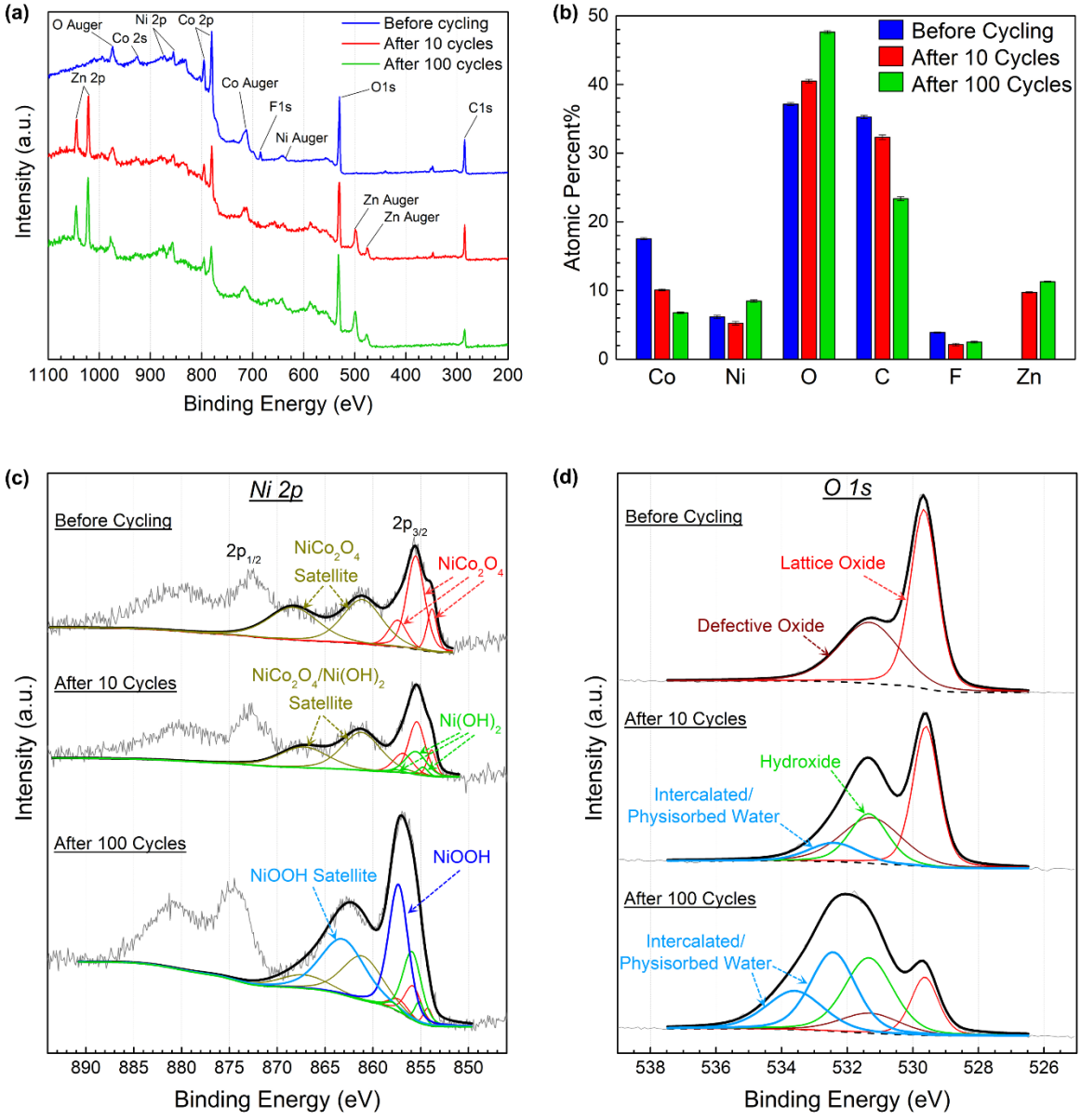

Figure 4.7. XPS analysis of the nickel-based gas diffusion electrode before and after 10 and 100 galvanostatic oxidation/reduction cycles (**Table 4.1**): (a) Survey spectra, (b) quantified chemical composition of electrode surfaces where the error bars represent the uncertainty (one standard deviation) of the quantified measurement,[288,289] (c) high-resolution deconvoluted Ni 2p spectra, (d) high-resolution deconvoluted O 1s spectra.

The high-resolution XPS spectra of the Ni 2p and O 1s peaks were investigated and deconvoluted to gain better insight into the chemical state of the Ni-rich film which grew on the electrode surface after cycling. The Ni 2p spectra, for which only the $2p_{3/2}$ spectra were deconvoluted, are presented in **Figure 4.7**c. The spectrum recorded before cycling was fitted with a multiplet envelope of three main peaks and two satellite peaks assigned to $NiCo_2O_4$.[290] After 10 cycles, the main peak in the $2p_{3/2}$ spectral pattern was noticeably broadened, which was well-fitted by adding the two major peaks of the multiplet envelope for $Ni(OH)_2$[290] and reducing the main $NiCo_2O_4$ peak intensities. This confirms the growth of a Ni (oxy)hydroxide film (observed as $Ni(OH)_2$ here, since the electrode was analyzed after the electrochemical reduction steps in **Table 4.1**) overtop of the $NiCo_2O_4$ catalyst in the early cycling stages. The spacing and relative sizes and shapes of the deconvoluted $NiCo_2O_4$ peaks remained largely unchanged in the optimized fitting, meaning that their chemical states did not appear to be altered after growth of the $Ni(OH)_2$ film. After 100 cycles, the main peak and satellite peak structures became larger and significantly shifted to higher binding energies. This spectrum was fitted by adding a main peak around 857 eV corresponding to NiOOH[291–293] and a new satellite peak around 863 eV, using fixed full width at half maximum values previously reported for electrochemically prepared γ-NiOOH.[294] The presence of NiOOH together with $Ni(OH)_2$ after 100 cycles means that the Ni (oxy)hydroxide film was not fully reduced to $Ni(OH)_2$ after it grew significantly thick, which could mean the film continued to grow even after its capacity appeared to plateau in **Figure 4.4**c.

The high-resolution O 1s spectra are shown in **Figure 4.7**d. The first spectrum before cycling was deconvoluted into two peaks corresponding to lattice oxides (529.7 eV) and defective oxides

(531.3 eV) in the $NiCo_2O_4$ catalyst.[290,295,296] After 10 cycles, the low-binding energy peak of the spectrum decreased while the high-binding energy peak increased, which was fitted by adding a sharper hydroxide peak at 531.3 eV.[296,297] An additional peak at 532.4 eV corresponding to physisorbed or intercalated water[298,299] was also necessary to produce an accurate fitting. After 100 cycles, the lattice oxide peak was significantly reduced while the hydroxide and water peaks were enhanced. An additional higher-binding energy water peak that has been previously noted in oxyhydroxide compounds[290] was also needed to fit the spectral data. $Zn(OH)_4^{2-}$ dissolved in this bound or intercalated water within the nickel (oxy)hydroxide film likely gave rise to the metastable ε-$Zn(OH)_2$ phase observed in XRD analysis (**Figure 4.6**). More importantly, intercalated water in the nickel (oxy)hydroxide film might play a role in preventing mass transfer of oxygen to the underlying $NiCo_2O_4$ catalyst, thus causing reduced ORR kinetics after cycling. Regardless, the nickel (oxy)hydroxide film observed with SEM and XPS is proposed to be the principal cause of potential degradation observed during galvanostatic cycling, since it likely increases the resistance of oxygen diffusion to the $NiCo_2O_4$ catalyst.

For deeper electrochemical insight on the increasing ORR overpotentials, galvanostatic cycling with EIS measurements at a reduction current of 10 mA cm^{-2} were conducted according to **Table 4.2** on a new gas diffusion electrode. The first important observation is that the ohmic resistance, indicated by the high-frequency real impedance intercepts (**Figure 4.8** inset), did not substantially increase as cycling progressed. This resistance was 1.3 Ω cm^2 during the first cycle and 2.5 Ω cm^2 during the 50^{th} cycle, corresponding to a very minor 12 mV increase of the ohmic drop at 10 mA cm^{-2}. Therefore, ohmic resistance (within the electrolyte, electrode or current

collectors) could not have accounted for the large ORR potential loss observed in **Figure 4.4**a,b,d. Secondly, it should be noted that each of the EIS plots in **Figure 4.8** begin at an approximate 45° angle. EIS curves typically begin at a 45° angle for diffusion-limited systems and a 90° angle for charge transfer-limited systems,[300] meaning that the electrodes studied here were likely limited by diffusion at 10 mA cm^{-2}. The EIS spectra appeared as two depressed semicircles, especially visible after higher cycle numbers, which is characteristic of porous electrodes.[301] Similar EIS spectra for gas diffusion electrodes have previously been modeled by a modified Randles circuit with one or more finite diffusion elements in series with the charge transfer resistance term.[251,300,301] Arai et al.[300] determined that, in a carbon-based air electrode, the high-frequency (leftmost) semicircle was indicative of ionic diffusion resistance while the low-frequency (rightmost) semicircle was indicative of oxygen diffusion resistance. In this case, the low-frequency (rightmost) semicircle appeared to experience the most growth as cycling progressed. This suggests that increased oxygen diffusion resistance was responsible for most of the ORR potential loss observed in **Figure 4.4**a,b,d.[301]

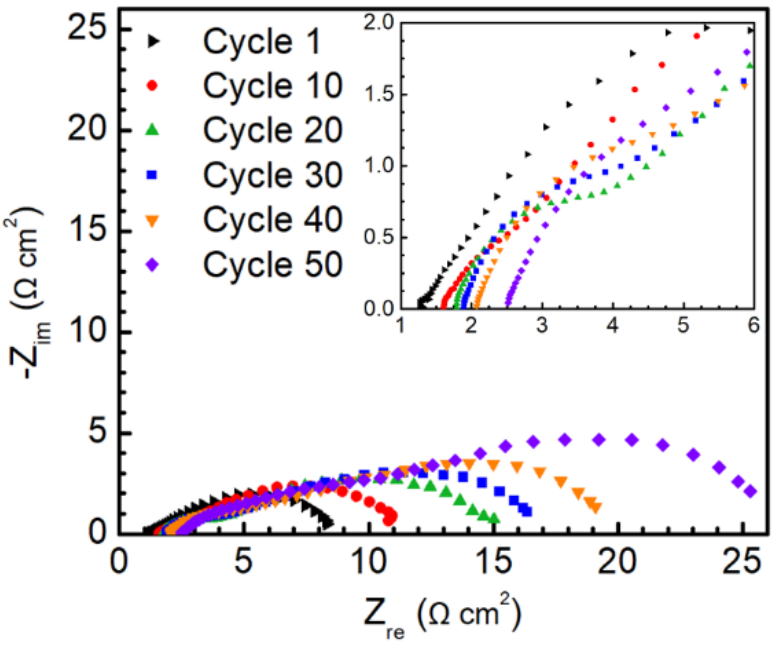

Figure 4.8. Galvanostatic EIS plots (procedure per **Table 4.2**) for nickel-based gas diffusion electrode.

Cyclic potentiodynamic polarization experiments were conducted on the gas diffusion electrode to directly investigate the role of activation loss (measured by analysis of the Tafel region) and mass transfer loss (measured by the limiting currents). The IR-corrected ORR polarization curves, which were measured as part of the procedure outlined in **Table 4.3**, are displayed in **Figure 4.9**a. **Figure 4.9**b shows the Tafel region of the ORR polarization curves measured after different cumulative times of oxidation at 2.2 V. Tafel slopes observed for the ORR on spinel catalysts in alkaline electrolytes have a minimum value of approximately 40 mV dec^{-1}.[302–304] This is consistent with a theoretical value of 39 mV dec^{-1} (2.303RT/αF, α=1.5),[305] which is predicted for the ORR where the second electron-transfer step of the 4-electron pathway is rate-

determining.[306] Doubled Tafel slopes are often observed on porous air electrodes due to oxygen transport limitations within porous aggregates,[243,244,305,307] which would explain the initial value of 76 mV dec^{-1} observed in **Figure 4.9**b. The shift from the normal Tafel slope to the double Tafel slope likely occurred at a potential above the polarization range.

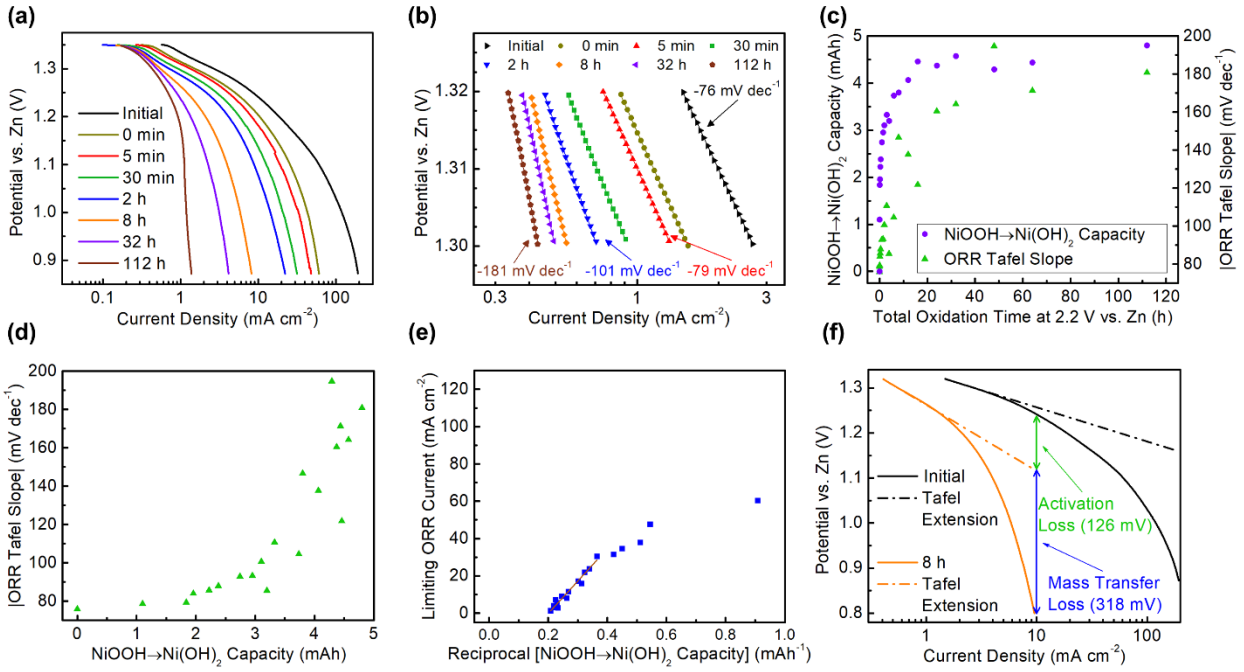

Figure 4.9. Cyclic potentiodynamic polarization (procedure per **Table 4.3**) for nickel-based gas diffusion electrode: (a) Full IR-corrected ORR polarization curves and (b) ORR Tafel plots after various total oxidation times at 2.2 V, (c) dependence of NiOOH→Ni(OH)$_2$ capacity and ORR Tafel slope magnitude on the total oxidation time at 2.2 V, (d) dependence of ORR Tafel slope magnitude on NiOOH→Ni(OH)$_2$ capacity, (e) dependence of limiting ORR current on the reciprocal of NiOOH→Ni(OH)$_2$ capacity with line of best fit over linear region, (f) ORR polarization curves before and after oxidation at 2.2 V for 8 h with extrapolation of the Tafel regions.

The first oxidation cycle (oxidized at 10 mA cm^{-2} until reaching the cut-off of 1.95 V and skipping step 8 of **Table 4.3**) and second oxidation cycle (5 min at 2.2 V) caused the $NiOOH/Ni(OH)_2$ capacity to quickly increase from zero to 1.1 mAh and 1.8 mAh, respectively (**Figure 4.9**c). The Tafel slope remained close (79 mV dec^{-1}) to its initial value after 5 min of charging (**Figure 4.9**b); however, the recorded current densities shifted negatively, which likely indicates the transition to a doubled Tafel slope occurred at a higher potential compared to the initial polarization curve. This could be attributed to the nickel (oxy)hydroxide film growing inside the pores of the catalyst-coated nickel aggregates, causing increased internal oxygen diffusion resistance and thus a transition to a doubled Tafel slope at a smaller ORR overpotential.[244] After greater oxidation time periods, currents in the Tafel region were further reduced. While this is partially explained by a further negative shift of the Tafel regions, it was also due to increasing Tafel slope magnitudes which reached nearly 200 mV dec^{-1} (**Figure 4.9**b). The dependence of both the $NiOOH/Ni(OH)_2$ capacity and ORR Tafel slope magnitude on the total oxidation time is shown in **Figure 4.9**c. Both values displayed relatively rapid increases within the first 8 h of oxidation at 2.2 V, followed by more gradual increases during the remaining 104 h.

An increasing Tafel slope could be attributed to two different factors, which in turn may be at least partially attributed to the growing nickel (oxy)hydroxide film. Firstly, if the rate-determining step of the ORR is changed from the second electron transfer step to the previous step (between the first and second electron transfers) involving adsorbed superoxide exchange with a surface hydroxide on the catalyst surface,[306] the theoretical Tafel slope would change from 39 mV dec^{-1} to 59 mV dec^{-1} ($2.303RT/\alpha F$, $\alpha=1.0$),[305] or an increase of 1.5 times. This may be caused

by the increased presence of $Ni(OH)_2$ or NiOOH surfaces, which have relatively slow redox reaction kinetics to support superoxide exchange.[308] Secondly, the Tafel slope (already presumed to be doubled due to oxygen transport limitations, as mentioned two paragraphs above) could be doubled again if both oxygen and ionic transport resistances become significant within the porous nickel aggregates of the electrode.[244] Ionic transport limitations within the porous aggregates are expected to occur due to reduced pore sizes between the Ni particles resulting from growth of the nickel (oxy)hydroxide film. Contributions from both factors would be needed to explain the Tafel slope increases observed in **Figure 4.9**b, since the first factor or second factor alone (i.e. only one of these factors considered together with the already doubled Tafel slope mentioned two paragraphs above) would result in a maximum Tafel slope of only 118 mV dec^{-1} ($2\times2.303RT/\alpha F$, $\alpha=1.0$) or 158 mV dec^{-1} ($2\times2\times2.303RT/\alpha F$, $\alpha=1.5$), respectively.[244,305] **Figure 4.9**d displays the relationship between the ORR Tafel slope magnitude and the $NiOOH/Ni(OH)_2$ capacity, where a relatively minor positive dependence is observed within the first 3 mAh of growth followed by an approximate doubling of the Tafel slope as the $NiOOH/Ni(OH)_2$ capacity approaches its maximum (limiting) value. The doubling of the Tafel slope during the latter period is consistent with the explanation of it being caused by significant ionic transport limitations (second factor above); this is reasoned because ionic transfer limitations are also likely to cause the nickel (oxy)hydroxide film's growth to become limited during this period, since hydroxide ions are required for the nickel oxidation reaction (**Equation 4.3**) to continue. This leaves the initial Tafel slope increase within the first 3 mAh of growth to be explained by a change of the rate-determining step (first factor above).

From the analysis in the previous paragraph, it appears likely that the nickel (oxy)hydroxide film plays a significant role in increasing activation losses of the nickel-based air electrode. However, it should be noted that the Tafel plots shown in **Figure 4.9**b do not maintain the same slope over at least 1 decade of current. This is further shown in **Figure 4.10** where, for each polarization curve, any three consecutive datapoints having a slope that differs by less than 1% of the measured Tafel slope in **Figure 4.9**b are indicated by enlargement of the middle of the three datapoints. Normally, reliable observance of Tafel behaviour requires the same Tafel slope to be measured across at least one decade of current density.[309] Since the polarization curves begin at 1.35 V vs. Zn, rather than a higher value (due to the prior steps 1-3 shown in **Table 4.3** required to reduce the NiOOH to $Ni(OH)_2$), a less-than-ideal range of the Tafel region was observed in this work. As shown in **Figure 4.10**, none of the Tafel plots in **Figure 4.9**b maintain the same measured slope (within 1% deviation) for more than one decade of current; mass transfer polarization losses cause the slope to increase before 1 full decade of current in the Tafel region can be observed. Therefore, improved measurements of the Tafel regions over 1 decade of current would be needed to have full confidence in the Tafel slopes discussed above (especially for the slopes measured beyond 8 h of total oxidation time, where **Figure 4.10** makes it evident that mass transfer polarization losses may have interfered with the Tafel slopes measured between 1.30-1.32 V). However, as will be discussed in the following paragraphs, mass transfer losses were found to dominate the polarization losses at the current density of 10 mA cm^{-2} focused on in this work. Thus, the activation losses characterized by Tafel slope measurements are not critical to understanding the main cause of failure shown in **Figure 4.4** for the nickel-based air electrode.

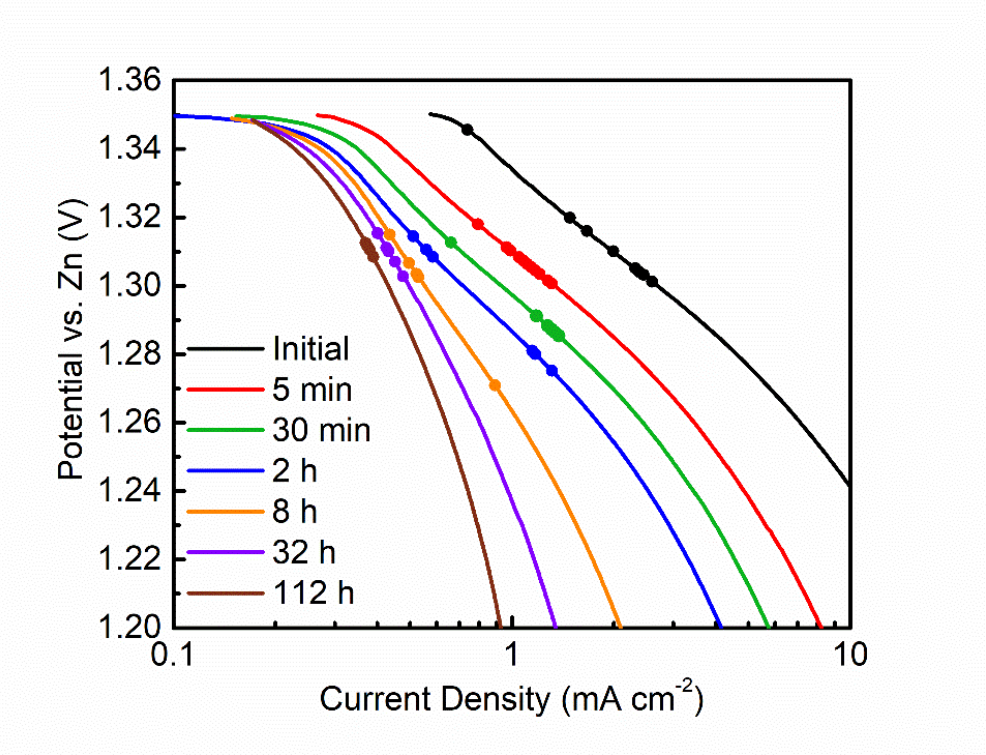

Figure 4.10. Magnified ORR polarization curves from **Figure 4.9**a. In these curves, any three consecutive datapoints having a slope that differs by less than 1% of the measured Tafel slope in **Figure 4.9**b are indicated by enlargement of the middle of the three datapoints.

The ORR polarization curves in **Figure 4.9**a display substantial reductions of the limiting current as the oxidation time is increased, revealing significantly increased mass transfer losses. Based on the SEM and XPS observations that the nickel (oxy)hydroxide film grows overtop of the $NiCo_2O_4$ catalyst, increased mass transfer losses are expected since oxygen must diffuse through an increasingly thicker film before undergoing reduction at the catalyst surface. If the nickel (oxy)hydroxide film is the dominating source of diffusion resistance, the limiting current will be inversely proportional to the film's thickness.[243,310] To confirm this, the limiting current measured

at 0.875 V vs. Zn was plotted against the reciprocal of the measured $NiOOH/Ni(OH)_2$ capacity (which is assumed to be proportional to its thickness) in **Figure 4.9**e. A linear correlation was indeed observed at high capacities (low reciprocal values), indicating that the nickel (oxy)hydroxide film was likely the dominant source of diffusion resistance when it became significantly thick. At low nickel (oxy)hydroxide thickness (high reciprocal capacity), deviation of the measured limiting currents from the linear pattern indicates that the porous PTFE/electrolyte/gas network in the air electrode (schematically shown in **Figure 4.1**a) was the initial dominant source of diffusion resistance.

Figure 4.9f compares the ORR polarization curves before oxidation (initial) and after 8 h of oxidation, including dashed lines for extrapolation of the Tafel slopes. This enables a comparison of the relative contributions of activation and mass transfer overpotential at different current densities. At 10 mA cm^{-2}, which was the current density for the galvanostatic oxidation/reduction experiments (**Figure 4.4**), mass transfer losses are the more significant source of overpotential after 8 h. After longer oxidation times, mass transfer losses are even more significant. Therefore, the rapid potential loss observed after 50 cycles in **Figure 4.4**d likely occurred when the limiting current approached and fell below 10 mA cm^{-2}. Even for shorter oxidation times, mass transfer losses were always responsible for at least 65% of the total potential loss from the initial performance at 10 mA cm^{-2}, indicating the high significance of performance degradation caused by the nickel (oxy)hydroxide film growing overtop of the catalyst.

Although the linear portion of **Figure 4.9**e strongly suggested that the nickel (oxy)hydroxide film was the dominate source of mass transfer losses, other time-dependent sources such as

electrolyte flooding into the gas diffusion channels or carbonate precipitation within the electrode pores could potentially contribute to diffusion resistance. Therefore, a similar experiment using a thin-layer electrode and the cell shown in **Figure 4.1**c was performed to further investigate mass transfer losses. The thin-layer electrode (150 μm thick) minimizes the importance of through-thickness oxygen diffusion in comparison to the relatively thick (1000 μm) gas diffusion electrode. Also, the only source of oxygen in this cell is dissolved in the electrolyte (i.e. no gas phase oxygen), meaning that mass transfer losses caused by electrolyte flooding into gas channels is not applicable. Moreover, since the oxygen and water reactants arrive from the same side of the electrode in this case, the ORR should be concentrated on the surface of the thin-layer electrode, which further minimizes the importance of through-thickness oxygen diffusion. Finally, the large volume of circulating electrolyte means that carbonates are unlikely to precipitate inside the electrode pores. Therefore, if the same relationship between limiting current and reciprocal $NiOOH/Ni(OH)_2$ capacity is observed in this experiment, mass transfer losses can be more definitively attributed to oxygen diffusion limitations through the nickel (oxy)hydroxide film.

Figure 4.11a shows the ORR polarization curves for the thin-layer electrode after various cumulative times of oxidation at 2.2 V vs. Zn. Much smaller limiting currents were observed in comparison to the gas diffusion electrode, highlighting the importance of exposure to the oxygen gas phase. It should be noted that Tafel slopes could not be measured from most of these curves since mass transfer losses appeared to dominate even at low overpotentials. Despite the much lower limiting currents, a similar trend of decreasing limiting currents with higher oxidation times was seen, while the inset of **Figure 4.11**b shows a similar relationship between the

$NiOOH/Ni(OH)_2$ capacity and total oxidation time. Most importantly, **Figure 4.11**b displays the same linear correlation between the limiting current and reciprocal of the $NiOOH/Ni(OH)_2$ capacity at high capacity values. The deviation of limiting currents from the linear pattern at low capacity values means that, in this case, the diffusion of dissolved oxygen through the electrolyte was the limiting factor prior to significant growth of the nickel (oxy)hydroxide film. Since other possible sources of mass transfer loss in the gas diffusion electrode can be ruled out in this experiment, the same relationships observed in **Figure 4.9**e and **Figure 4.11**b points to the nickel (oxy)hydroxide film as the most significant source of mass transfer losses in both electrodes. Since the nickel (oxy)hydroxide film grows most rapidly at high potentials (i.e. during OER or charging of a zinc-air battery), the majority of voltage loss in each cycling experiment was likely dictated by total charging time at a given potential and not by other cycling parameters such as the depth of discharge.

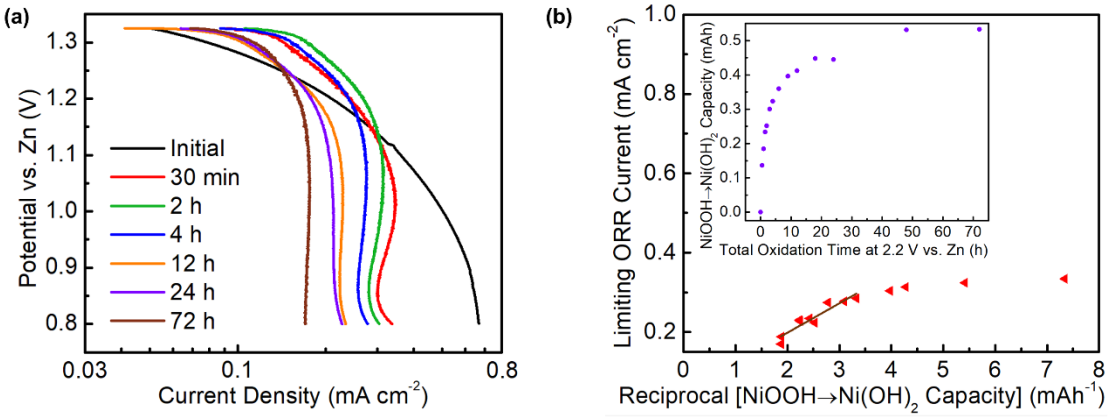

Figure 4.11. Cyclic potentiodynamic polarization (procedure per **Table 4.3**) for nickel-based thin-layer electrode: (a) Full IR-corrected ORR polarization curves, (b) dependence of limiting ORR current on the reciprocal of $NiOOH \rightarrow Ni(OH)_2$ capacity with line of best fit over linear region (inset: dependence of $NiOOH \rightarrow Ni(OH)_2$ capacity on the total oxidation time at 2.2 V).

To summarize, the ORR potential losses observed during cycling of the nickel-based air electrode investigated in this work were caused by a combination of activation and mass transfer losses. Both losses were mainly attributed to the growth of the nickel (oxy)hydroxide film, which is shown schematically for an aggregate of catalyst-coated nickel particles in **Figure 4.12** (actual aggregates could potentially be much more than 8 particles as shown here). Activation losses were associated with a steeper and negatively-shifted Tafel slope, which are caused by increased resistance to oxygen and ionic transport within the aggregate due to film growth inside the pores between the particles. The increased Tafel slope was also attributed to rate limitations of the adsorbed superoxide exchange step in the ORR mechanism, which might also be influenced by nickel (oxy)hydroxide film growth. Mass transfer losses were caused by increased oxygen transport resistance from the gas diffusion channels to the inside of the aggregate due to the nickel (oxy)hydroxide film growth on the outer nickel surfaces. At 10 mA cm^{-2}, mass transfer losses were the dominant source of ORR overpotential. These findings are applicable not only to nickel-supported catalysts, but to any catalyst system involving a metal component where an oxidation film could grow from its surface and block a nearby catalyst site (possibly the metal itself) from access to reactants.

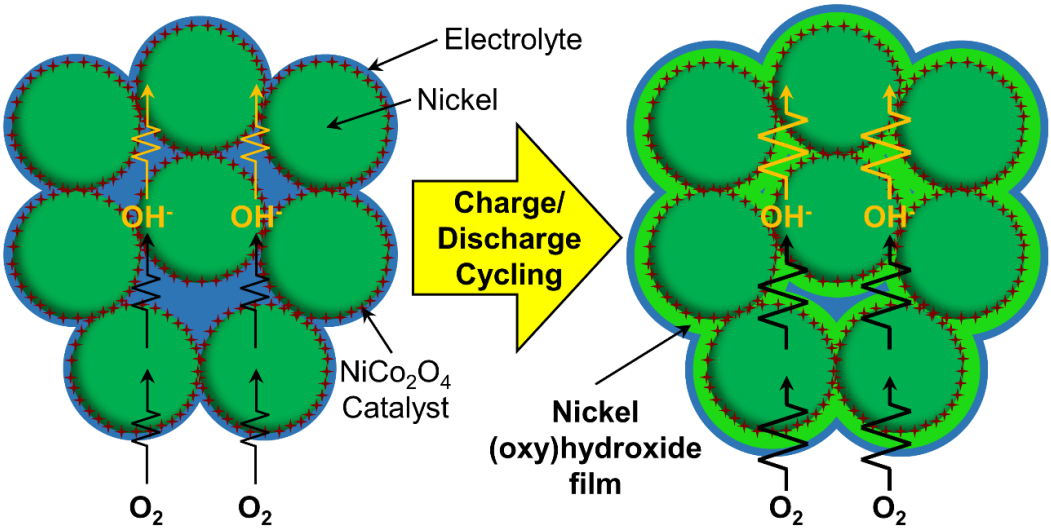

Figure 4.12. Schematic representation of an electrolyte-flooded agglomerate of catalyst-coated nickel particles. The nickel oxy(hydroxide) film growth resulting from prolonged oxidation causes increased oxygen and ionic transport resistance within the aggregate and increased oxygen transport resistance from the outside to the inside of the aggregate.

The results of this investigation have important implications for the design of nickel-based bifunctional air electrodes with improved stability, as well as air electrodes based on other porous networks of metals which may form passivating films. Firstly, the size of the nickel particle aggregates should be reduced; this would shorten the diffusion lengths within the aggregate and mitigate the activation losses from higher effective diffusion coefficients arising from film growth within the aggregate. This could be accomplished by improving the dispersion of nickel and PTFE to minimize nickel particle aggregation during electrode preparation.[311] While the influence of the nickel particle size itself is not clear, it is suspected that the use of larger particles could help minimize aggregation, although larger particles could also result in a significantly lower surface area for catalyst deposition. For mitigating mass transfer losses, the deposited catalyst could be

engineered with a high aspect ratio (e.g. nanowire morphology[225,277]) such that it extends far enough from the nickel support to maintain direct exposure to the electrolyte/gas phase after the passivating film growth begins to slow down. Alternatively, a physical mixture of nickel and catalyst particles (rather than catalyst-coated nickel particles employed in this work) could provide greater separation between the two materials, thus avoiding total (oxy)hydroxide film coverage of the catalyst. However, this could lead to significant ohmic resistance losses if the (oxy)hydroxide film grows between the nickel and catalyst particles. In this case, incorporating a small amount of non-film-forming conductive additives (i.e. carbon or graphite) in the air electrode to maintain electron-conductive interfaces[274] may be beneficial, if the relatively minor carbonate generation from the corrosion of the distributed carbon is tolerable. Finally, it may be possible to completely replace metal supports with metal oxide/hydroxide supports if their conductivity could be sufficiently increased,[312,313] since the growth of oxidation films would not apply in this case. Certainly, the rechargeability of carbon-free or low-carbon air electrodes can be greatly improved by optimizing these structural and compositional factors.

4.4 Conclusions

In this work, the nature and underlying mechanism of nickel-based air electrode performance loss was investigated within rechargeable zinc-air batteries. It was shown that increased ORR overpotential after extended battery cycling was caused by a combination of activation and mass transfer losses, with the latter more significant at a current density of 10 mA cm^{-2}. Electron

microscopy and X-ray photoelectron spectroscopy revealed the growth of a nickel (oxy)hydroxide film overtop of the $NiCo_2O_4$ catalyst, which impeded oxygen diffusion and was the dominant source of mass transfer losses after it grew significantly thick. Nickel (oxy)hydroxide film growth within the pores of the catalyst-coated nickel particle aggregates also likely contributed to higher activation losses evidenced by steeper and negatively-shifted Tafel slopes. The diagnostic methods in this work shed light on various strategies for mitigating performance loss caused by the (oxy)hydroxide film growth. Implementing these strategies could lead to high-energy density rechargeable zinc-air batteries with long cycle life and calendar life.

Chapter 5: Design and Feasibility of Thin Nickel Foam-Based Air Electrodes for Rechargeable Zinc-Air Batteries

5.1 Introduction

In the previous chapter, it was shown that oxidation of nickel metal supports for nickel-based air electrodes is an important factor contributing to the degradation of their ORR activity, particularly when the nickel (oxy)hydroxide film grows overtop of the adhered catalyst. Therefore, to improve the performance of nickel-based air electrodes, electrode designs which can reduce metal oxidation or catalyst structures which can withstand the growth of the nickel (oxy)hydroxide film should be explored. In addition, the mass and thickness of such nickel-based air electrodes should be minimized if they are to succeed in energy-dense rechargeable zinc-air batteries. For instance, the areal mass and thickness of the nickel-based air electrode reported by Price and coworkers[129,256,273] were about 195 mg cm^{-2} and 1.0 mm, while those reported by Armstrong[258] were about 122 mg cm^{-2} and 0.71 mm, respectively. By comparison, carbon felts and papers used for carbon-based air electrodes have areal masses ranging from 4-70 mg cm^{-2} with thicknesses less than 0.5 mm.[314,315]

Unlike the nickel-based air electrode investigated in **Chapter 4**, the nickel metal substrate (sintered nickel plaque with 85% porosity) employed by Armstrong was not loaded with a nickel powder/PTFE slurry before dip-coating. To achieve hydrophobicity, the electrode was either soaked with PTFE emulsion after calcining the dip-coated nickel/cobalt nitrates to nickel/cobalt

oxide, or it was dip-coated in an aqueous mixture of cobalt/nickel nitrate and PTFE particles, which were then calcined/heat-treated together. The latter method was found to result in improved electrochemical performance of the bifunctional air electrode.

It is worthwhile to explore whether the method of co-dip-coating cobalt/nickel nitrates and PTFE particles could also be used to coat a bare nickel foam substrate rather than nickel foam pre-loaded with nickel powder and PTFE. Since nickel foam has an areal mass comparable to carbon papers and felts, such an electrode would be less heavy than the previously investigated nickel-based air electrodes. The nickel foam can also be compressed to a lower thickness prior to dip-coating to produce a thin air electrode that could be practically used in an energy-dense rechargeable zinc-air battery. Also, since a lower ratio of nickel metal to catalyst particles in the electrode can be achieved by eliminating nickel metal powder, less growth and lower interference of the nickel (oxy)hydroxide film with the catalyst is hypothesized. Therefore, this work investigates nickel foam pre-compressed to a thickness of about 0.2 mm and loaded with a mixed cobalt or nickel/cobalt oxide and PTFE coating, herein referred to as thin nickel-foam based air electrodes.

5.2 Experimental Methods

Commercially available nickel foam (110 pores per inch, 35 mg cm^{-2}, 1.6 mm thick), 60 wt.% PTFE emulsion (Sigma Aldrich, product #665800), cobalt (II) nitrate hexahydrate (Alfa Aesar, product #11341A1) and nickel (II) nitrate hexahydrate (Sigma Aldrich, product #72253) were used for fabrication of the air electrode. Morphological characterizations were conducted

with a Zeiss UltraPlus field emission SEM and XRD analyses were completed on a MiniFlex 600 Rigaku instrument.

The thin nickel foam-based air electrode was prepared from which. The nickel foam, which acted as both the catalyst support and current collector, was cut into the desired size and then compressed down to a thickness of approximately 0.2 mm with fixed-width rollers. After rinsing in ethanol and air-drying, the nickel foam was first dip-coated in various precursor mixtures containing suspended PTFE particles and dissolved cobalt nitrate (or nickel/cobalt nitrate). Dip-coating was accomplished by immersing the nickel foam in the precursor solution for 5 minutes, followed by drying in a non-convective oven at 75 °C for approximately 15 minutes, resulting in a mixed coating of PTFE and cobalt nitrate (or nickel/cobalt nitrate) adhered on the nickel foam. The cobalt (or nickel/cobalt nitrates) were converted to the spinel oxide phase (Co_3O_4 or $NiCo_2O_4$) by calcining in an air atmosphere for various temperatures and times. Prior to calcination, some electrodes were also subjected to a pre-heat-treatment step at 125 °C in an air atmosphere, usually for 16 hours. After calcination, the electrodes were soaked in PTFE emulsion with various concentrations, dried at 75 °C for approximately 15 minutes, and then subjected to a heat-treatment in air at the same temperature as the prior calcination, resulting in an outer PTFE-coating. Specific details and parameters of each preparation step are shown in **Table 5.1**. As indicated by the "Dip/pre-heat-treat/calcine sequence" column, some electrodes were subjected to dipping, pre-heating and calcination three times prior to the outer PTFE-coating step (denoted as "3 dip/pre-heat/calcine"), and other electrodes were subjected to dipping and pre-heating three times prior to the calcination step (denoted as "3 dip/pre-heat, 1 calcine").

Table 5.1. Preparation parameters for the investigated thin nickel foam-based air electrodes (*indicates that the pre-heat-treatments after the first two dipping steps were carried out for only 4 hours).

Elec-trode #	**Precursor mixture for electrode dipping**	**Pre-heat-treat temp /time**	**Calcin-ation temp/ time**	**Dip/pre-heat-treat/calcine sequence**	**PTFE concentration for outer PTFE-coating**	**Heat-treatment temp/time after PTFE soaking**
1	2.75 mol l^{-1} $Co(NO_3)_2$ + 80 mg l^{-1} PTFE	-	250 °C / 4 hours	1 dip/calcine	15 wt.%	250 °C / 5 min
2	2.75 mol l^{-1} $Co(NO_3)_2$ + 80 mg l^{-1} PTFE	-	250 °C / 4 hours	1 dip/calcine	15 wt.%	250 °C / 1 h
3	2.75 mol l^{-1} $Co(NO_3)_2$ + 80 mg l^{-1} PTFE	-	300 °C / 2 hours	1 dip/calcine	15 wt.%	300 °C / 5 min
4	2.75 mol l^{-1} $Co(NO_3)_2$ + 80 mg l^{-1} PTFE	-	300 °C / 2 hours	1 dip/calcine	15 wt.%	300 °C / 1 h
5	2.75 mol l^{-1} $Co(NO_3)_2$ + 80 mg l^{-1} PTFE	125 °C / 16 hours	250 °C / 4 hours	1 dip/pre-heat/ calcine	15 wt.%	250 °C / 5 min
6	2.75 mol l^{-1} $Co(NO_3)_2$ + 80 mg l^{-1} PTFE	125 °C / 16 hours	250 °C / 4 hours	1 dip/pre-heat/ calcine	15 wt.%	250 °C / 1 h
7	2.75 mol l^{-1} $Co(NO_3)_2$ + 80 mg l^{-1} PTFE	125 °C / 16 hours	300 °C / 2 hours	1 dip/pre-heat/ calcine	15 wt.%	300 °C / 5 min
8	2.75 mol l^{-1} $Co(NO_3)_2$ + 80 mg l^{-1} PTFE	125 °C / 16 hours	300 °C / 2 hours	1 dip/pre-heat/ calcine	15 wt.%	300 °C / 1 h
9	2.0 mol l^{-1} $Co(NO_3)_2$ + 80 mg l^{-1} PTFE	125 °C / 16 hours	250 °C / 4 hours	1 dip/pre-heat/ calcine	15 wt.%	250 °C / 1 h
10	3.5 mol l^{-1} $Co(NO_3)_2$ + 80 mg l^{-1} PTFE	125 °C / 16 hours	250 °C / 4 hours	1 dip/pre-heat/ calcine	15 wt.%	250 °C / 1 h
11	2.75 mol l^{-1} $Co(NO_3)_2$ + 80 mg l^{-1} PTFE	125 °C / 16 hours	250 °C / 4 hours	3 dip/pre-heat/ calcine	15 wt.%	250 °C / 1 h
12	2.0 mol l^{-1} $Co(NO_3)_2$ + 80 mg l^{-1} PTFE	125 °C / 16 hours	250 °C / 4 hours	3 dip/pre-heat/ calcine	15 wt.%	250 °C / 1 h
13	3.5 mol l^{-1} $Co(NO_3)_2$ + 80 mg l^{-1} PTFE	125 °C / 16 hours	250 °C / 4 hours	3 dip/pre-heat/ calcine	15 wt.%	250 °C / 1 h
14	2.75 mol l^{-1} $Co(NO_3)_2$ + 80 mg l^{-1} PTFE	125 °C / 16 hours	250 °C / 4 hours	3 dip/pre-heat, 1 calcine	15 wt.%	250 °C / 1 h
15	2.0 mol l^{-1} $Co(NO_3)_2$ + 80 mg l^{-1} PTFE	125 °C / 16 hours	250 °C / 4 hours	3 dip/pre-heat, 1 calcine	15 wt.%	250 °C / 1 h
16	3.5 mol l^{-1} $Co(NO_3)_2$ + 80 mg l^{-1} PTFE	125 °C / 16 hours	250 °C / 4 hours	3 dip/pre-heat, 1 calcine	15 wt.%	250 °C / 1 h
17	2.0 mol l^{-1} $Co(NO_3)_2$ + 80 mg l^{-1} PTFE	125 °C / 16 hours	250 °C / 4 hours	3 dip/pre-heat*, 1 calcine	30 wt.%	250 °C / 1 h
18	1.33 mol l^{-1} $Co(NO_3)_2$ + 0.67 mol l^{-1} $Ni(NO_3)_2$ + 80 mg l^{-1} PTFE	125 °C / 16 hours	250 °C / 4 hours	3 dip/pre-heat*, 1 calcine	30 wt.%	250 °C / 1 h

All electrochemical testing was conducted using the same cell design as described in **Section 4.2.2** and shown in **Figure 4.1**b. Galvanostatic cycling was conducted at various current densities using the same "two-step" oxidation and reduction procedure from **Chapter 4** in order to allow the $NiOOH/Ni(OH)_2$ reactions to complete and track their capacities before each subsequent reduction (ORR) or oxidation (OER) step, as shown in **Table 5.2**-**Table 5.4**. To help determine which preparation parameters in **Table 5.1** were important, analysis of variance (ANOVA) and t-tests of the electrode's initial ORR potentials and cycle-lives were completed using "Real Statistics Resource Pack" with Microsoft Excel.

Table 5.2. Galvanostatic cycling procedure at 10 mA cm^{-2} for thin nickel foam-based electrode.

Step	Operation	Duration/End Condition	Dominant Reaction
1	Rest	1 min	
2	Reduction @ 10 mA cm^{-2}	Cut-off @ 1.3 V	Eq. 4.2 (forward)
3	Reduction @ 10 mA cm^{-2}	15 min	Eq. 4.1 (forward)
4	Rest	1 min	
5	Oxidation @ 10 mA cm^{-2}	Cut-off @ 1.95 V	Eq. 4.2 (reverse), Eq. 4.3
6	Oxidation @ 10 mA cm^{-2}	17 min	Eq. 4.3 (reverse)
7	Loop to Step 2		

Table 5.3. Galvanostatic cycling procedure at 20 mA cm^{-2} for thin nickel foam-based electrode. Step 4 was added to additionally monitor the ORR potential at 10 mA cm^{-2} during cycling.

Step	Operation	Duration/End Condition	Dominant Reaction
1	Rest	1 min	
2	Reduction @ 20 mA cm^{-2}	Cut-off @ 1.25 V	Eq. 4.2 (forward)
3	Reduction @ 20 mA cm^{-2}	15 min	Eq. 4.1 (forward)
4	Reduction @ 10 mA cm^{-2}	1 min	Eq. 4.1 (forward)
5	Rest	1 min	
6	Oxidation @ 20 mA cm^{-2}	Cut-off @ 2.0 V	Eq. 4.2 (reverse), Eq. 4.3
7	Oxidation @ 20 mA cm^{-2}	19 min	Eq. 4.3 (reverse)
8	Loop to Step 2		

Table 5.4. Galvanostatic cycling procedure at 50 mA cm^{-2} for thin nickel foam-based electrode. Steps 4 and 5 were added to additionally monitor the ORR potentials at 10 mA cm^{-2} and 20 mA cm^{-2} during cycling.

Step	Operation	Duration/End Condition	Dominant Reaction
1	Rest	1 min	
2	Reduction @ 50 mA cm^{-2}	Cut-off @ 1.20 V	Eq. 4.2 (forward)
3	Reduction @ 50 mA cm^{-2}	15 min	Eq. 4.1 (forward)
4	Reduction @ 20 mA cm^{-2}	1 min	Eq. 4.1 (forward)
5	Reduction @ 10 mA cm^{-2}	1 min	Eq. 4.1 (forward)
6	Rest	1 min	
7	Oxidation @ 50 mA cm^{-2}	Cut-off @ 2.05 V	Eq. 4.2 (reverse), Eq. 4.3
8	Oxidation @ 50 mA cm^{-2}	19 min	Eq. 4.3 (reverse)
9	Loop to Step 2		

5.3 Results and Discussion

5.3.1 Physical Characterization

The morphologies of the thin nickel foam-based air electrode after calcination and after applying the outer PTFE-coating are displayed in **Figure 5.1** As will be shown later, this specific electrode design (Electrode #17 in **Table 5.1**) resulted in the highest cycle-life and is therefore used as the basis for the following physical and crystallographic analyses. The as-calcined electrode displays a rough texture across the surface of the nickel foam struts (**Figure 5.1**a), and upon examination at higher magnifications (**Figure 5.1**c,e) is revealed to be uniformly coated by sisal-like structures. After applying the outer-PTFE coating, the nickel foam struts have a more smooth appearance (**Figure 5.1**b) due to the mostly-continuous layer of PTFE observed at higher magnifications (**Figure 5.1**d,f). However, the tips of the sisal-like structures can still be observed protruding through the outer PTFE layer across various locations of the electrode in **Figure 5.1**d,f. The texture of the PTFE layer in **Figure 5.1**f is consistent with that of previously reported annealed PTFE film samples.[316] It should also be noted that, as expected, the electrode surface becomes highly water-repellant after applying the outer PTFE-coating due to the hydrophobic property of PTFE.

Figure 5.2 displays a sequence of even higher magnification SEM images exhibiting the morphological evolution of the constituents on the nickel foam surface after various stages of preparation, and **Figure 5.3** displays corresponding diffraction patterns. After dipping the thin nickel foam in the cobalt nitrate/PTFE precursor mixture and drying at 75 °C, sharp crystals are

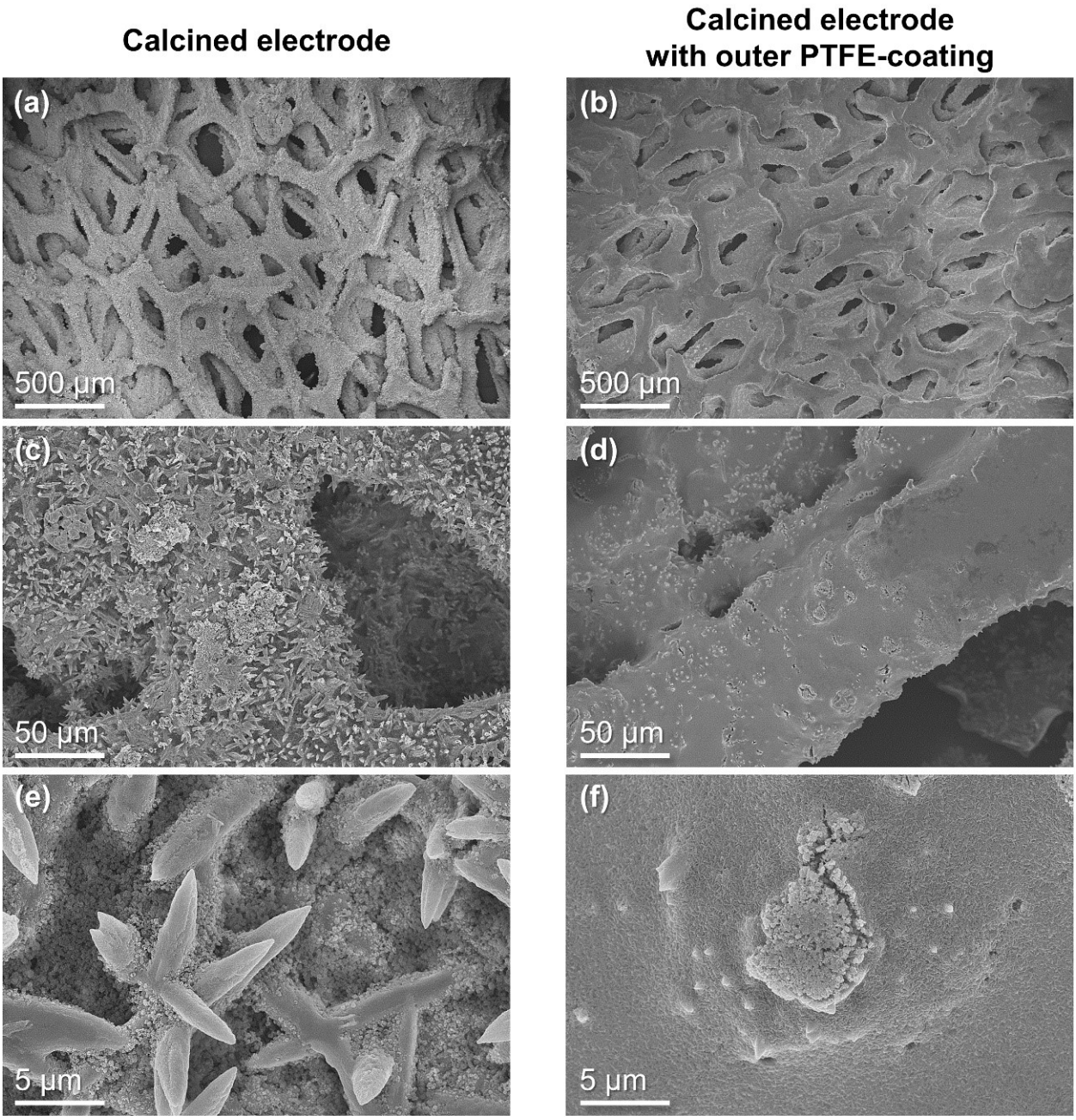

Figure 5.1. SEM images of thin nickel-foam based air electrode (Electrode #17 in **Table 5.1**): (a,c,e) calcined electrode and (b,d,f) calcined electrode with outer PTFE-coating. (a,b) 100 X magnification; (c,d) 1000X magnification; (d,e) 10,000X magnification.

observed on the foam surface (**Figure 5.2**a). These crystals were assumed to have resulted from the precipitation of dissolved cobalt nitrate upon evaporation of water during drying. The associated diffraction pattern after drying at 75 °C (**Figure 5.3**a) displays a large number of peaks ranging from approximately 7 to 43 degrees. Hydrated cobalt nitrates often similarly display a high density of diffraction peaks[317,318]; however, the diffraction pattern in **Figure 5.3**a could not be indexed to any hydrated cobalt nitrate pattern references, perhaps because the intermixed PTFE particles could change the facets of the typical hydrated cobalt nitrate crystal structure.

Figure 5.2b shows the $Co(NO_3)_2$/PTFE-dipped electrode after the 16-hour pre-heat-treatment at 125 °C. A much smoother surface is observed after this pre-heat-treatment, likely due to the melting and partial dehydration/decomposition[317,319] of the hydrated cobalt nitrate resulting in a more compact coating. The associated diffraction pattern in **Figure 5.3**b shows a reduced number of crystal facets likely due to the partial dehydration/decomposition of the cobalt nitrate, but once again it could not be indexed to any cobalt nitrate pattern references. The compacted coating is suspected to be beneficial to the electrode's stability by providing better protection of the underlying nickel metal struts from oxidation by the electrolyte. **Figure 5.2**c shows a higher-magnification image of the same sample, highlighting the presence of small particles likely corresponding to PTFE due to their similar size and morphology to previously reported images of PTFE particles.[316,320] This is also consistent with the existence of a diffraction peak at 17 degrees in **Figure 5.3**b corresponding to PTFE.

The SEM images in **Figure 5.2**d,e show the aforementioned sisal-like structure at higher magnification that is formed after calcining the electrode at 250 °C, while the diffraction pattern

in **Figure 5.3**c shows the added presence of Co_3O_4-indexed peaks, confirming that the cobalt nitrate coating is converted to cobalt oxide. The higher-magnification image in **Figure 5.2**d,e also highlights that the PTFE particles remain in place after calcination and are well-dispersed around the branches of the sisal-like cobalt oxide. This could be beneficial to the mechanical stability of the cobalt oxide branches during electrochemical cycling, especially during high-current OER where oxygen bubbles are rapidly evolved from the oxide surface, due to the binding property of PTFE. The partial coverage of the cobalt oxide branches by PTFE particles could also provide ample three-phase interfaces between the oxide, electrolyte and oxygen during ORR due to the hydrophobic function of PTFE. It is also interesting to note that previous reporters of sisal-like cobalt oxides[321,322] employed more complicated synthesis routes than the simple dip-coating method employed here.

Figure 5.2f finally shows the thin nickel foam surface after applying the outer-PTFE layer, and the associated diffraction pattern in **Figure 5.3**e predictably shows a more intense peak corresponding to PTFE. Unlike **Figure 5.1**f, this region of the PTFE-coating contains a relatively large hole around a cobalt oxide branch. While the purpose of the outer PTFE-coating is to prevent over-flooding of the electrolyte throughout the entire pore volume of the nickel foam, it is speculated that these holes could allow a thin film of electrolyte to travel underneath the outer PTFE layer, providing necessary contact with the cobalt oxide branches. However, the electrolyte could also possibly contact the tips of the branches which protrude through the outer PTFE layer.

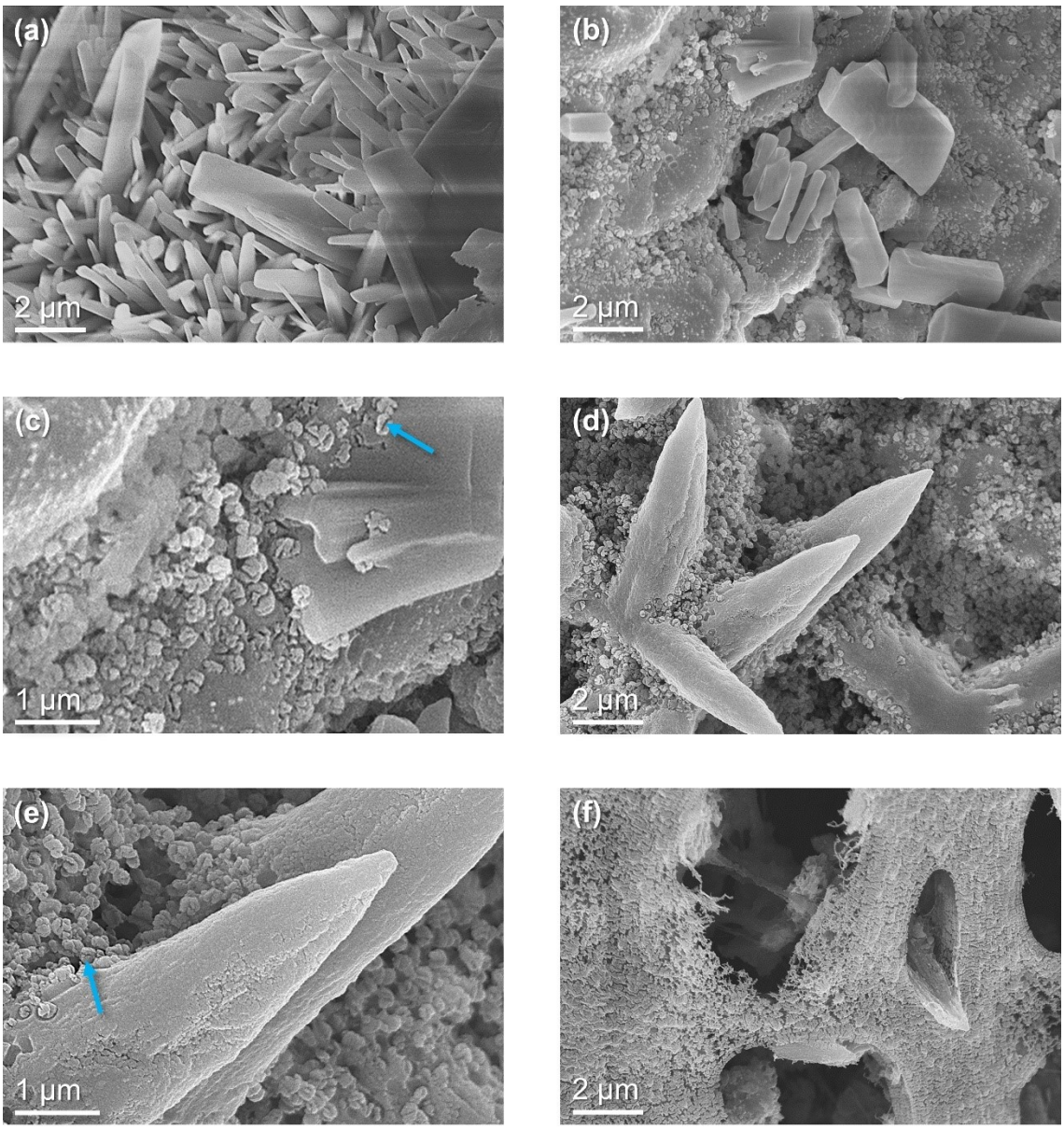

Figure 5.2. SEM images of the thin nickel foam-based air electrode after various stages of preparation: (a) after dipping in $Co(NO_3)_2$/PTFE mixture (2.0 mol l^{-1} $Co(NO_3)_2$ + 80 mg l^{-1} PTFE) and drying at 75 °C for 15 minutes; (b,c) after subjecting $Co(NO_3)_2$/PTFE-dipped electrode to pre-heat-treatment at 125 °C for 16 hours; (d,e) after subjecting $Co(NO_3)_2$/PTFE-dipped and pre-heat-treated electrode (3 dip/pre-heat-treatment cycles) to calcination at 250 °C for 4 hours; (f) after soaking calcined electrode from (d,e) in 30 wt.% PTFE emulsion, drying at 75 °C for 15 minutes, and heat-treating at 250 °C for 1 hour. (a,b,d,f) 20,000X magnification; (c,e) 50,000X magnification, with blue arrows highlighting the existence of PTFE particles.

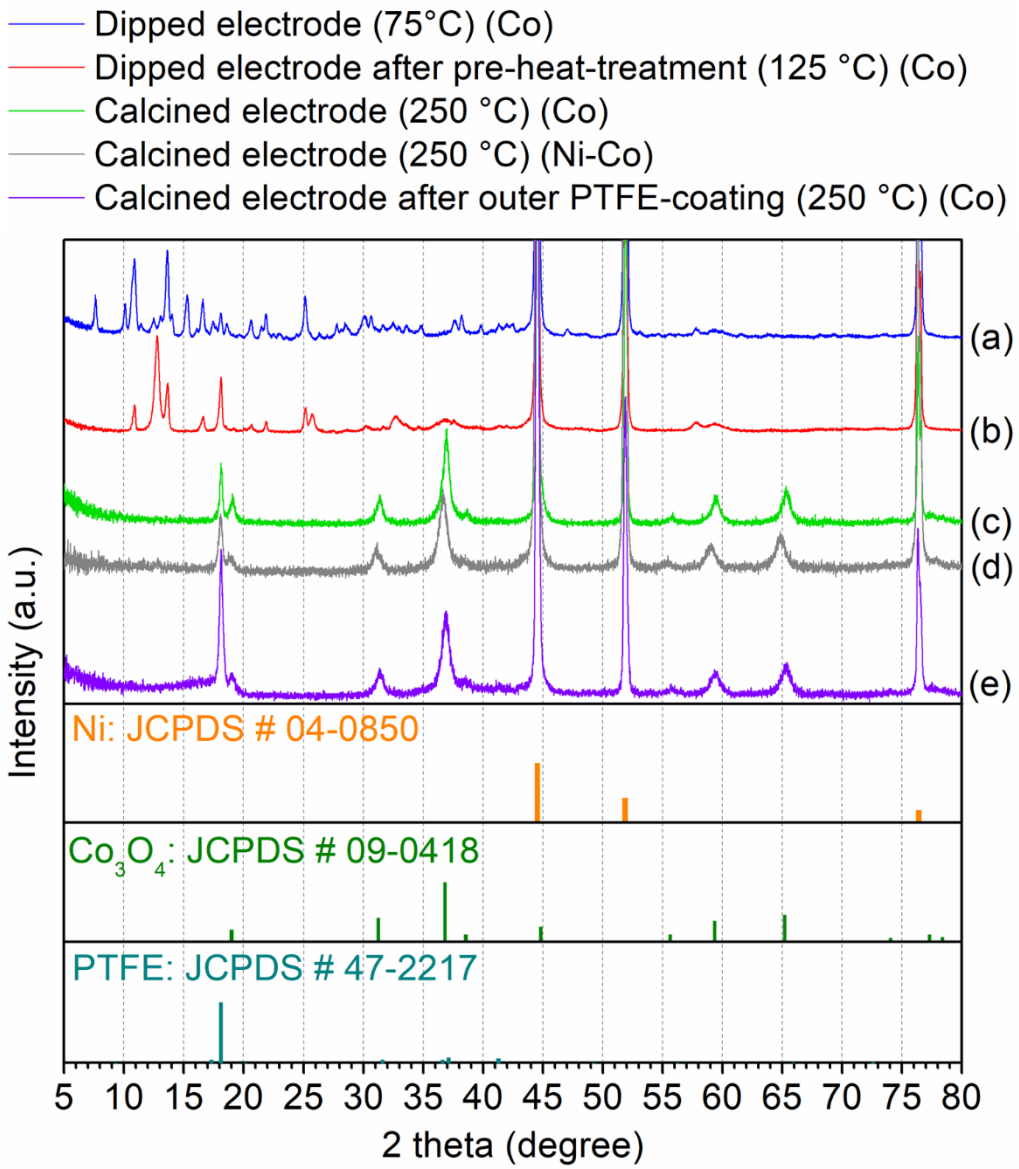

Figure 5.3. XRD spectra of the nickel foam-based air electrode after various stages of preparation: (a) after dipping in $Co(NO_3)_2$/PTFE mixture (2.0 mol l^{-1} $Co(NO_3)_2$ + 80 mg l^{-1} PTFE) and drying at 75 °C for 15 minutes; (b) after subjecting $Co(NO_3)_2$/PTFE-dipped electrode to pre-heat-treatment at 125 °C for 16 hours; (c) after subjecting $Co(NO_3)_2$/PTFE-dipped and pre-heat-treated electrode (3 dip/pre-heat-treatment cycles) to calcination at 250 °C for 4 hours; (d) after subjecting $[Ni_{1/3}Co_{2/3}](NO_3)_2$/PTFE-dipped and pre-heat-treated electrode (3 dip/pre-heat-treat cycles, equivalent total nitrate and PTFE concentration as (a-c)) to calcination at 250 °C for 4 hours; (e) after soaking calcined electrode from (c) in 30 wt.% PTFE emulsion, drying at 75 °C for 15 minutes, and heat-treating at 250 °C for 1 hour.

Figure 5.4 shows an equivalently prepared as-calcined electrode which was dipped in a mixture of nickel and cobalt nitrate (1.33 mol l^{-1} $Co(NO_3)_2$ + 0.67 mol l^{-1} $Ni(NO_3)_2$) with PTFE instead of only cobalt nitrate and PTFE. While the left-shifted spinel diffraction peaks in **Figure 5.3**d indicate the formation of $NiCo_2O_4$, the sisal-like oxide morphology was not observed on this electrode, which instead displayed a more flat and cracked structure. Cracks could perhaps form due to stress buildup if the cobalt and nickel nitrate ions precipitate at different rates during drying, or if cobalt and nickel nitrates decompose at different rates during the pre-heat-treatment or calcination steps. A previous report[323] also showed considerably different morphologies between calcined Co_3O_4 and $NiCo_2O_4$ nanostructures.

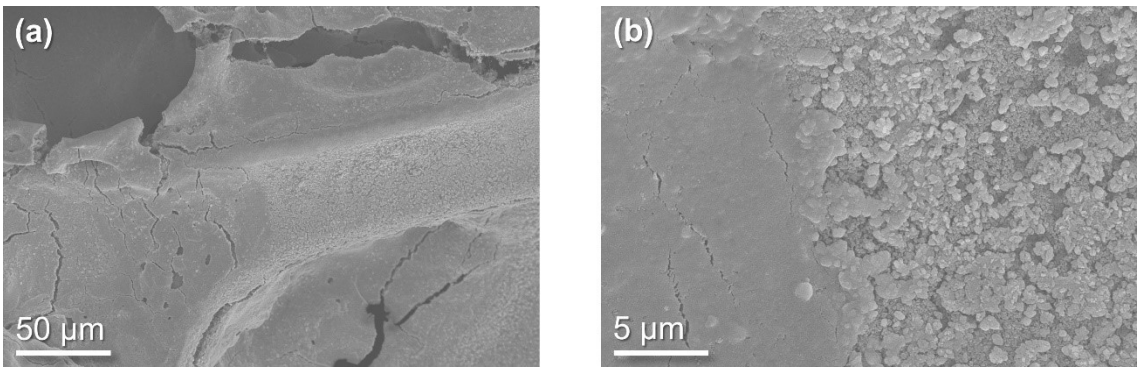

Figure 5.4. SEM images of $[Ni_{1/3}Co_{2/3}](NO_3)_2$/PTFE-dipped and pre-heat-treated electrode (3 dip/pre-heat-treat cycles, 1.33 mol l^{-1} $Co(NO_3)_2$ + 0.67 mol l^{-1} $Ni(NO_3)_2$ + 80 mg l^{-1} PTFE) after calcination at 250 °C for 4 hours: (a) 1000X magnification; (b) 10,000X magnification.

Table 5.5 shows some basic physical properties of the developed thin nickel foam-based air electrode. Typical values for the nickel-based air electrode investigated in **Chapter 4** (hereafter referred to as the thick nickel-based air electrode) are also shown for comparison. The

approximately four-times thinner and over four-times lighter electrode developed here is much better suited to an energy-dense zinc-air battery configuration, since there would be far less "wasted" mass and thickness on a component which does not itself provide electrochemical capacity. The Co_3O_4 or $NiCo_2O_4$ loading of the thin nickel foam-based electrode, despite undergoing three dip-coat cycles rather than only one for the thick nickel-based air electrode, is slightly lower than the $NiCo_2O_4$ loading on the thick nickel-based air electrode. This is likely due to the higher surface area of the pre-dipped thick nickel-based air electrode, which unlike the present electrode, was loaded with nickel powder. The thin nickel foam-based electrode also has over six times less PTFE than the thick nickel-based electrode, which (along with the complete absence of nickel powder) should substantially lower the material costs for the former. The absence of a nickel powder slurry also means that the manufacturing cost of large-scale fabrication of the thin nickel foam-based air electrode should be lower due, since slurry mixing and slurry pasting equipment is not needed.

Table 5.5. Basic physical properties of the thin nickel foam-based air electrode (Electrode #17 in **Table 5.1**) compared to the thick nickel-based air electrode from **Chapter 4**. Loadings were calculated by mass change measurements.

	Thin nickel foam-based air electrode (Co_3O_4-loaded)				**Thin nickel foam-based air electrode** ($NiCo_2O_4$-loaded)	**Thick nickel-based air electrode** ($NiCo_2O_4$-loaded)
	Sample 1	Sample 2	Sample 3	**Aver-age**		
Approximate Thickness (mm)	0.25	0.25	0.25	0.25	0.25	1.0
Areal Mass (mg cm^{-2})	47.38	48.95	51.33	49.22	46.00	237.45
Co_3O_4 or $NiCo_2O_4$ loading (mg cm^{-2})	8.02	8.60	8.85	8.49	7.12	10.47
Inner PTFE (intermixed with Co_3O_4 or $NiCo_2O_4$) loading (mg cm^{-2})	4.00	4.29	4.42	4.24	3.56	-
Outer PTFE loading (mg cm^{-2})	3.82	4.14	5.41	4.46	4.14	-
Total PTFE (mg cm^{-2})	7.82	8.43	9.83	8.70	7.70	57.20

5.3.2 Electrochemical Cycling Evaluation

The galvanostatic cycling performance of the $NiCo_2O_4$-loaded thin nickel foam electrode (Electrode #18 in **Table 5.1**) is evaluated here first at 10 mA cm^{-2} in order to provide a direct comparison to the thick nickel-based air electrode from **Chapter 4:**. The galvanostatic cycling potentials over time are shown in **Figure 5.5**a. The initial ORR potential at 10 mA cm^{-2} for the thin nickel foam electrode was over 1.25 V vs. Zn, which was slightly higher than the thick nickel electrode (1.24 V vs. Zn, **Figure 4.4**a). The OER potential at 10 mA cm^{-2} was also slightly lower for the thin nickel foam electrode, remaining below 2.05 V vs. Zn during the entire cycling experiment. Moreover, no within-cycle fluctuations of the OER potential (as was shown for the thick nickel-based electrode in **Figure 4.4**a,b) were observed for the thin nickel foam electrode, which could be explained by the electrode's larger porosity which avoids trapping evolved oxygen.

In **Figure 5.5**b it is seen that the $NiOOH/Ni(OH)_2$ capacity of the thin nickel foam air electrode grows larger as the cycle number increases, showing that the underlying nickel metal foam is progressively oxidized to nickel hydroxide which subsequently oxidizes and reduces between NiOOH and $Ni(OH)_2$. However, the capacity growth on the thick nickel-based air electrode was considerably faster than that of the thin nickel foam-based air electrode; for instance, after 80 cycles, the $NiOOH/Ni(OH)_2$ capacity of the former grew to approximately 4 mAh (**Figure 4.4**c), compared to only 1.7 mAh for the latter (**Figure 5.5**b). This likely helps to explain why the thin nickel foam electrode withstood over three times more charge-discharge cycles than the thick nickel-based electrode, lasting 187 charge-discharge cycles with an ORR voltage higher than 1.0 V vs. Zn at 10 mA cm^{-2} (**Figure 5.5**c).

If the same failure mechanism (**Figure 4.12)** applies to both types of electrodes, the thin nickel foam electrode likely can withstand more charge/discharge cycles because only the nickel metal foam struts grow a nickel (oxy)hydroxide film, as compared to both the nickel metal powder particles and nickel metal struts in the thick nickel-based electrode. Also, while the total catalyst loading is relatively similar on both electrodes (**Table 5.5**), the catalyst is dispersed across a much lower surface area on the thin nickel foam electrode (i.e. only across the nickel struts, whereas the catalyst is dispersed across both the nickel metal struts and nickel powder particles for the thick nickel-based electrode). This means that the catalyst layer thickness on the thin nickel foam-based electrode is likely significantly thicker than that on the thick nickel-based electrode, meaning that the underlying nickel metal is better protected from oxidation and also that a growing (oxy)hydroxide layer will require a longer time to completely grow overtop of the catalyst particles.

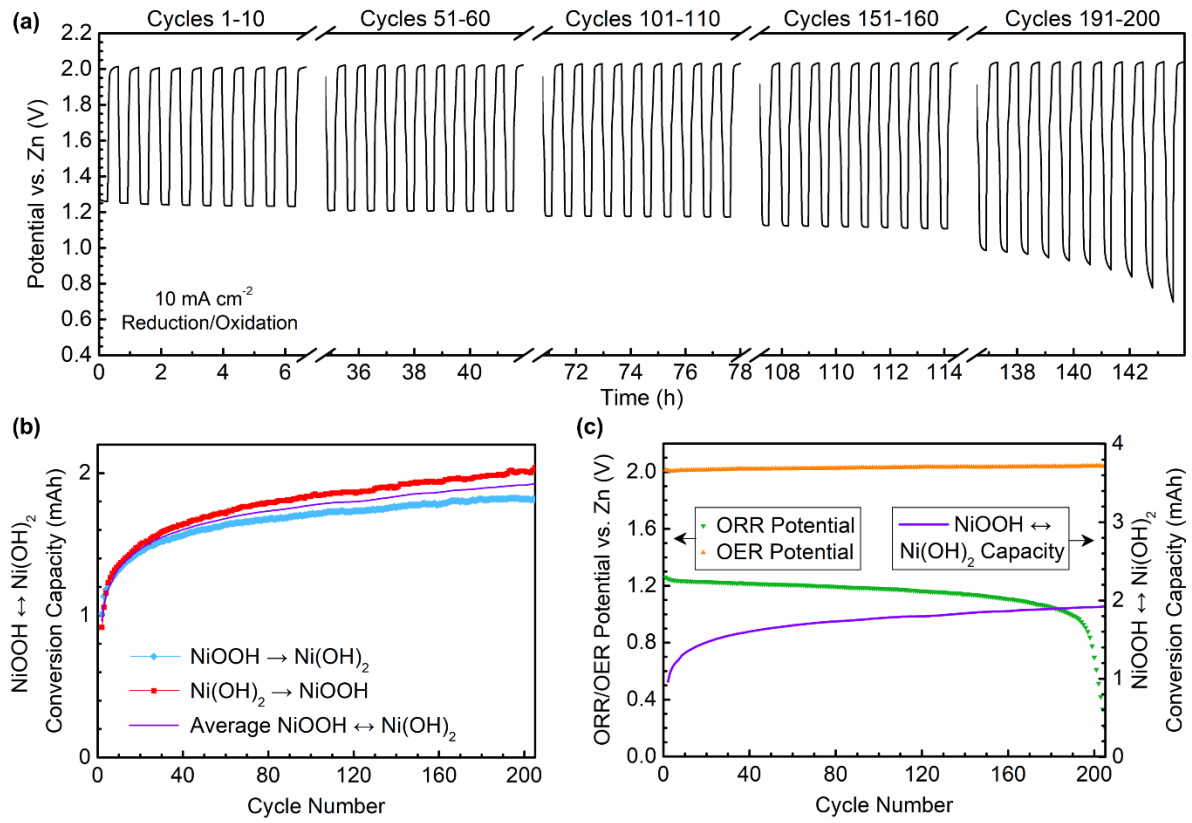

Figure 5.5. Galvanostatic cycling at 10 mA cm^{-2} (procedure per **Table 5.2**) for thin-nickel foam-based air electrode with $NiCo_2O_4$ catalyst (Electrode #18 in **Table 5.1**): (a) Galvanostatic cycling potentials; (b) NiOOH→$Ni(OH)_2$ and $Ni(OH)_2$→NiOOH conversion capacities with 10-point adjacent-average smoothed lines; (c) ORR/ OER potentials and average NiOOH/$Ni(OH)_2$ capacity as a function of cycle number.

Next, the galvanostatic cycling performance of the equivalently prepared Co_3O_4-loaded thin nickel foam electrode (Electrode #17 in **Table 5.1**) at 10 mA cm^{-2} is evaluated to observe the outcome when using Co_3O_4 as the dip-coated catalyst rather than $NiCo_2O_4$. **Figure 5.6**a shows the galvanostatic cycling potentials, where it is apparent that although the initial ORR potential is slightly lower (1.24 V vs. Zn) in comparison to the $NiCo_2O_4$-loaded electrode, the cycle-stability of the ORR potential is dramatically improved for the Co_3O_4-loaded electrode. This result can be

correlated with the much slower $NiOOH/Ni(OH)_2$ capacity growth observed in **Figure 5.6**b; after 200 cycles, the measured $NiOOH/Ni(OH)_2$ capacity of the Co_3O_4-loaded electrode was only 0.84 mAh, over two times lower than that for the $NiCo_2O_4$-loaded electrode (1.9 mAh after 200 cycles). Perhaps due to this factor, the Co_3O_4-loaded electrode displays a remarkably improved cycle-life, providing over 1100 charge-discharge cycles with an ORR potential greater than 1.0 V vs. Zn at 10 mA cm^{-2} (**Figure 5.6**c).

The slower capacity growth of the Co_3O_4-loaded electrode, indicating slower oxidation of the nickel metal foam, could be explained by the more uniform surface coverage of the deposited oxide/PTFE layer (**Figure 5.1**c,e) compared to that for the $NiCo_2O_4$-loaded electrode (**Figure 5.4**a,b). The specific morphology of the Co_3O_4-loaded electrode, where the branches of the sisal-like Co_3O_4 particles protrude away from the nickel foam substrate and the PTFE particles are congregated closer to the substrate at the base of the branches, may also help to explain its reduced nickel metal oxidation and enhanced cycle-life. It is suspected that this configuration reduces the amount of direct electrolyte contact with the nickel metal substrate due to the hydrophobic nature of the PTFE particles, and the electrolyte would instead preferentially contact the more hydrophilic protruding tips of the Co_3O_4 branches that are free from PTFE particle coverage.

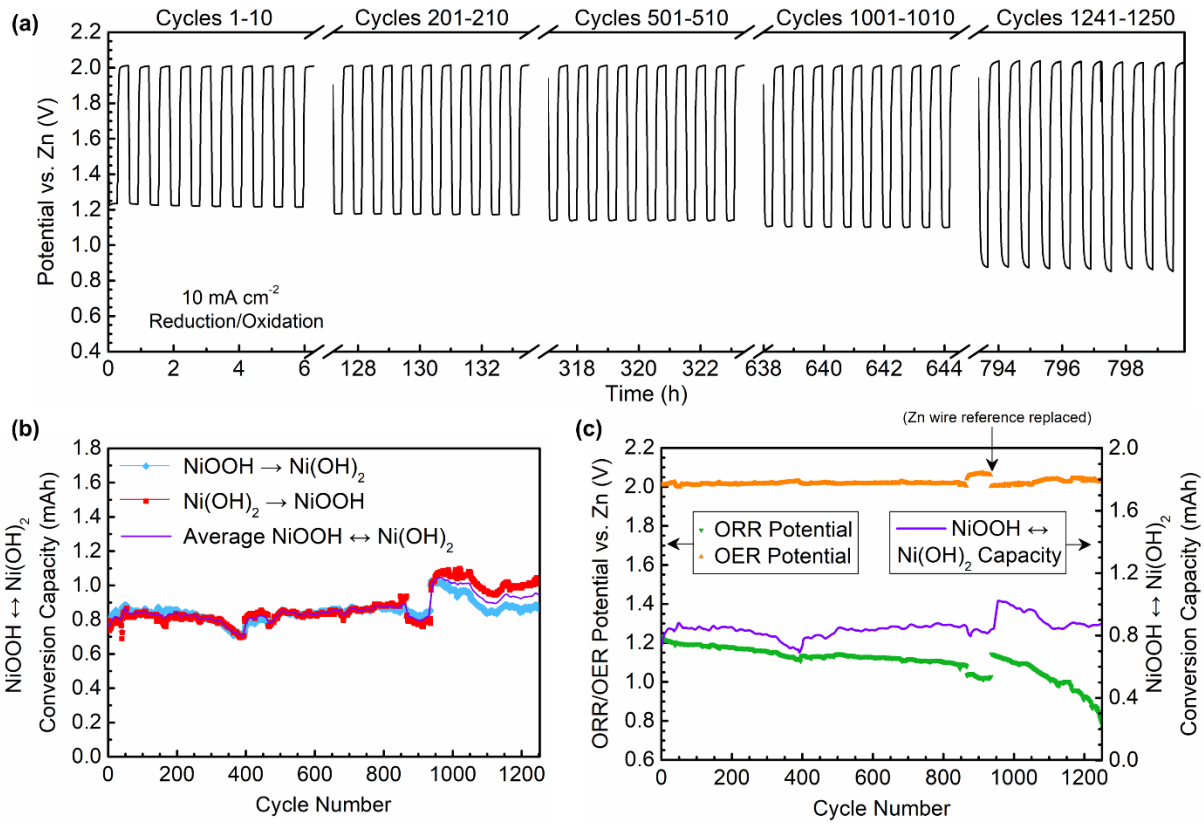

Figure 5.6. Galvanostatic cycling at 10 mA cm^{-2} (procedure per **Table 5.2**) for thin-nickel foam-based air electrode with Co_3O_4 catalyst (Electrode #17 in **Table 5.1**): (a) Galvanostatic cycling potentials; (b) NiOOH→$Ni(OH)_2$ and $Ni(OH)_2$→NiOOH conversion capacities with 10-point adjacent-average smoothed lines; (c) ORR/ OER potentials and average NiOOH/$Ni(OH)_2$ capacity as a function of cycle number.

Due to the long cycle-life of the Co_3O_4-loaded thin foam electrode at 10 mA cm^{-2} (over 650 hours of operation with an ORR potential above 1.0 V vs. Zn), the electrode cycle-life was also evaluated with higher-current galvanostatic cycling tests. The galvanostatic cycling potentials for cycle-tests using 20 mA cm^{-2} and 50 mA cm^{-2} alternating oxidation and reduction currents are shown in **Figure 5.7**a and **Figure 5.7**b, respectively. At 20 mA cm^{-2}, the thin foam electrode is still capable of providing over 500 cycles with ORR potentials above 1.0 V vs. Zn during over 350

hours of operation. At 50 mA cm^{-2}, the electrode can provide over 100 cycles with ORR potentials above 1.0 V vs Zn. A recent modeling study[257] determined that a theoretical rechargeable zinc-air battery capable of providing 150 charge-discharge cycles with discharge currents up to 40 mA cm^{-2} would be feasible in a dual-battery electric vehicle, with the zinc-air battery pack acting as a range extender to supplement a small lithium-ion battery pack. Therefore, the result in **Figure 5.7**b for cycling at a constant current of 50 mA cm^{-2} seems to indicate that the thin nickel foam-based electrode developed here could be a promising air electrode candidate in an automotive zinc-air battery application. Also, as discussed in earlier chapters, the absence of any carbon-phase constituent in nickel-based air electrodes would eliminate the issue of carbon corrosion in conventional carbon-based air electrodes,[130] which would occur in the latter electrode type even when the battery is not operating. This is an important consideration especially for a zinc-air battery acting as an occasionally used range-extender, since such a battery would be inactive for long periods of time.

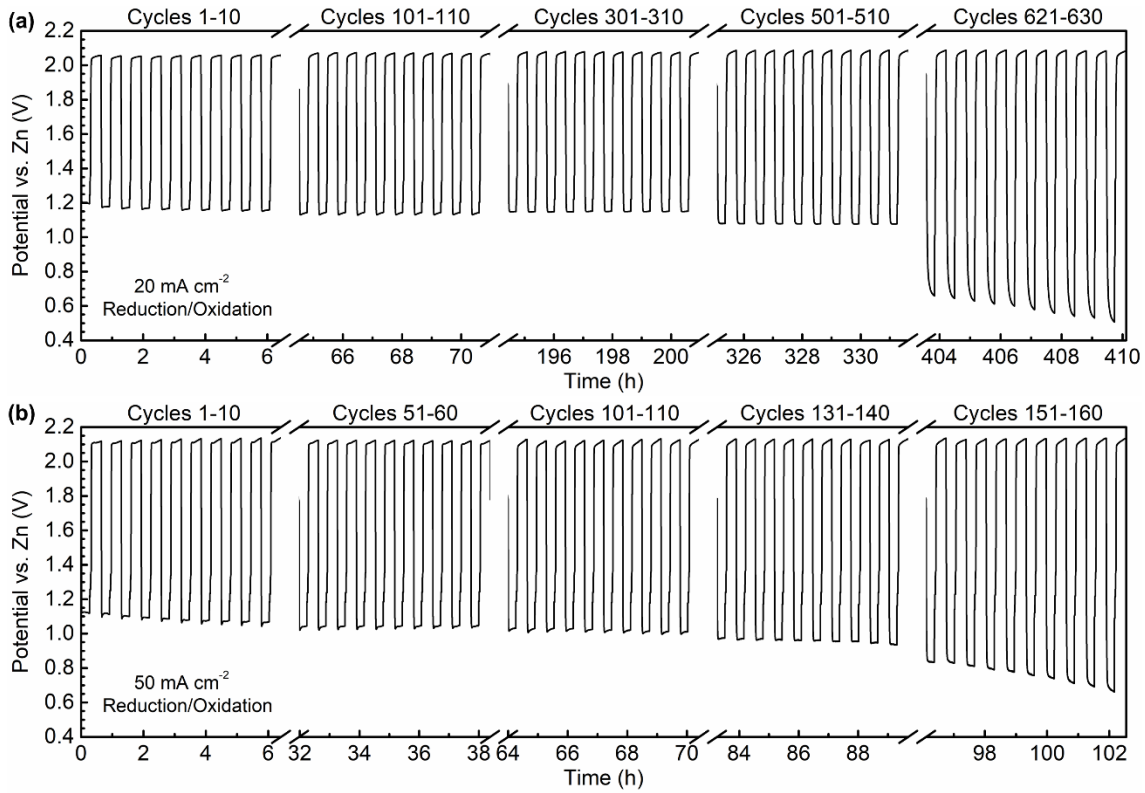

Figure 5.7. Galvanostatic cycling potentials for thin-nickel foam-based air electrode with Co_3O_4 catalyst (Electrode #17 in **Table 5.1**) at (a) 20 mA cm^{-2} (procedure per **Table 5.3**) and (b) 50 mA cm^{-2} (procedure per **Table 5.4**).

The next section briefly discusses and compares the performances of Electrode #'s 1 through 17 in **Table 5.1**, showing how the preferred combination of preparation parameters to produce the above Co_3O_4-loaded thin nickel foam-based air electrode was arrived at. All evaluations were conducted at 20 mA cm^{-2} using the procedure outlined in **Table 5.3**, and the initial ORR potentials and cycle-lives of the electrodes were both evaluated. The initial ORR potential was measured at the end of the first reduction cycle (end of step 3 in **Table 5.3**) following the first oxidation cycle, and the cycle-life was defined as the number of completed oxidation-reduction cycles that the air

electrode displayed an ORR potential of greater than 1.0 V vs. Zn by the end of step 3 in **Table 5.3**.

First, **Figure 5.8** summarizes the initial ORR potentials and cycle-lives of electrodes (i) with and without the 16-hour, 125 °C pre-heat-treatment step, (ii) calcined at 250 °C for 4 hours or 300 °C for 2 hours, and (iii) heat-treated for 5 minutes or 1 hour after PTFE soaking for the outer PTFE-coating. In all cases, the initial ORR potential was higher for electrodes calcined at 250 °C for 4 hours, and electrodes pre-heat-treated at 125°C for 16 hours prior to calcination. The cycle-life was also higher for all electrodes subjected to the pre-heat-treatment step, but the effect of the calcination condition on cycle-life was inconclusive. The effect of heat-treatment time after PTFE soaking on the initial ORR potential was inconclusive, but the 1-hour heat-treatment time appeared to be slightly beneficial to the cycle-life.

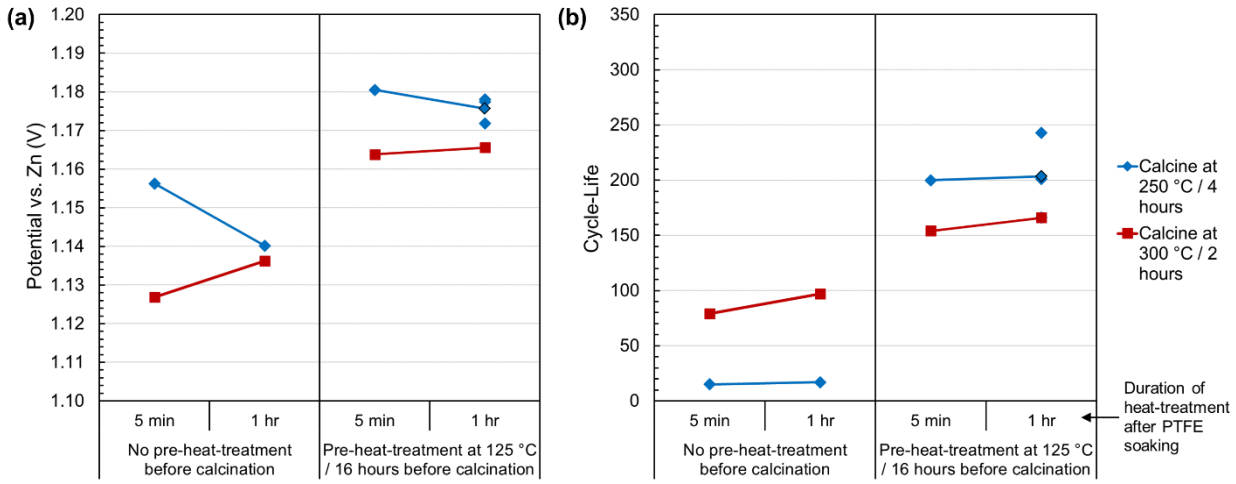

Figure 5.8. (a) Initial ORR potential vs. Zn and (b) cycle-life of thin nickel foam-based air electrodes at 20 mA cm^{-2} with the following three preparation factors: pre-heat/no pre-heat, calcination temperature/time, duration of heat-treatment after PTFE soaking. The initial ORR potential was measured at the end of the first reduction cycle (end of step 3 in **Table 5.3**) following the first oxidation cycle. Cycle life is defined as the number of oxidation-reduction cycles at 20 mA cm^{-2} (procedure per **Table 5.3**) with that the air electrode maintained an ORR potential of greater than 1.0 V vs. Zn by the end of each 20 mA cm^{-2} reduction cycle (end of step 5 in). In the cases where repeat samples were tested, the black-outlined coordinate indicates the average potential or cycle-life of the three samples. The results in this figure are of Electrode #'s 1-8 in **Table 5.1**.

The means and variances of the initial ORR potential and cycle-life for the above three factors are summarized in **Table 5.6** and **Table 5.8** respectively, and associated ANOVA results are shown in **Table 5.7** and **Table 5.9** respectively. The ANOVA results confirmed that pre-heat-treatment step significantly affected both the initial ORR potential and cycle-life, and the choice of calcination condition also significantly affected the initial ORR potential. Therefore the 125 °C pre-heat-treatment step and 250 °C/4-hour calcination condition were selected as preferred preparation parameters. The difference in means of cycle-life between 5-minue and 1-hour heat-

treatment times after PTFE soaking was not statistically significant, but nevertheless the 1-hour heat-treatment time after PTFE soaking was selected for producing the next set of electrodes.

Table 5.6. Means and variances of initial ORR potential (vs. Zn at 20 mA cm^{-2}) for thin nickel foam-based electrodes grouped by the following three preparation factors: pre-heat/no pre-heat, calcination temperature/time, duration of heat-treatment after PTFE soaking. Initial ORR potential and cycle-life are defined in the **Figure 5.8** caption.

Pre-heat-treatment before calcination	Calcination temperature / time	Duration of heat-treatment after PTFE soaking	Count	Mean	Variance
No			4	1.1399 V	0.000150580
Yes (125 °C / 16 hr)			4	1.1714 V	0.000064329
	250 °C / 4 hr		4	1.1632 V	0.000344328
	300 °C / 2 hr		4	1.1481 V	0.000381262
		5 minutes	4	1.1569 V	0.000501643
		1 hour	4	1.1544 V	0.000371142

Table 5.7. Three-factor ANOVA of initial ORR potential statistics in **Table 5.6**.

	SS	df	MS	F	p-value	Significant? (α=0.05)
Pre-heat-treatment before calcination	0.001985550	1	0.001985550	44.29628	0.00265	Yes
Calcination temperature / time	0.000453507	1	0.000453507	10.11743	0.03351	Yes
Duration of heat-treatment after PTFE soaking	0.000011923	1	0.000011923	0.26600	0.63322	No
Error (Within)	0.000179297	4	0.000044824			
Total	0.002630278	7	0.000375754			

Table 5.8. Means and variances of cycle-life (at 20 mA cm^{-2}) for thin nickel foam-based electrodes grouped by the following three preparation factors: pre-heat/no pre-heat, calcination temperature/time, duration of heat-treatment after PTFE soaking. Initial ORR potential and cycle-life are defined in the **Figure 5.8** caption.

Pre-heat-treatment before calcination	Calcination temperature / time	Duration of heat-treatment after PTFE soaking	Count	Mean	Variance
No			4	52	1783
Yes (125 °C / 16 hr)			4	181	605
	250 °C / 4 hr		4	109	11493
	300 °C / 2 hr		4	124	1806
		5 minutes	4	112	6669
		1 hour	4	121	6732

Table 5.9. Three-factor ANOVA of cycle-life statistics in **Table 5.8**.

	SS	df	MS	F	p-value	Significant? (α=0.05)
Pre-heat-treatment before calcination	33196	1	33196	20.28616534	0.010789324	Yes
Calcination temperature / time	460	1	460	0.281140723	0.624023114	No
Duration of heat-treatment after PTFE soaking	156	1	156	0.095365812	0.772879111	No
Error (Within)	6546	4	1636			
Total	40358	7	5765			

Figure 5.9 summarizes the initial ORR potentials and cycle-lives of electrodes with (i) three different $Co(NO_3)_2$ concentrations in the precursor dipping mixture (2.0, 2.75, 3.5 mol l^{-1}) and (ii) dip/pre-heat-treat/calcine sequence (1 dip/pre-heat/calcine, 3 dip/pre-heat/calcine, 3 dip/pre-heat, 1 calcine). In all cases, the electrodes subjected to 3 dip/pre-heat/calcine cycles showed the lowest initial ORR potentials and the lowest cycle-lives. The electrodes subjected to 3 dip/pre-heat cycles prior to calcination tended to show higher initial ORR potential and in all cases displayed the

highest cycle-life than the other dip/pre-heat-treat/calcine sequences for the same $Co(NO_3)_2$ concentration. The effect of the $Co(NO_3)_2$ concentration in the precursor dipping mixture on the initial ORR potential was inconclusive, while the 2.75 mol l^{-1} concentration tended to result in higher cycle life.

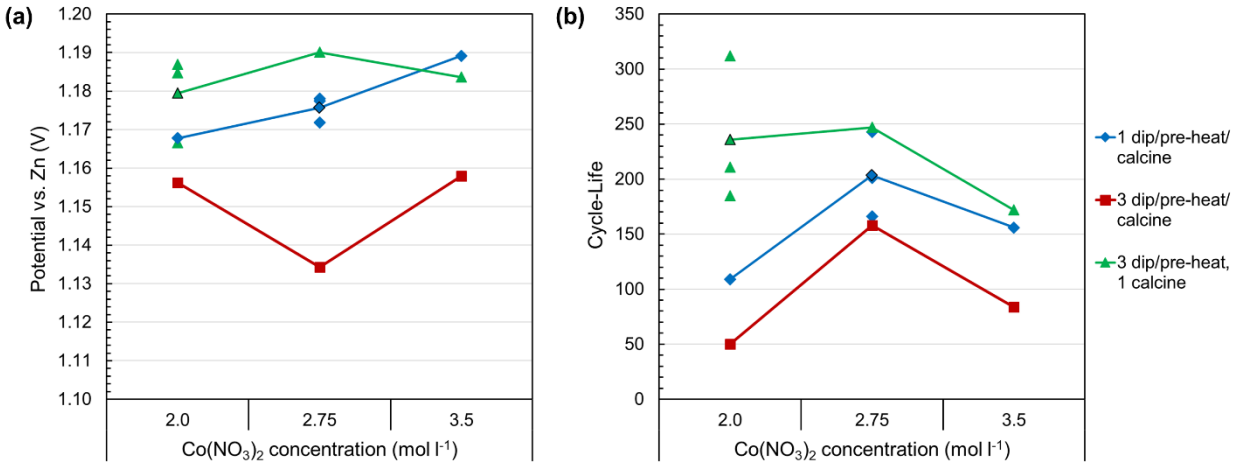

Figure 5.9. (a) Initial ORR potential vs. Zn and (b) cycle-life of thin nickel foam-based air electrodes at 20 mA cm^{-2} with the following two preparation factors: $Co(NO_3)_2$ concentration of precursor mixture for electrode dipping and dip/pre-heat-treat/calcine sequence. Initial ORR potential and cycle-life are defined in the **Figure 5.8** caption. The results in this figure are of Electrode #'s 6 and 9-16 in **Table 5.1**.

The means and variances of the initial ORR potential and cycle-life for the above two factors are summarized in **Table 5.10** and **Table 5.12** respectively, and associated ANOVA results are shown in **Table 5.11** and **Table 5.13** respectively. The ANOVA results confirmed that the choice of dip/pre-heat/calcine sequence significantly affected both the initial ORR potential and cycle-life of the electrode, but the difference in means of both performance metrics for the various

$Co(NO_3)_2$ concentrations was not statistically significant. The 3 dip/pre-heat, 1 calcine sequence was selected as the preferred production method since the electrodes resulting from this process achieved the highest cycle lives and mostly displayed the highest initial ORR potentials. Although the 2.75 mol l^{-1} $Co(NO_3)_2$ precursor concentration tended to result in higher cycle-lives, the 2.0 mol l^{-1} $Co(NO_3)_2$ concentration was selected due to the lower cost and lower toxicity associated with using a lower $Co(NO_3)_2$ concentration for electrode dipping. Further investigation is needed to determine if an even lower $Co(NO_3)_2$ concentration is feasible, and also if changing the PTFE concentrations in the precursor mixture would result in different ORR activities or cycle-lives.

Table 5.10. Means and variances of initial ORR potential (vs. Zn at 20 mA cm^{-2}) for thin nickel foam-based electrodes grouped by the following two preparation factors: $Co(NO_3)_2$ concentration of precursor mixture for electrode dipping and dip/pre-heat-treat/calcine sequence. Initial ORR potential and cycle-life are defined in the **Figure 5.8** caption.

D/P/C sequence / **$Co(NO_3)_2$ concentration**	1 dip/pre-heat/ calcine	3 dip/pre-heat/ calcine	3 dip/pre-heat, 1 calcine	**Mean**	**Variance**
2.0 mol l^{-1}	1.1678 V	1.1563 V	1.1795 V	1.1679 V	0.000134176
2.75 mol l^{-1}	1.1757 V	1.1343 V	1.1901 V	1.1667 V	0.00083946
3.5 mol l^{-1}	1.1892 V	1.1579 V	1.1836 V	1.1769 V	0.00027859
Mean	1.1776 V	1.1495 V	1.1844 V	1.1705 V	
Variance	0.000117041	0.00017392	2.87337E-05		0.000336422

Table 5.11. Two-factor ANOVA of initial ORR potential statistics in **Table 5.10**.

	SS	**df**	**MS**	**F**	**p-value**	**Significant? (α=0.05)**
$Co(NO_3)_2$ concentration	0.00018693	2	9.3463E-05	0.82625223	0.50076983	No
D/P/C sequence	0.00205199	2	0.00102599	9.07025546	0.03263959	Yes
Error (Within)	0.00045247	4	0.00011312			
Total	0.00269138	8	0.00033642			

Table 5.12. Means and variances of cycle-life (at 20 mA cm^{-2}) for thin nickel foam-based electrodes grouped by the following two preparation factors: $Co(NO_3)_2$ concentration of precursor mixture for electrode dipping and dip/pre-heat-treat/calcine sequence. Initial ORR potential and cycle-life are defined in the **Figure 5.8** caption

D/P/C sequence / **$Co(NO_3)_2$ concentration**	1 dip/pre-heat/ calcine	3 dip/pre-heat/ calcine	3 dip/pre-heat, 1 calcine	**Mean**	**Variance**
2.0 mol l^{-1}	109	50	236	132	9034
2.75 mol l^{-1}	203	158	247	203	1980
3.5 mol l^{-1}	156	84	172	137	2197
Mean	156	97	218	157	
Variance	2225	3049	1640		4475

Table 5.13. Two-factor ANOVA of cycle-life statistics in **Table 5.12**.

	SS	**df**	**MS**	**F**	**p-value**	**Significant? (α=0.05)**
$Co(NO_3)_2$ concentration	9372	2	4686	4.205592151	0.103870814	No
D/P/C sequence	21967	2	10984	9.857797377	0.028448013	Yes
Error (Within)	4457	4	1114			
Total	35796	8	4475			

Finally, the effect of the concentration of the PTFE emulsion used for applying the outer PTFE-coating was investigated by comparing three samples soaked in 15 wt.% PTFE to three samples soaked in 30 wt.% PTFE (three each of Electrode #'s 15 and 17 in **Table 5.1**). A two-sample two-tail t-test assuming unequal variance was performed on the two groups of initial ORR potentials and cycle-lives. As shown in **Table 5.14**, the electrode soaked in 30 wt.% PTFE had a higher average mean ORR potential, but the t-test result in **Table 5.15** showed that this difference was not statistically significant. Remarkably, however, the mean cycle-life of the electrodes soaked in 30 wt.% PTFE was 539, over double that of the 15 wt.% PTFE-soaked electrodes (**Table 5.16**),

which was shown to be statistically significant in **Table 5.17**. It should also be noted that Electrode #17 was produced using only 4-hour pre-heat-treatment steps for the first two of the three dip/pre-heat cycles, instead of the usual 16-hour times. This did not appear to have adverse affects on the electrode cycle life, at least not compared to the improvement from using a higher PTFE concentration for electrode soaking.

Table 5.14. Means and variances of initial ORR potential (vs. Zn at 20 mA cm^{-2}) for thin nickel foam-based electrodes prepared using 15 wt.% and 30 wt.% PTFE emulsions for outer PTFE-coating. Initial ORR potential is defined in the **Figure 5.8** caption. The results in this table are of Electrode #'s 15 and 17 in **Table 5.1**.

PTFE concentration for outer PTFE-coating	Count	Mean	Variance
15 wt.%	3	1.1795 V	0.00012537
30 wt.%	3	1.1912 V	0.00015050
Pooled			0.00013794

Table 5.15. Two-sample two-tail t-test assuming unequal variance of initial ORR potential statistics in **Table 5.14**.

	std err	t-stat	df	p-value	t-crit	Significant? (α=0.05)
Two Tail	0.00959	1.22703	3.96708	0.28761	2.78555	No

Table 5.16. Means and variances of cycle-life (at 20 mA cm^{-2}) for thin nickel foam-based electrodes prepared using 15 wt.% and 30 wt.% PTFE emulsions for outer PTFE-coating. Cycle-life is defined in the **Figure 5.8** caption. The results in this table are of Electrode #'s 15 and 17 in **Table 5.1**.

PTFE concentration for outer PTFE-coating	Count	Mean	Variance
15 wt.%	3	236	4501
30 wt.%	3	539	76
Pooled			2288.5

Table 5.17. Two-sample two-tail t-test assuming unequal variance of cycle-life statistics in **Table 5.16**.

	std err	t-stat	df	p-value	t-crit	Significant? (α=0.05)
Two Tail	39	7.757	2.068	0.0147	4.171	Yes

5.3.3 Specific Energy and Energy Density Estimation

To gain insight into the feasibility of using the developed thin nickel foam-based air electrode in a rechargeable zinc-air battery, the specific energy and energy density of an idealized zinc-air battery design using this air electrode and various reversible zinc electrodes evaluated in **Table 3.2** is calculated here. The specific energy (SE) and energy density (ED) of a zinc-air cell in an energy-dense configuration (electrolyte-soaked separator sandwiched between an air electrode and electrolyte-soaked zinc electrode, i.e. **Figure 3.2**) can be estimated according to **Equations 5.1**-**5.5**:

$$SE_{Zn-air\ cell} = \frac{AC_{Zn\ electrode}}{AM_{Zn-air\ cell}} \times V_{nominal} \quad \textbf{(Equation 5.1)}$$

$$AM_{Zn-air\ cell} = AM_{Air\ electrode} + AM_{Separator} + AM_{Electrolyte} + AM_{Zn\ electrode} \quad \textbf{(Equation 5.2)}$$

$$AM_{Electrolyte} = D_{Electrolyte} \times (P_{Separator} t_{Separator} + P_{Zn\ Electrode} t_{Zn\ Electrode}) \quad \textbf{(Equation 5.3)}$$

$$ED_{Zinc-air\ cell} = \frac{AC_{Zn\ electrode}}{t_{Zn-air\ cell}} \times V_{Nominal} \quad \textbf{(Equation 5.4)}$$

$$t_{Zn-air\ cell} = t_{Air\ \ electrode} + t_{Separator} + t_{Zn\ electrode}$$

(**Equation 5.5**)

where SE is specific energy, AC is areal capacity, AM is areal mass, V is voltage, D is density, P is porosity, and t is thickness. It should be noted that the mass of current collectors and cell casing is excluded from this analysis. The nominal voltage and the air electrode, separator and electrolyte properties used in **Equations 5.1**-**5.5** are shown in **Table 5.18**.

Table 5.18. Nominal voltage and air electrode, separator and electrolyte properties used for **Equations 5.1**-**5.5**.

$V_{nominal}$ (V)	1.1
$AM_{Air\ electrode}$ (g cm^{-2})	0.0491
$t_{Air\ electrode}$ (cm)	0.025
$AM_{Separator}$ (g cm^{-2})	0.00284
$t_{separator}$ (cm)	0.011
$P_{Separator}$	0.55
$D_{electrolyte}$ (6 mol l^{-1} KOH) (g cm^{-3})	1.25

Table 5.19 shows the results of performing these calculations. The idealized rechargeable zinc-air battery incorporating the thin nickel foam-based air electrode and either the 3D Zn sponge electrode[175] or the Bi-based nanoparticle coated Zn electrode[198] has competitive or better specific energy and energy densities in comparison to lithium-ion batteries (**Figure 2.4**), although this conclusion might change if the mass of current collectors and cell casings are taken into

account. However, both of these zinc electrodes have less than 100 demonstrated cycle lives, which may be insufficient even for automotive range-extender applications.[257] The other zinc electrodes considered here have higher cycle lives, but as seen in **Table 5.19**, their areal capacities are too low to enable a rechargeable zinc-air battery with competitive specific energy and energy density values even in the idealized cell calculation. Therefore, future work on zinc electrodes should prioritize achieving high cycle lives with areal capacities comparable to the 3D Zn sponge electrode or Bi-based nanoparticle coated Zn electrode in this analysis.

5.4 Conclusions

In this work, a thin nickel foam-based air electrode was designed and successfully demonstrated for use in electrically rechargeable zinc-air batteries. The electrode was 2-4 times lighter and thinner than previously reported nickel-based air electrodes, while displaying similar or better ORR/OER activities and a higher cycle-life than the previously investigated thick nickel-based air electrode. Specifically, more than 1100 charge-discharge cycles during over 700 hours of cycling at 10 mA cm^{-2} or more than 500 charge-discharge cycles during over 340 hours of operation at 20 mA cm^{-2} with a discharge potential over 1.0 V vs. Zn was observed. Calculations for an energy-dense zinc-air battery configuration were also performed, which showed that the thin nickel foam-based air electrode could enable competitive or better specific energy and energy density values compared to lithium-ion batteries, when paired with a high-areal capacity zinc electrode. The carbon-free design of the air electrode also makes it a promising candidate for use in zinc-air battery range-extender applications for EVs.

Table 5.19. Zinc electrode properties (from **Table 3.2**) and calculation of specific energy and energy density of rechargeable zinc-air batteries containing each zinc electrode paired with a thin nickel foam-based air electrode in an energy-dense configuration.

	3D Zn sponge electrode [175]	**Calcium zincate electrode** [195]	**Zn-Al-layer double oxide electrode** [165]	**Bi-based nanoparticle coated Zn electrode** [198]	**In-doped Zn electrode** [163]
$P_{Zn\ electrode}$ (higher)	0.795	0.75	0.75	0.75	0.75
$P_{Zn\ electrode}$ (lower)	0.795	0.60	0.60	0.60	0.60
$t_{Zn\ electrode}$ (lower) (cm)	0.100	0.020	0.020	0.030	0.028
$t_{Zn\ electrode}$ (higher) (cm)	0.400	0.020	0.020	0.030	0.028
$AC_{Zn\ electrode}$ (high Zn electrode porosity or low Zn electrode thickness) (mAh cm^{-2})	92.8	6.75	11.04	30.74	20.36
$AC_{Zn\ electrode}$ (low Zn electrode porosity or high Zn electrode thickness) (mAh cm^{-2})	371.2	10.80	17.66	49.19	32.58
$AM_{Zn\ electrode}$ (high Zn electrode porosity or low Zn electrode thickness) (g cm^{-2})	0.127	0.0175	0.0235	0.0468	0.0347
$AM_{Zn\ electrode}$ (low Zn electrode porosity or high Zn electrode thickness) (g cm^{-2})	0.510	0.0281	0.0376	0.0750	0.0556
$AM_{Electrolyte}$ (high Zn electrode porosity or low Zn electrode thickness) (g cm^{-2})	0.1069	0.0263	0.0263	0.0357	0.0338
$AM_{Electrolyte}$ (low Zn electrode porosity or high Zn electrode thickness) (g cm^{-2})	0.4051	0.0226	0.0226	0.0301	0.0286
$AM_{Zn\text{-}air\ cell}$ (high Zn electrode porosity or low Zn electrode thickness) (g cm^{-2})	0.2864	0.0958	0.1018	0.1345	0.1205
$AM_{Zn\text{-}air\ cell}$ (low Zn electrode porosity or high Zn electrode thickness) (g cm^{-2})	0.9669	0.1026	0.1121	0.1570	0.1361
$t_{Zn\text{-}air\ cell}$ (low Zn electrode thickness) (cm)	0.1360	0.0560	0.0560	0.0660	0.0640
$t_{Zn\text{-}air\ cell}$ (high Zn electrode thickness) (cm)	0.4360	0.0560	0.0560	0.0660	0.0640
$SE_{Zn\text{-}air\ cell}$ (high Zn electrode porosity or low Zn electrode thickness) (Wh kg^{-1})	356.5	77.5	119.3	251.5	185.9
$SE_{Zn\text{-}air\ cell}$ (low Zn electrode porosity or high Zn electrode thickness) (Wh kg^{-1})	422.3	115.9	173.3	344.7	263.3
$ED_{Zn\text{-}air\ cell}$ (high Zn electrode porosity or low Zn electrode thickness) (Wh L^{-1})	750.6	132.7	216.8	512.4	350.0
$ED_{Zn\text{-}air\ cell}$ (low Zn electrode porosity or high Zn electrode thickness) (Wh L^{-1})	936.5	212.2	346.9	819.8	560.0
Demonstrated cycle-life of Zn electrode	~25	250+	1000+	50+	73+

Chapter 6: Conclusions and Future Work

6.1 Conclusions

This thesis investigated the feasibility of using rechargeable zinc-air batteries for electric vehicle applications as well as electrode design considerations for achieving an energy-dense and long-lasting zinc-air battery cell. In **Chapter 2**, the energy and economic characteristics of zinc-air batteries in comparison to hydrogen fuel cells and a number of other batteries (lead-acid, nickel-metal hydride, lithium-sulfur, lithium-air) was thoroughly reviewed. Then, the potential abilities of these energy technologies to facilitate the growth of emerging electric vehicle markets, which so far have not been well served by the properties of lithium-ion batteries, were evaluated. Zinc-air batteries have the highest practically achievable volumetric energy density among the other batteries, as well as a potentially higher specific energy, lower or equal cost and better safety relative to lithium-ion batteries. The gives them the ability to possibly better serve the emerging long-range and low-cost electric vehicle markets, and unlike hydrogen fuel cells, would not rely on the global development of renewable hydrogen production and transportation infrastructure. However, the low specific power, energy efficiency and cycle-life of zinc-air batteries means that they likely will not act as a primary energy source for electric vehicles, and instead they should be paired with a high-power, high-efficiency and high-cycle life battery. The most logical dual-battery configuration that exploits the strengths and shelters the weaknesses of zinc-air batteries would employ them as a low-cost and energy-dense range-extender.

Chapter 3 provided an overview of the specific technology challenges that electrically-rechargeable zinc-air batteries are currently facing, with a specific lens placed on energy-dense zinc electrodes and configurations that need to be developed for electric vehicle range-extender applications. Four performance-limiting phenomena which typically hinder reversible zinc electrodes were detailed, namely dendrite growth, shape change, passivation/internal resistance and hydrogen evolution. Strategies to overcome these issues were summarized, and a selection of zinc electrodes from the literature incorporating one or more of these strategies was also evaluated. **Table 3.2** revealed that many zinc electrodes with high reported cycle-lives have quite low areal capacities, while those with higher areal capacities tend to have lower cycle-lives, highlighting the difficulty in optimizing both parameters simultaneously. Electrode design fundamentals for bifunctional air electrodes were then reviewed, including their general architecture and the flooded agglomerate model which explains the need for a balance of hydrophobic and hydrophilic properties as well as electronic conductivity in the electrode design. Carbon-based materials and substrates together with polytetrafluoroethylene (PTFE) have conventionally been used to achieve these properties, but for zinc-air batteries with long calendar lives needed for EV range-extender applications, durable and corrosion-resistant metals such as nickel offer a promising alternative to carbon. Nickel-based air electrodes, however, have received relatively little attention in the literature, which provided the motivation for the experimental investigations in **Chapters 4** and **5** of the thesis.

In **Chapter 4**, the failure mechanism of nickel-based air electrodes in rechargeable zinc-air batteries was investigated. Nickel metal forms a passivating (oxy)hydroxide film when exposed to

the alkaline electrolyte of rechargeable zinc-air batteries, preventing the structure from breaking down due to corrosion. However, the (oxy)hydroxide film also grows progressively thicker when the air electrode is subjected to repeated ORR and OER cycling. Since this film also converts between $Ni(OH)_2$ and NiOOH with relatively low overpotentials at the beginning of each charge and discharge cycle, cut-off voltages were introduced into a "two-step" cycling regime that enabled electrochemical tracking of the (oxy)hydroxide film growth during the battery cycling. A correlation between the film growth and a loss of ORR activity mainly caused by mass transfer losses was revealed, and SEM, XRD and XPS analyses provided corroborating evidence of increasing resistance to oxygen transport caused by the film growing overtop of the metal-supported catalyst.

Finally, in **Chapter 5**, a new nickel-based air electrode design with dramatically improved cycle-life and 2-4 times lower thickness and weight than previously proposed designs was introduced. This electrode, produced by a simple dip-coating procedure in a mixture of cobalt nitrate and PTFE particles, displayed over 1100 charge-discharge cycles at 10 mA cm^{-2}, over 500 charge-discharge cycles at 20 mA cm^{-2} and over 100 charge-discharge cycles at 50 mA cm^{-2} while maintaining an ORR potential greater than 1.0 V vs. Zn. The improved cycle-life was attributed to the absence of nickel metal powder and uniformly coated nickel foam struts, both resulting in slower nickel (oxy)hydroxide film growth, as well as the presence of sisal-like Co_3O_4 branches intermixed with PTFE particles, which were hypothesized to provide a beneficial balance between hydrophobic and hydrophilic properties needed for high-current cycling operation. The specific energy and energy density of a hypothetical rechargeable zinc-air battery incorporating the thin

nickel foam-based air electrode and the zinc electrodes evaluated in **Chapter 3** were calculated, showing values which were competitive or better than lithium-ion batteries if the zinc electrode had a relatively high areal capacity. Therefore, the thin, light-weight, high-stability, carbon-free and easily reproducible air electrode developed in this work could be an ideal choice to employ in a durable and energy-dense rechargeable zinc-air battery for electric vehicle range-extender applications.

6.2 Future Work

Based on the results of this thesis, three major recommendations for future work are provided here. First, more fundamental research on the performance and failure mechanism of nickel-based air electrodes should be completed. For instance, cross-sectional SEM or transmission electron microscopy (TEM) characterization of the air electrode after cycling could more directly confirm the presence of the nickel (oxy)hydroxide layer overtop of the catalyst-coated electrode. Further SEM, XPS and XRD analyses before and after electrochemical cycling should also be carried out with direct comparisons made between cobalt nitrate-coated electrodes and mixed PTFE/cobalt nitrate-coated electrodes, as well as between Co_3O_4-coated electrodes and $NiCo_2O_4$-coated electrodes, to provide further insight into the morphological, crystallographic and surface chemistry changes (and their relative rates) resulting from electrochemical operation. This could enable a more detailed understanding of the mechanism in which the nickel (oxy)hydroxide film growth interacts or interferes with the catalyst, and how the various preparation methods affect this mechanism, which could in turn lead to better preparation methods for enabling electrodes

with higher durability or higher current operability. Additionally, other metal-based air electrodes could be investigated in terms of their oxide growth rates, post-cycling morphologies, and ultimately their electrochemical durability compared to nickel-based air electrodes.

Secondly, further design and testing of the thin nickel foam-based air electrode (or other metal-based air electrodes) should be completed. Several design factors were not explored in this work, such as the nickel foam thickness and the concentration of PTFE in the precursor dip-coating solution, while other parameters such as possibly even lower cobalt nitrate concentration, more precisely optimized outer-PTFE coating emulsion concentration, and other heat-treatment/calcination temperatures and times could use further investigation. Additionally, protective coatings with sufficient electronic conductivity could also be applied to the nickel foam before applying the catalyst/PTFE layer in order to provide a barrier between the nickel metal foam and electrolyte, thus reducing its oxidation rate during electrochemical cycling. Long-term operational testing of the air electrodes, including long periods of inactivity between charge/discharge cycles, should also be conducted to determine whether the electrode can provide a long calendar-life in addition to its long cycle-life. An air electrode that shows long calendar-life in addition to long cycle-life is ultimately what would be needed to enable long-lasting zinc-air battery range-extenders in electric vehicles.

The last major recommendation arising from this work is to spend significant efforts on the zinc electrode design and total cell design. Zinc electrodes with high areal capacities and decent cycle-lives are necessary to enable energy-dense, electrically rechargeable zinc-air batteries for electric vehicle applications. Testing and designing of both the zinc electrode and air electrode for

operation in an energy-dense cell configuration should also be prioritized, since their cycle-lives and also the overall durability of the whole cell is likely to face more challenges in a minimum-electrolyte configuration. Hydrophilic materials or gelled electrolytes will likely need to be developed to prevent electrolyte evaporation, and hydrogen evolution at the zinc electrode will also need to receive greater consideration in the minimum-electrolyte configuration to minimize electrolyte consumption. Ultimately, full-cell testing under cycling protocols relevant to electric vehicle range-extenders is needed to fully evaluate the potential of zinc-air batteries in this application.

Letters of Copyright Permission

1. John Wiley and Sons / Advanced Materials

JOHN WILEY AND SONS LICENSE
TERMS AND CONDITIONS
Jan 17, 2020

This Agreement between Zachary P Cano ("You") and John Wiley and Sons ("John Wiley and Sons") consists of your license details and the terms and conditions provided by John Wiley and Sons and Copyright Clearance Center.

License Number	4751430928543
License date	Jan 17, 2020
Licensed Content Publisher	John Wiley and Sons
Licensed Content Publication	Advanced Materials
Licensed Content Title	Electrically Rechargeable Zinc–Air Batteries: Progress, Challenges, and Perspectives
Licensed Content Author	Zhongwei Chen, Michael Fowler, Aiping Yu, et al
Licensed Content Date	Nov 28, 2016
Licensed Content Volume	29
Licensed Content Issue	7
Licensed Content Pages	34
Type of use	Dissertation/Thesis
Requestor type	Author of this Wiley article
Format	Electronic
Portion	Full article
Will you be translating?	No
Title of your thesis / dissertation	Electrode Design for Durable and Energy-Dense Rechargeable Zinc-Air Batteries
Expected completion date	Jan 2020
Expected size (number of pages)	174
Requestor Location	Zachary P Cano Department of Chemical Engineering University of Waterloo

	200 University Avenue West Waterloo, ON N2L3G1 Canada Attn: Zachary P Cano
Publisher Tax ID	EU826007151
Total	0.00 CAD
Terms and Conditions	

TERMS AND CONDITIONS

This copyrighted material is owned by or exclusively licensed to John Wiley & Sons, Inc. or one of its group companies (each a"Wiley Company") or handled on behalf of a society with which a Wiley Company has exclusive publishing rights in relation to a particular work (collectively "WILEY"). By clicking "accept" in connection with completing this licensing transaction, you agree that the following terms and conditions apply to this transaction (along with the billing and payment terms and conditions established by the Copyright Clearance Center Inc., ("CCC's Billing and Payment terms and conditions"), at the time that you opened your RightsLink account (these are available at any time at http://myaccount.copyright.com).

Terms and Conditions

- The materials you have requested permission to reproduce or reuse (the "Wiley Materials") are protected by copyright.

- You are hereby granted a personal, non-exclusive, non-sub licensable (on a stand-alone basis), non-transferable, worldwide, limited license to reproduce the Wiley Materials for the purpose specified in the licensing process. This license, **and any CONTENT (PDF or image file) purchased as part of your order,** is for a one-time use only and limited to any maximum distribution number specified in the license. The first instance of republication or reuse granted by this license must be completed within two years of the date of the grant of this license (although copies prepared before the end date may be distributed thereafter). The Wiley Materials shall not be used in any other manner or for any other purpose, beyond what is granted in the license. Permission is granted subject to an appropriate acknowledgement given to the author, title of the material/book/journal and the publisher. You shall also duplicate the copyright notice that appears in the Wiley publication in your use of the Wiley Material. Permission is also granted on the understanding that nowhere in the text is a previously published source acknowledged for all or part of this Wiley Material. Any third party content is expressly excluded from this permission.

- With respect to the Wiley Materials, all rights are reserved. Except as expressly granted by the terms of the license, no part of the Wiley Materials may be copied, modified, adapted (except for minor reformatting required by the new Publication), translated, reproduced, transferred or distributed, in any form or by any means, and no derivative works may be made based on the Wiley Materials without the prior permission of the respective copyright owner.**For STM Signatory Publishers clearing permission under the terms of the STM Permissions Guidelines only, the terms of the license are extended to include subsequent editions and for editions in other languages, provided such editions are for the work as a whole in situ and does not involve the separate exploitation of the permitted figures or extracts,** You may not alter, remove or suppress in any manner any copyright, trademark or other notices displayed by the Wiley Materials. You may not license, rent, sell, loan, lease, pledge, offer as security, transfer or assign the Wiley Materials on a stand-alone basis, or any of the rights granted to you hereunder to any other person.

- The Wiley Materials and all of the intellectual property rights therein shall at all times remain the exclusive property of John Wiley & Sons Inc, the Wiley Companies, or their respective licensors, and your interest therein is only that of having possession of and the right to reproduce the Wiley Materials pursuant to Section 2 herein during the continuance of this Agreement. You agree that you own no right, title or interest in or to the Wiley Materials or any of the intellectual property rights therein. You shall have no rights hereunder other than the license as provided for above in Section 2. No right, license or interest to any trademark, trade name, service mark or other branding ("Marks") of WILEY or its licensors is granted hereunder, and you agree that you shall not assert any such right, license or interest with respect thereto

- NEITHER WILEY NOR ITS LICENSORS MAKES ANY WARRANTY OR REPRESENTATION OF ANY KIND TO YOU OR ANY THIRD PARTY, EXPRESS, IMPLIED OR STATUTORY, WITH RESPECT TO THE MATERIALS OR THE ACCURACY OF ANY INFORMATION CONTAINED IN THE MATERIALS, INCLUDING, WITHOUT LIMITATION, ANY IMPLIED WARRANTY OF MERCHANTABILITY, ACCURACY, SATISFACTORY QUALITY, FITNESS FOR A PARTICULAR PURPOSE, USABILITY, INTEGRATION OR NON-INFRINGEMENT AND ALL SUCH WARRANTIES ARE HEREBY EXCLUDED BY WILEY AND ITS LICENSORS AND WAIVED BY YOU.

- WILEY shall have the right to terminate this Agreement immediately upon breach of this Agreement by you.

- You shall indemnify, defend and hold harmless WILEY, its Licensors and their respective directors, officers, agents and employees, from and against any actual or threatened claims, demands, causes of action or proceedings arising from any breach of this Agreement by you.

- IN NO EVENT SHALL WILEY OR ITS LICENSORS BE LIABLE TO YOU OR ANY OTHER PARTY OR ANY OTHER PERSON OR ENTITY FOR ANY SPECIAL, CONSEQUENTIAL, INCIDENTAL, INDIRECT, EXEMPLARY OR PUNITIVE DAMAGES, HOWEVER CAUSED, ARISING OUT OF OR IN CONNECTION WITH THE DOWNLOADING, PROVISIONING, VIEWING OR USE OF THE MATERIALS REGARDLESS OF THE FORM OF ACTION, WHETHER FOR BREACH OF CONTRACT, BREACH OF WARRANTY, TORT, NEGLIGENCE, INFRINGEMENT OR OTHERWISE (INCLUDING, WITHOUT LIMITATION, DAMAGES BASED ON LOSS OF PROFITS, DATA, FILES, USE, BUSINESS OPPORTUNITY OR CLAIMS OF THIRD PARTIES), AND WHETHER OR NOT THE PARTY HAS BEEN ADVISED OF THE POSSIBILITY OF SUCH DAMAGES. THIS LIMITATION SHALL APPLY NOTWITHSTANDING ANY FAILURE OF ESSENTIAL PURPOSE OF ANY LIMITED REMEDY PROVIDED HEREIN.

- Should any provision of this Agreement be held by a court of competent jurisdiction to be illegal, invalid, or unenforceable, that provision shall be deemed amended to achieve as nearly as possible the same economic effect as the original provision, and the legality, validity and enforceability of the remaining provisions of this Agreement shall not be affected or impaired thereby.

- The failure of either party to enforce any term or condition of this Agreement shall not constitute a waiver of either party's right to enforce each and every term and condition of this Agreement. No breach under this agreement shall be deemed waived or excused by either party unless such waiver or consent is in writing signed by the party granting such waiver or consent. The waiver by or consent of a party to a breach of any provision of this Agreement shall not operate or be construed as a waiver of or consent to any other or subsequent breach by such other party.

- This Agreement may not be assigned (including by operation of law or otherwise) by you without WILEY's prior written consent.

- Any fee required for this permission shall be non-refundable after thirty (30) days from receipt by the CCC.

- These terms and conditions together with CCC's Billing and Payment terms and conditions (which are incorporated herein) form the entire agreement between you and WILEY concerning this licensing transaction and (in the absence of fraud)

supersedes all prior agreements and representations of the parties, oral or written. This Agreement may not be amended except in writing signed by both parties. This Agreement shall be binding upon and inure to the benefit of the parties' successors, legal representatives, and authorized assigns.

- In the event of any conflict between your obligations established by these terms and conditions and those established by CCC's Billing and Payment terms and conditions, these terms and conditions shall prevail.

- WILEY expressly reserves all rights not specifically granted in the combination of (i) the license details provided by you and accepted in the course of this licensing transaction, (ii) these terms and conditions and (iii) CCC's Billing and Payment terms and conditions.

- This Agreement will be void if the Type of Use, Format, Circulation, or Requestor Type was misrepresented during the licensing process.

- This Agreement shall be governed by and construed in accordance with the laws of the State of New York, USA, without regards to such state's conflict of law rules. Any legal action, suit or proceeding arising out of or relating to these Terms and Conditions or the breach thereof shall be instituted in a court of competent jurisdiction in New York County in the State of New York in the United States of America and each party hereby consents and submits to the personal jurisdiction of such court, waives any objection to venue in such court and consents to service of process by registered or certified mail, return receipt requested, at the last known address of such party.

WILEY OPEN ACCESS TERMS AND CONDITIONS

Wiley Publishes Open Access Articles in fully Open Access Journals and in Subscription journals offering Online Open. Although most of the fully Open Access journals publish open access articles under the terms of the Creative Commons Attribution (CC BY) License only, the subscription journals and a few of the Open Access Journals offer a choice of Creative Commons Licenses. The license type is clearly identified on the article.

The Creative Commons Attribution License

The Creative Commons Attribution License (CC-BY) allows users to copy, distribute and transmit an article, adapt the article and make commercial use of the article. The CC-BY license permits commercial and non-

Creative Commons Attribution Non-Commercial License

The Creative Commons Attribution Non-Commercial (CC-BY-NC)License permits use, distribution and reproduction in any medium, provided the original work is properly cited and is not used for commercial purposes.(see below)

Creative Commons Attribution-Non-Commercial-NoDerivs License

The Creative Commons Attribution Non-Commercial-NoDerivs License (CC-BY-NC-ND) permits use, distribution and reproduction in any medium, provided the original work is properly cited, is not used for commercial purposes and no modifications or adaptations are made. (see below)

Use by commercial "for-profit" organizations

Use of Wiley Open Access articles for commercial, promotional, or marketing purposes requires further explicit permission from Wiley and will be subject to a fee.

Further details can be found on Wiley Online Library http://olabout.wiley.com/WileyCDA/Section/id-410895.html

Other Terms and Conditions:

v1.10 Last updated September 2015

Questions? customercare@copyright.com or +1-855-239-3415 (toll free in the US) or +1-978-646-2777.

2. Springer Nature / Nature Energy

Batteries and fuel cells for emerging electric vehicle markets

Author: Zachary P. Cano et al

Publication: Nature Energy

Publisher: Springer Nature

Date: Apr 12, 2018

For full paper portion: Authors of original research papers published by Springer Nature are encouraged to submit the author's version of the accepted, peer-reviewed manuscript to their relevant funding body's archive, for release six months after publication. In addition, authors are encouraged to archive their version of the manuscript in their institution's repositories (as well as their personal Web sites), also six months after original publication.

v1.0

3. American Chemical Society / The Journal of Physical Chemistry C

New Interpretation of the Performance of Nickel-Based Air Electrodes for Rechargeable Zinc–Air Batteries

Author: Zachary P. Cano, Moon Gyu Park, Dong Un Lee, et al

Publication: The Journal of Physical Chemistry C

Publisher: American Chemical Society

Date: Sep 1, 2018

References

[1] C. Breyer, A. Gerlach, *Prog. Photovolt. Res. Appl.* **2013**, *21*, 121.
[2] L. A. H. Munoz, J. C. C. M. Huijben, B. Verhees, G. P. J. Verbong, *Technol. Forecast. Soc. Change* **2014**, *87*, 179.
[3] J. B. Goodenough, K.-S. Park, *J. Am. Chem. Soc.* **2013**, *135*, 1167.
[4] S. Goriparti, E. Miele, F. De Angelis, E. Di Fabrizio, R. Proietti Zaccaria, C. Capiglia, *J. Power Sources* **2014**, *257*, 421.
[5] E. Shafiei, H. Thorkelsson, E. I. Ásgeirsson, B. Davidsdottir, M. Raberto, H. Stefansson, *Technol. Forecast. Soc. Change* **2012**, *79*, 1638.
[6] B. Propfe, D. Kreyenberg, J. Wind, S. Schmid, *Int. J. Hydrog. Energy* **2013**, *38*, 5201.
[7] O. Egbue, S. Long, *Energy Policy* **2012**, *48*, 717.
[8] M. A. Rahman, X. Wang, C. Wen, *J. Electrochem. Soc.* **2013**, *160*, A1759.
[9] S. R. Narayanan, G. K. S. Prakash, A. Manohar, B. Yang, S. Malkhandi, A. Kindler, *Solid State Ion.* **2012**, *216*, 105.
[10] X. Ren, Y. Wu, *J. Am. Chem. Soc.* **2013**, *135*, 2923.
[11] P. Hartmann, C. L. Bender, M. Vračar, A. K. Dürr, A. Garsuch, J. Janek, P. Adelhelm, *Nat. Mater.* **2013**, *12*, 228.
[12] J.-S. Lee, S. Tai Kim, R. Cao, N.-S. Choi, M. Liu, K. T. Lee, J. Cho, *Adv. Energy Mater.* **2011**, *1*, 34.
[13] J. Muldoon, C. B. Bucur, T. Gregory, *Chem. Rev.* **2014**, *114*, 11683.
[14] A. J. Appleby, J. Jacquelin, J. P. Pompon, *SAE Tech. Pap.* **1977**, *770381*, DOI 10.4271/770381.
[15] P. N. J. Ross, in *Proceedlngs 21st Intersoc. Energy Convers. Eng. Conf.*, San Diego, California, **1986**.
[16] M. C. Cheiky, L. G. Danczyk, M. C. Wehrey, *SAE Tech. Pap.* **1990**, *901516*, DOI 10.4271/901516.
[17] M. C. Cheiky, L. G. Danczyk, R. L. Scheffler, in *Battery Conf. Appl. Adv. 1991 Proc. Sixth Annu.*, **1991**, pp. 29–36.
[18] L. G. Danczyk, R. L. Scheffler, R. S. Hobbs, *SAE Tech. Pap.* **1991**, *911633*, DOI 10.4271/911633.
[19] G. W. Merry, *SAE Tech. Pap.* **1991**, *911912*, DOI 10.4271/911912.
[20] M. C. Cheiky, L. G. Danczyk, M. C. Wehrey, *SAE Tech. Pap.* **1992**, *920448*, DOI 10.4271/920448.
[21] J. R. Goldstein, B. Koretz, *IEEE Aerosp. Electron. Syst. Mag.* **1993**, *8*, 34.
[22] C. Clark, K. Kinoshita, *Zinc/Air Technology, December 1993 Meeting Report*, Sandia National Labs., Albuquerque, NM (United States), **1994**.
[23] P. N. Ross, in *Battery Conf. Appl. Adv. 1995 Proc. Tenth Annu.*, **1995**, pp. 131–133.

[24] J. F. Cooper, D. Fleming, D. Hargrove, R. Koopman, K. Peterman, *SAE Tech. Pap.* **1995**, *951948*, DOI 10.4271/951948.
[25] D. Sieminski, in *Battery Conf. Appl. Adv. 1997 Twelfth Annu.*, IEEE, Long Beach, CA, **1997**, pp. 171–180.
[26] F. G. Will, in *Battery Conf. Appl. Adv. 1998 Thirteen. Annu.*, **1998**, pp. 1–6.
[27] J. Goldstein, I. Brown, B. Koretz, *J. Power Sources* **1999**, *80*, 171.
[28] K. Tweed, "Eos Energy Storage Closes $23M Funding Round for Cheap Grid Batteries," can be found under http://www.greentechmedia.com/articles/read/eos-energy-storage-closes-23m-funding-round, **2015**.
[29] E. Wesoff, "Fluidic Energy Is the Biggest Zinc-Air Battery Startup You Haven't Heard Of," can be found under http://www.greentechmedia.com/articles/read/Fluidic-Energy-is-the-Biggest-Zinc-Air-Battery-Startup-You-Havent-Heard-Of, **2015**.
[30] N. R. C. Government of Canada, "Canada News Centre - Archived - Government of Canada and SDTC Announce New Clean Technology Funding in British Columbia," can be found under http://news.gc.ca/web/article-en.do?nid=950589, **2015**.
[31] Y. Li, H. Dai, *Chem. Soc. Rev.* **2014**, *43*, 5257.
[32] S. G. Stewart, S. I. Kohn, K. R. Kelty, J. B. Straubel, *Electric Vehicle Extended Range Hybrid Battery Pack System*, **2013**, US8471521 B2.
[33] R. Eckl, P. Burda, A. Foerg, H. Finke, P. D.-I. M. Lienkamp, in *Conf. Future Automot. Technol.* (Ed.: M. Lienkamp), Springer Fachmedien Wiesbaden, **2013**, pp. 3–18.
[34] A. Santos, N. McGuckin, H. Y. Nakamoto, D. Gray, S. Liss, **2011**.
[35] M. Guarnieri, in *2012 Third IEEE Hist. Electro-Technol. Conf. HISTELCON*, **2012**, pp. 1–6.
[36] "Global Plug-in Sales for 2016," can be found under http://www.ev-volumes.com/news/global-plug-in-sales-for-2016/, **2017**.
[37] *Energy Technology Perspectives 2017*, International Energy Agency, Paris, **2017**.
[38] S. Castle, *N. Y. Times* **2017**.
[39] M. Hocking, J. Kan, P. Young, C. Terry, D. Begleiter, *Welcome to the Lithium-Ion Age*, Deutsche Bank Markets Research, **2016**.
[40] T. Placke, R. Kloepsch, S. Dühnen, M. Winter, *J. Solid State Electrochem.* **2017**, *21*, 1939.
[41] S. Saxena, J. MacDonald, S. Moura, *Appl. Energy* **2015**, *157*, 720.
[42] B. Nykvist, M. Nilsson, *Nat. Clim. Change* **2015**, *5*, 329.
[43] O. Schmidt, A. Hawkes, A. Gambhir, I. Staffell, *Nat. Energy* **2017**, *6*, nenergy2017110.
[44] C. Curry, "Lithium-ion Battery Costs: Squeezed Margins and New Business Models," can be found under https://about.bnef.com/blog/lithium-ion-battery-costs-squeezed-margins-new-business-models/, **2017**.
[45] S. M. Knupfer, R. Hensley, P. Hertzke, P. Schaufuss, N. Laverty, N. Kramer, *Electrifying Insights: How Automakers Can Drive Electrified Vehicle Sales and Profitability | McKinsey & Company*, McKinsey & Company, **2017**.
[46] W. Sierzchula, S. Bakker, K. Maat, B. van Wee, *Energy Policy* **2014**, *68*, 183.
[47] *Global EV Outlook 2017: Two Million and Counting*, International Energy Agency, **2017**.
[48] M. Singer, *Consumer Views on Plug-in Electric Vehicles–National Benchmark Report (Second Edition)*, National Renewable Energy Laboratory (NREL), Golden, CO, **2016**.

[49] W. Li, R. Long, H. Chen, J. Geng, *Renew. Sustain. Energy Rev.* **2017**, *78*, 318.
[50] A. Dimitropoulos, P. Rietveld, J. N. van Ommeren, *Transp. Res. Part Policy Pract.* **2013**, *55*, 27.
[51] J. R. Kenworthy, F. B. Laube, *Transp. Res. Part Policy Pract.* **1999**, *33*, 691.
[52] M. Liebreich, **2017**.
[53] J. Dahn, G. M. Ehrlich, in *Linden's Handb. Batter. Fourth Ed.*, McGraw Hill Professional, Access Engineering, New York, **2011**.
[54] D. Andre, S.-J. Kim, P. Lamp, S. F. Lux, F. Maglia, O. Paschos, B. Stiaszny, *J. Mater. Chem. A* **2015**, *3*, 6709.
[55] M. Hagen, D. Hanselmann, K. Ahlbrecht, R. Maça, D. Gerber, J. Tübke, *Adv. Energy Mater.* **2015**, *5*, n/a.
[56] O. Gröger, H. A. Gasteiger, J.-P. Suchsland, *J. Electrochem. Soc.* **2015**, *162*, A2605.
[57] K. Kerman, A. Luntz, V. Viswanathan, Y.-M. Chiang, Z. Chen, *J. Electrochem. Soc.* **2017**, *164*, A1731.
[58] L. Fulton, A. Jenn, G. Tal, *GFEI Working Paper 16: Can We Reach 100 Million Electric Cars Worldwide by 2030? A Modelling/Scenario Analysis*, Global Fuel Economy Initiative, **2017**.
[59] D. McFadden, **1973**.
[60] "Chinese-Made Electric Cars," can be found under http://chinaautoweb.com/electric-cars/, **n.d.**
[61] *The Future of Trucks - Implications for Energy and the Environment*, International Energy Agency, **2017**.
[62] J.-Q. Li, *Int. J. Sustain. Transp.* **2016**, *10*, 157.
[63] Y. Ye, L. H. Saw, Y. Shi, K. Somasundaram, A. A. O. Tay, *Electrochimica Acta* **2014**, *134*, 327.
[64] Q. Liu, C. Du, B. Shen, P. Zuo, X. Cheng, Y. Ma, G. Yin, Y. Gao, *RSC Adv.* **2016**, *6*, 88683.
[65] Y. Gao, J. Jiang, C. Zhang, W. Zhang, Z. Ma, Y. Jiang, *J. Power Sources* **2017**, *356*, 103.
[66] E. Akhavan-Rezai, M. F. Shaaban, E. F. El-Saadany, A. Zidan, in *2012 IEEE Power Energy Soc. Gen. Meet.*, **2012**, pp. 1–7.
[67] C. H. Dharmakeerthi, N. Mithulananthan, T. K. Saha, *Int. J. Electr. Power Energy Syst.* **2014**, *57*, 241.
[68] P. Liu, R. Ross, A. Newman, *MRS Energy Amp Sustain.- Rev. J.* **2015**, *2*, DOI 10.1557/mre.2015.13.
[69] S. Sripad, V. Viswanathan, *ACS Energy Lett.* **2017**, *2*, 1669.
[70] Y. Yamaguchi, in *Encycl. Appl. Electrochem.* (Eds.: G. Kreysa, K. Ota, R.F. Savinell), Springer New York, New York, **2014**, pp. 1161–1165.
[71] W. Liu, L. Chen, J. Tian, *Environ. Sci. Technol.* **2016**, *50*, 5412.
[72] J. Jung, L. Zhang, J. Zhang, *Lead-Acid Battery Technologies: Fundamentals, Materials, and Applications*, CRC Press, Boca Raton, **2015**.
[73] J. X. Weinert, A. F. Burke, X. Wei, *J. Power Sources* **2007**, *172*, 938.
[74] A. Salkind, G. Zguris, in *Linden's Handb. Batter. Fourth Ed.*, McGraw Hill Professional, Access Engineering, New York, **2011**.

[75] P. T. Moseley, D. A. J. Rand, K. Peters, *J. Power Sources* **2015**, *295*, 268.
[76] J. Yang, C. Hu, H. Wang, K. Yang, J. B. Liu, H. Yan, *Int. J. Energy Res.* **2017**, *41*, 336.
[77] E. Karden, S. Ploumen, B. Fricke, T. Miller, K. Snyder, *J. Power Sources* **2007**, *168*, 2.
[78] A. Jaiswal, S. C. Chalasani, *J. Energy Storage* **2015**, *1*, 15.
[79] The Advanced Lead-Acid Battery Consortium, "Lead-Carbon Batteries to Boost Market Prospects of 48V Hybrids — ALABC," can be found under http://www.alabc.org/press-releases/lead-carbon-batteries-to-boost-market-prospects-of-48v-hybrids, **n.d.**
[80] M. Fetcenko, J. Koch, in *Linden's Handb. Batter. Fourth Ed.*, McGraw Hill Professional, Access Engineering, New York, **2011**.
[81] A. Manthiram, Y. Fu, S.-H. Chung, C. Zu, Y.-S. Su, *Chem. Rev.* **2014**, *114*, 11751.
[82] D. Eroglu, K. R. Zavadil, K. G. Gallagher, *J. Electrochem. Soc.* **2015**, *162*, A982.
[83] Y.-X. Yin, S. Xin, Y.-G. Guo, L.-J. Wan, *Angew. Chem. Int. Ed.* **2013**, *52*, 13186.
[84] X.-B. Cheng, J.-Q. Huang, Q. Zhang, *J. Electrochem. Soc.* **2018**, *165*, A6058.
[85] M. A. Pope, I. A. Aksay, *Adv. Energy Mater.* **2015**, *5*, 1500124.
[86] P. Bonnick, E. Nagai, J. Muldoon, *J. Electrochem. Soc.* **2018**, *165*, A6005.
[87] Q.-C. Liu, T. Liu, D.-P. Liu, Z.-J. Li, X.-B. Zhang, Y. Zhang, *Adv. Mater.* **2016**, *28*, 8413.
[88] F. Mizuno, S. Nakanishi, Y. Kotani, S. Yokoishi, H. Iba, *Electrochemistry* **2010**, *78*, 403.
[89] A. C. Luntz, B. D. McCloskey, *Chem. Rev.* **2014**, *114*, 11721.
[90] A. Manthiram, L. Li, *Adv. Energy Mater.* **2015**, *5*, n/a.
[91] J. Christensen, P. Albertus, R. S. Sanchez-Carrera, T. Lohmann, B. Kozinsky, R. Liedtke, J. Ahmed, A. Kojic, *J. Electrochem. Soc.* **2012**, *159*, R1.
[92] K. G. Gallagher, S. Goebel, T. Greszler, M. Mathias, W. Oelerich, D. Eroglu, V. Srinivasan, *Energy Environ. Sci.* **2014**, *7*, 1555.
[93] Y. Li, J. Lu, *ACS Energy Lett.* **2017**, *2*, 1370.
[94] K. F. Blurton, A. F. Sammells, *J. Power Sources* **1979**, *4*, 263.
[95] T. B. Atwater, A. Dobley, in *Lindens Handb. Batter. 4th Ed.*, McGraw Hill Professional, New York, **2010**.
[96] R. Eckl, B. Ehrl, M. Lienkamp, **2013**.
[97] J. Bockstette, K. Habermann, J. Ogrzewalla, M. Pischinger, D. Seibert, *SAE Int. J. Altern. Powertrains* **2013**, *2*, 156.
[98] F. Larsson, A. Rytinki, I. Ahmed, I. Albinsson, B.-E. Mellander, *Batteries* **2017**, *3*, 1.
[99] B. Pivovar, *H2 at Scale: Deeply Decarbonizing Our Energy System*, NREL (National Renewable Energy Laboratory (NREL), Golden, CO (United States)), **2016**.
[100] *Technology Roadmap: Hydrogen and Fuel Cells*, International Energy Agency, Paris, **2017**.
[101] J. Pontes, "Fuel Cells 2016," can be found under http://ev-sales.blogspot.com/2017/02/fuel-cells-2016.html, **n.d.**
[102] "Toyota Mirai US car sales figures," can be found under http://carsalesbase.com/us-car-sales-data/toyota/toyota-mirai/, **n.d.**
[103] N. Guerrero Moreno, M. Cisneros Molina, D. Gervasio, J. F. Pérez Robles, *Renew. Sustain. Energy Rev.* **2015**, *52*, 897.
[104] M. Wei, S. J. Smith, M. D. Sohn, *Appl. Energy* **2017**, *191*, 346.
[105] M. Miotti, J. Hofer, C. Bauer, *Int. J. Life Cycle Assess.* **2017**, *22*, 94.

[106] A. Kongkanand, M. F. Mathias, *J. Phys. Chem. Lett.* **2016**, *7*, 1127.
[107] J. Wang, *Energy* **2015**, *80*, 509.
[108] D. Banham, S. Ye, K. Pei, J. Ozaki, T. Kishimoto, Y. Imashiro, *J. Power Sources* **2015**, *285*, 334.
[109] D. Banham, T. Kishimoto, T. Sato, Y. Kobayashi, K. Narizuka, J. Ozaki, Y. Zhou, E. Marquez, K. Bai, S. Ye, *J. Power Sources* **2017**, *344*, 39.
[110] F. T. Wagner, B. Lakshmanan, M. F. Mathias, *J. Phys. Chem. Lett.* **2010**, *1*, 2204.
[111] *Fuel Cells Bull.* **2016**, *2016*, 12.
[112] B. Vinsnic, "Nikola CEO: Fuel-Cell Class 8 truck on track for 2021 - SAE International," can be found under http://articles.sae.org/15616/, **2017**.
[113] J. Alazemi, J. Andrews, *Renew. Sustain. Energy Rev.* **2015**, *48*, 483.
[114] M. Melaina, M. Penev, *Hydrogen Station Cost Estimates: Comparing Hydrogen Station Cost Calculator Results with Other Recent Estimates*, NREL (National Renewable Energy Laboratory (NREL), Golden, CO (United States)), **2013**.
[115] N. Qin, P. Brooker, S. Srinivasan, **2014**.
[116] A. Schroeder, T. Traber, *Energy Policy* **2012**, *43*, 136.
[117] A. Lajunen, T. Lipman, *Energy* **2016**, *106*, 329.
[118] C. M. Kalamaras, A. M. Efstathiou, in *Conf. Pap. Sci.*, Hindawi Publishing Corporation, **2013**.
[119] S. Ramachandran, U. Stimming, *Energy Environ. Sci.* **2015**, *8*, 3313.
[120] I. Staffell, P. Dodds, *The Role of Hydrogen and Fuel Cells in Future Energy Systems*, H2FC SUPERGEN, London, UK, **2017**.
[121] P. Zihrul, I. Hartung, S. Kirsch, G. Huebner, F. Hasché, H. A. Gasteiger, *J. Electrochem. Soc.* **2016**, *163*, F492.
[122] T. Hua, R. Ahluwalia, L. Eudy, G. Singer, B. Jermer, N. Asselin-Miller, S. Wessel, T. Patterson, J. Marcinkoski, *J. Power Sources* **2014**, *269*, 975.
[123] Ballard Power Systems, "Ballard Powered Fuel Cell Electric Bus Achieves 25,000 Hours of Revenue Operation," can be found under http://www.ballard.com/modules-display/news-releases/2017/08/29/ballard-powered-fuel-cell-electric-bus-achieves-25-000-hours-of-revenue-operation, **2017**.
[124] AC Transit, "AC Transit's Fuel Cell Program Breaks 25,000 Hour Operating Record," can be found under http://www.actransit.org/2017/07/11/fuel-cell-record-25k/, **2017**.
[125] L. Eudy, M. Post, M. Jeffers, *Fuel Cell Buses in US Transit Fleets: Current Status 2016*, National Renewable Energy Laboratory (NREL), **2016**.
[126] J. Kurtz, S. Sprik, C. Ainscough, G. Saur, **2017**.
[127] A. R. Mainar, L. C. Colmenares, J. A. Blázquez, I. Urdampilleta, *Int. J. Energy Res.* **2017**, *42*, 903.
[128] D. U. Lee, P. Xu, Z. P. Cano, A. G. Kashkooli, M. G. Park, Z. Chen, *J. Mater. Chem. A* **2016**, *4*, 7107.
[129] S. W. T. Price, S. J. Thompson, X. Li, S. F. Gorman, D. Pletcher, A. E. Russell, F. C. Walsh, R. G. A. Wills, *J. Power Sources* **2014**, *259*, 43.
[130] P. N. Ross, H. Sokol, *J. Electrochem. Soc.* **1984**, *131*, 1742.

[131] C. A. Friesen, R. Krishnan, G. Friensen, *Electrochemical Cell with Spacers for Flow Management System*, **2013**, US8492052 B2.
[132] S. Amendola, L. Johnson, M. Binder, M. Kunz, P. J. Black, M. Oster, S. Sharp-Goldman, T. Chciuk, R. Johnson, *Electrically Rechargeable, Metal-Air Battery Systems and Methods*, **2013**, US20130115531 A1.
[133] D. Wolfe, C. A. Friesen, P. B. Johnson, *Ionic Liquid Containing Sulfonate Ions*, **2014**, US8741491 B2.
[134] M. Pinto, S. Smedley, J. A. Colborn, *Refuelable Electrochemical Power Source Capable of Being Maintained in a Substantially Constant Full Condition and Method of Using the Same*, **2004**, US6706433 B2.
[135] M. Pinto, S. Smedley, G. Wu, *Recirculating Anode*, **2004**, US20040251126 A1.
[136] W. A. Garcia, H. F. Wilkins, *Metal-Air Battery with Reduced Gas Diffusion Layer*, **2014**, US8871394 B1.
[137] J. Passaniti, D. Carpenter, R. McKenzie, in *Lindens Handb. Batter. 4th Ed.*, McGraw Hill Professional, New York, **2010**.
[138] E. Deiss, F. Holzer, O. Haas, *Electrochimica Acta* **2002**, *47*, 3995.
[139] H. Ma, B. Wang, Y. Fan, W. Hong, *Energies* **2014**, *7*, 6549.
[140] W. Hong, H. Li, B. Wang, *Int J Electrochem Sci* **2016**, *11*, 3843.
[141] P.-C. Li, Y.-J. Chien, C.-C. Hu, *J. Power Sources* **2016**, *313*, 37.
[142] O. Haas, F. Holzer, K. Müller, S. Müller, in *Handb. Fuel Cells*, John Wiley & Sons, Ltd, Hoboken, **2010**.
[143] K. Kordesch, V. Hacker, in *Handb. Fuel Cells*, John Wiley & Sons, Ltd, Hoboken, **2010**.
[144] J. W. Diggle, A. R. Despic, J. O. Bockris, *J. Electrochem. Soc.* **1969**, *116*, 1503.
[145] A. R. Despić, M. M. Purenović, *J. Electrochem. Soc.* **1974**, *121*, 329.
[146] M. V. Simičić, K. I. Popov, N. V. Krstajić, *J. Electroanal. Chem.* **2000**, *484*, 18.
[147] R. Y. Wang, D. W. Kirk, G. X. Zhang, *J. Electrochem. Soc.* **2006**, *153*, C357.
[148] R. V. Moshtev, P. Zlatilova, *J. Appl. Electrochem.* **1978**, *8*, 213.
[149] J. McBreen, *J. Electrochem. Soc.* **1972**, *119*, 1620.
[150] F. R. McLarnon, E. J. Cairns, *J. Electrochem. Soc.* **1991**, *138*, 645.
[151] Y. Shen, K. Kordesch, *J. Power Sources* **2000**, *87*, 162.
[152] K. W. Choi, D. N. Bennion, J. Newman, *J. Electrochem. Soc.* **1976**, *123*, 1616.
[153] K. W. Choi, D. Hamby, D. N. Bennion, J. Newman, *J. Electrochem. Soc.* **1976**, *123*, 1628.
[154] W. G. Sunu, D. N. Bennion, *J. Electrochem. Soc.* **1980**, *127*, 2007.
[155] W. G. Sunu, D. N. Bennion, *J. Electrochem. Soc.* **1980**, *127*, 2017.
[156] R. E. F. Einerhand, W. Visscher, J. J. M. de Goeij, E. Barendrecht, *J. Electrochem. Soc.* **1991**, *138*, 1.
[157] R. E. F. Einerhand, W. Visscher, J. J. M. de Goeij, E. Barendrecht, *J. Electrochem. Soc.* **1991**, *138*, 7.
[158] R. Jain, T. C. Adler, F. R. McLarnon, E. J. Cairns, *J. Appl. Electrochem.* **1992**, *22*, 1039.
[159] T. C. Adler, F. R. McLarnon, E. J. Cairns, *J. Electrochem. Soc.* **1993**, *140*, 289.
[160] S. Müller, F. Holzer, O. Haas, *J. Appl. Electrochem.* **1998**, *28*, 895.
[161] J. Yu, H. Yang, X. Ai, X. Zhu, *J. Power Sources* **2001**, *103*, 93.

[162] S. Wang, Z. Yang, L. Zeng, *J. Electrochem. Soc.* **2009**, *156*, A18.
[163] D. Zeng, Z. Yang, S. Wang, X. Ni, D. Ai, Q. Zhang, *Electrochimica Acta* **2011**, *56*, 4075.
[164] P. Bonnick, J. R. Dahn, *J. Electrochem. Soc.* **2012**, *159*, A981.
[165] J. Huang, Z. Yang, R. Wang, Z. Zhang, Z. Feng, X. Xie, *J. Mater. Chem. A* **2015**, *3*, 7429.
[166] R. F. Thornton, E. J. Carlson, *J. Electrochem. Soc.* **1980**, *127*, 1448.
[167] T. P. Dirkse, *J. Electrochem. Soc.* **1981**, *128*, 1412.
[168] C.-Y. Jung, T.-H. Kim, W.-J. Kim, S.-C. Yi, *Energy* **2016**, *102*, 694.
[169] T. S. Chang, Y. Y. Wang, C. C. Wan, *J. Power Sources* **1983**, *10*, 167.
[170] X. G. Zhang, *J. Power Sources* **2006**, *163*, 591.
[171] E. G. Gagnon, Y.-M. Wang, *J. Electrochem. Soc.* **1987**, *134*, 2091.
[172] T. S. Lee, *J. Electrochem. Soc.* **1971**, *118*, 1278.
[173] C. W. Lee, S. W. Eom, K. Sathiyanarayanan, M. S. Yun, *Electrochimica Acta* **2006**, *52*, 1588.
[174] J. Fu, Z. P. Cano, M. G. Park, A. Yu, M. Fowler, Z. Chen, *Adv. Mater.* **2017**, *29*, 1604685.
[175] J. F. Parker, C. N. Chervin, E. S. Nelson, D. R. Rolison, J. W. Long, *Energy Environ. Sci.* **2014**, *7*, 1117.
[176] Z. Yan, E. Wang, L. Jiang, G. Sun, *RSC Adv.* **2015**, *5*, 83781.
[177] M. Chamoun, B. J. Hertzberg, T. Gupta, D. Davies, S. Bhadra, B. Van Tassell, C. Erdonmez, D. A. Steingart, *NPG Asia Mater.* **2015**, *7*, e178.
[178] K. Bass, P. J. Mitchell, G. D. Wilcox, J. Smith, *J. Power Sources* **1991**, *35*, 333.
[179] M. N. Masri, A. A. Mohamad, *Corros. Sci.* **2009**, *51*, 3025.
[180] C. Biegler, R. L. Deutscher, S. Fletcher, S. Hua, R. Woods, *J. Electrochem. Soc.* **1983**, *130*, 2303.
[181] R. Othman, A. H. Yahaya, A. K. Arof, *J. Appl. Electrochem.* **2002**, *32*, 1347.
[182] M. N. Masri, A. A. Mohamad, *J. Electrochem. Soc.* **2013**, *160*, A715.
[183] J. Fu, D. U. Lee, F. M. Hassan, L. Yang, Z. Bai, M. G. Park, Z. Chen, *Adv. Mater.* **2015**, *27*, 5617.
[184] J. Fu, J. Zhang, X. Song, H. Zarrin, X. Tian, J. Qiao, L. Rasen, K. Li, Z. Chen, *Energy Environ. Sci.* **2016**, *9*, 663.
[185] D. U. Lee, J. Fu, M. G. Park, H. Liu, A. Ghorbani Kashkooli, Z. Chen, *Nano Lett.* **2016**, *16*, 1794.
[186] J. McBreen, E. Gannon, *Electrochimica Acta* **1981**, *26*, 1439.
[187] J. McBreen, M. G. Chu, G. Adzic, *J. Electrochem. Soc.* **1981**, *128*, 2287.
[188] J. McBreen, E. Gannon, *J. Electrochem. Soc.* **1983**, *130*, 1980.
[189] J. McBreen, E. Gannon, *J. Power Sources* **1985**, *15*, 169.
[190] F. Moser, F. Fourgeot, R. Rouget, O. Crosnier, T. Brousse, *Electrochimica Acta* **2013**, *109*, 110.
[191] Y. Sato, M. Kanda, H. Niki, M. Ueno, K. Murata, T. Shirogami, T. Takamura, *J. Power Sources* **1983**, *9*, 147.
[192] J.-S. Chen, L.-F. Wang, *J. Appl. Electrochem.* **1996**, *26*, 227.
[193] H. Yang, H. Zhang, X. Wang, J. Wang, X. Meng, Z. Zhou, *J. Electrochem. Soc.* **2004**, *151*, A2126.

[194] X. Fan, Z. Yang, R. Wen, B. Yang, W. Long, *J. Power Sources* **2013**, *224*, 80.
[195] R. Wang, Z. Yang, B. Yang, X. Fan, T. Wang, *J. Power Sources* **2014**, *246*, 313.
[196] J. Zhu, Y. Zhou, *J. Power Sources* **1998**, *73*, 266.
[197] J. Vatsalarani, D. C. Trivedi, K. Ragavendran, P. C. Warrier, *J. Electrochem. Soc.* **2005**, *152*, A1974.
[198] Y. F. Yuan, L. Q. Yu, H. M. Wu, J. L. Yang, Y. B. Chen, S. Y. Guo, J. P. Tu, *Electrochimica Acta* **2011**, *56*, 4378.
[199] X. Fan, Z. Yang, W. Long, Z. Zhao, B. Yang, *Electrochimica Acta* **2013**, *92*, 365.
[200] Y. F. Yuan, J. P. Tu, H. M. Wu, C. Q. Zhang, S. F. Wang, X. B. Zhao, *J. Power Sources* **2007**, *165*, 905.
[201] S.-H. Lee, C.-W. Yi, K. Kim, *J. Phys. Chem. C* **2011**, *115*, 2572.
[202] X. G. Zhang, in *Encycl. Electrochem. Power Sources* (Ed.: J. Garche), Elsevier, Amsterdam, **2009**, pp. 454–468.
[203] V. Caramia, B. Bozzini, *Mater. Renew. Sustain. Energy* **2014**, *3*, 1.
[204] M. Xu, D. G. Ivey, Z. Xie, W. Qu, *J. Power Sources* **2015**, *283*, 358.
[205] D. U. Lee, J. Fu, Z. Chen, **2016**.
[206] A. R. Mainar, O. Leonet, M. Bengoechea, I. Boyano, I. de Meatza, A. Kvasha, A. Guerfi, J. Alberto Blázquez, *Int. J. Energy Res.* **2016**, n/a.
[207] P. Pei, K. Wang, Z. Ma, *Appl. Energy* **2014**, *128*, 315.
[208] K. Harting, U. Kunz, T. Turek, *Z. Für Phys. Chem. Int. J. Res. Phys. Chem. Chem. Phys.* **2011**, *226*, 151.
[209] T. J. Simons, A. A. J. Torriero, P. C. Howlett, D. R. MacFarlane, M. Forsyth, *Electrochem. Commun.* **2012**, *18*, 119.
[210] M. Kar, T. J. Simons, M. Forsyth, D. R. MacFarlane, *Phys. Chem. Chem. Phys.* **2014**, *16*, 18658.
[211] C.-C. Yang, S.-J. Lin, *J. Power Sources* **2002**, *112*, 497.
[212] A. A. Mohamad, N. S. Mohamed, M. Z. A. Yahya, R. Othman, S. Ramesh, Y. Alias, A. K. Arof, *Solid State Ion.* **2003**, *156*, 171.
[213] J. Liu, C. Guan, C. Zhou, Z. Fan, Q. Ke, G. Zhang, C. Liu, J. Wang, *Adv. Mater.* **2016**, n/a.
[214] M. C. Cheiky, *Electrolyte Distributing System and Method*, **1997**, US5615717 A.
[215] L. T. Skeggs, J. E. Young, E. C. Cherry, *Cathode Air Recirculation and Moisture Control*, **1996**, EP0696384 B1.
[216] M. C. Cheiky, *Coated Cathode for Rechargeable Metal Battery*, **1995**, US5432022 A.
[217] J. R. Goldstein, Y. Harats, Y. Sharon, N. Naimer, *Scrubber System for Removing Carbon Dioxide from a Metal-Air or Fuel Cell Battery*, **1997**, US5595949 A.
[218] C. S. Pedicni, *Load Responsive Air Door for an Electrochemical Cell*, **2002**, US6350537 B1.
[219] T. P. Dirkse, N. A. Hampson, *Electrochimica Acta* **1972**, *17*, 383.
[220] R. J. Gilliam, J. W. Graydon, D. W. Kirk, S. J. Thorpe, *Int. J. Hydrog. Energy* **2007**, *32*, 359.
[221] E. G. Gagnon, *J. Electrochem. Soc.* **1986**, *133*, 1989.
[222] E. G. Gagnon, *J. Electrochem. Soc.* **1991**, *138*, 3173.
[223] T. C. Adler, F. R. McLarnon, E. J. Cairns, *Ind. Eng. Chem. Res.* **1998**, *37*, 3237.

[224] J. T. Nichols, F. R. McLarnon, E. J. Cairns, *Chem. Eng. Commun.* **1985**, *37*, 355.
[225] D. U. Lee, J.-Y. Choi, K. Feng, H. W. Park, Z. Chen, *Adv. Energy Mater.* **2014**, *4*, 1301389.
[226] E. L. Dewi, K. Oyaizu, H. Nishide, E. Tsuchida, *J. Power Sources* **2003**, *115*, 149.
[227] N. Fujiwara, M. Yao, Z. Siroma, H. Senoh, T. Ioroi, K. Yasuda, *J. Power Sources* **2011**, *196*, 808.
[228] F. Büker, D. Hertkorn, C. Müller, H. Reinecke, *ECS Trans.* **2014**, *58*, 69.
[229] B. Bertolotti, H. Messaoudi, L. Chikh, C. Vancaeyzeele, S. Alfonsi, O. Fichet, *J. Power Sources* **2015**, *274*, 488.
[230] J. Zhang, J. Fu, X. Song, G. Jiang, H. Zarrin, P. Xu, K. Li, A. Yu, Z. Chen, *Adv. Energy Mater.* **2016**, n/a.
[231] S. Zhu, Z. Chen, B. Li, D. Higgins, H. Wang, H. Li, Z. Chen, *Electrochimica Acta* **2011**, *56*, 5080.
[232] D. U. Lee, H. W. Park, D. Higgins, L. Nazar, Z. Chen, *J. Electrochem. Soc.* **2013**, *160*, F910.
[233] J. W. D. Ng, M. Tang, T. F. Jaramillo, *Energy Environ. Sci.* **2014**, *7*, 2017.
[234] C. Ma, N. Xu, J. Qiao, S. Jian, J. Zhang, *Int. J. Hydrog. Energy* **2016**, *41*, 9211.
[235] F. Bidault, D. J. L. Brett, P. H. Middleton, N. P. Brandon, *J. Power Sources* **2009**, *187*, 39.
[236] F. Bidault, A. Kucernak, *J. Power Sources* **2010**, *195*, 2549.
[237] K. Tomantschger, K. V. Kordesch, *J. Power Sources* **1989**, *25*, 195.
[238] K. Kordesch, M. Cifrain, *Handb. Fuel Cells* **2010**.
[239] G. V. Shteinberg, A. V. Dribinsky, I. A. Kukushkina, L. N. Mokorousov, V. S. Bagotzky, *J. Electroanal. Chem. Interfacial Electrochem.* **1984**, *180*, 619.
[240] A. L. Dicks, *J. Power Sources* **2006**, *156*, 128.
[241] V. Neburchilov, H. Wang, J. J. Martin, W. Qu, *J. Power Sources* **2010**, *195*, 1271.
[242] J. Giner, C. Hunter, *J. Electrochem. Soc.* **1969**, *116*, 1124.
[243] P. Björnbom, *Electrochimica Acta* **1987**, *32*, 115.
[244] M. L. Perry, J. Newman, E. J. Cairns, *J. Electrochem. Soc.* **1998**, *145*, 5.
[245] N. Staud, P. N. Ross, *J. Electrochem. Soc.* **1986**, *133*, 1079.
[246] K. Kinoshita, in *Handb. Battery Mater.* (Eds.: -Ing Claus Daniel, J.O. Besenhard), Wiley-VCH Verlag GmbH & Co. KGaA, Weinheim, **2011**, pp. 269–284.
[247] P. Vanýsek, in *CRC Handb. Chem. Phys. 97th Ed.*, CRC Press, Boca Raton, **2016**.
[248] P. N. Ross, M. Sattler, *J. Electrochem. Soc.* **1988**, *135*, 1464.
[249] N. Staud, H. Sokol, P. N. Ross, *J. Electrochem. Soc.* **1989**, *136*, 3570.
[250] S. Müller, K. Striebel, O. Haas, *Electrochimica Acta* **1994**, *39*, 1661.
[251] S. Müller, F. Holzer, H. Arai, O. Haas, *J. New Mater. Electrochem. Syst.* **1999**, *2*, 227.
[252] T. Thippani, S. Mandal, G. Wang, V. K. Ramani, R. Kothandaraman, *RSC Adv.* **2016**, *6*, 71122.
[253] J.-F. Drillet, F. Holzer, T. Kallis, S. Müller, V. M. Schmidt, *Phys. Chem. Chem. Phys.* **2001**, *3*, 368.
[254] E. Gülzow, N. Wagner, M. Schulze, *Fuel Cells* **2003**, *3*, 67.
[255] D. Wittmaier, N. Wagner, K. A. Friedrich, H. M. A. Amin, H. Baltruschat, *J. Power Sources* **2014**, *265*, 299.

[256] X. Li, D. Pletcher, A. E. Russell, F. C. Walsh, R. G. A. Wills, S. F. Gorman, S. W. T. Price, S. J. Thompson, *Electrochem. Commun.* **2013**, *34*, 228.
[257] S. B. Sherman, Z. P. Cano, M. Fowler, Z. Chen, *Energy 2018 Vol 5 Pages 121-145* **2018**, DOI 10.3934/energy.2018.1.121.
[258] W. A. Armstrong, *An Oxygen Electrode Based on Nickel/Cobalt Spinel*, Defence Research Establishment Ottawa, Ottawa, Ontario (Canada), **1981**.
[259] F. Cheng, J. Chen, *Chem. Soc. Rev.* **2012**, *41*, 2172.
[260] Z.-L. Wang, D. Xu, J.-J. Xu, X.-B. Zhang, *Chem. Soc. Rev.* **2014**, *43*, 7746.
[261] L. Jöerissen, in *Encycl. Electrochem. Power Sources*, Elsevier, Amsterdam, **2009**, pp. 356–371.
[262] S. Gupta, W. Kellogg, H. Xu, X. Liu, J. Cho, G. Wu, *Chem. – Asian J.* **2016**, *11*, 10.
[263] Y. Gorlin, B. Lassalle-Kaiser, J. D. Benck, S. Gul, S. M. Webb, V. K. Yachandra, J. Yano, T. F. Jaramillo, *J. Am. Chem. Soc.* **2013**, *135*, 8525.
[264] Y. Shimizu, K. Uemura, H. Matsuda, N. Miura, N. Yamazoe, *J. Electrochem. Soc.* **1990**, *137*, 3430.
[265] J.-I. Jung, H. Y. Jeong, J.-S. Lee, M. G. Kim, J. Cho, *Angew. Chem. Int. Ed.* **2014**, *53*, 4582.
[266] J. Suntivich, H. A. Gasteiger, N. Yabuuchi, H. Nakanishi, J. B. Goodenough, Y. Shao-Horn, *Nat. Chem.* **2011**, *3*, 546.
[267] J. Suntivich, K. J. May, H. A. Gasteiger, J. B. Goodenough, Y. Shao-Horn, *Science* **2011**, *334*, 1383.
[268] J.-I. Jung, H. Y. Jeong, M. G. Kim, G. Nam, J. Park, J. Cho, *Adv. Mater.* **2015**, *27*, 266.
[269] J.-I. Jung, S. Park, M.-G. Kim, J. Cho, *Adv. Energy Mater.* **2015**, *5*, n/a.
[270] J. Ponce, J.-L. Rehspringer, G. Poillerat, J. L. Gautier, *Electrochimica Acta* **2001**, *46*, 3373.
[271] M. Hamdani, R. N. Singh, P. Chartier, *Int. J. Electrochem. Sci.* **2010**, *5*, 556.
[272] F. Cheng, J. Shen, B. Peng, Y. Pan, Z. Tao, J. Chen, *Nat. Chem.* **2011**, *3*, 79.
[273] D. Pletcher, X. Li, S. W. T. Price, A. E. Russell, T. Sönmez, S. J. Thompson, *Electrochimica Acta* **2016**, *188*, 286.
[274] M. G. Park, D. U. Lee, M. H. Seo, Z. P. Cano, Z. Chen, *Small* **2016**, *12*, 2707.
[275] W. Song, Z. Ren, S.-Y. Chen, Y. Meng, S. Biswas, P. Nandi, H. A. Elsen, P.-X. Gao, S. L. Suib, *ACS Appl. Mater. Interfaces* **2016**, *8*, 20802.
[276] X. Han, X. Wu, C. Zhong, Y. Deng, N. Zhao, W. Hu, *Nano Energy* **2017**, *31*, 541.
[277] J.-T. Ren, G.-G. Yuan, C.-C. Weng, Z.-Y. Yuan, *ACS Sustain. Chem. Eng.* **2018**, *6*, 707.
[278] X. Han, G. He, Y. He, J. Zhang, X. Zheng, L. Li, C. Zhong, W. Hu, Y. Deng, T.-Y. Ma, *Adv. Energy Mater.* **2018**, *8*, 1702222.
[279] X. Liu, M. Park, M. G. Kim, S. Gupta, X. Wang, G. Wu, J. Cho, *Nano Energy* **2016**, *20*, 315.
[280] J. Park, M. Risch, G. Nam, M. Park, T. J. Shin, S. Park, M. G. Kim, Y. Shao-Horn, J. Cho, *Energy Environ. Sci.* **2017**, *10*, 129.
[281] A. K. Shukla, S. Venugopalan, B. Hariprakash, *J. Power Sources* **2001**, *100*, 125.
[282] K. Watanabe, T. Kikuoka, N. Kumagai, *J. Appl. Electrochem.* **1995**, *25*, 219.
[283] Y. L. Cao, H. X. Yang, X. P. Ai, L. F. Xiao, *J. Electroanal. Chem.* **2003**, *557*, 127.

[284] J. Yan, Z. Fan, W. Sun, G. Ning, T. Wei, Q. Zhang, R. Zhang, L. Zhi, F. Wei, *Adv. Funct. Mater.* **2012**, *22*, 2632.
[285] S. L. Medway, C. A. Lucas, A. Kowal, R. J. Nichols, D. Johnson, *J. Electroanal. Chem.* **2006**, *587*, 172.
[286] S. Yamabi, H. Imai, *J. Mater. Chem.* **2002**, *12*, 3773.
[287] X. Qu, D. Jia, *J. Cryst. Growth* **2009**, *311*, 1223.
[288] K. Harrison, L. B. Hazell, *Surf. Interface Anal.* **1992**, *18*, 368.
[289] S. Evans, *Surf. Interface Anal.* **1992**, *18*, 323.
[290] M. C. Biesinger, B. P. Payne, A. P. Grosvenor, L. W. M. Lau, A. R. Gerson, R. St. C. Smart, *Appl. Surf. Sci.* **2011**, *257*, 2717.
[291] I. G. Casella, M. R. Guascito, M. G. Sannazzaro, *J. Electroanal. Chem.* **1999**, *462*, 202.
[292] M. Schulze, R. Reissner, M. Lorenz, U. Radke, W. Schnurnberger, *Electrochimica Acta* **1999**, *44*, 3969.
[293] D. Gioia, A. Laurita, G. D. Bello, I. G. Casella, *J. Solid State Electrochem.* **2016**, *20*, 3383.
[294] A. N. Mansour, C. A. Melendres, *Surf. Sci. Spectra* **1994**, *3*, 271.
[295] J.-G. Kim, D. L. Pugmire, D. Battaglia, M. A. Langell, *Appl. Surf. Sci.* **2000**, *165*, 70.
[296] J. Yang, H. Liu, W. N. Martens, R. L. Frost, *J. Phys. Chem. C* **2010**, *114*, 111.
[297] C. Yuan, J. Li, L. Hou, X. Zhang, L. Shen, X. W. (David) Lou, *Adv. Funct. Mater.* **2012**, *22*, 4592.
[298] J. F. Marco, J. R. Gancedo, M. Gracia, J. L. Gautier, E. Ríos, F. J. Berry, *J. Solid State Chem.* **2000**, *153*, 74.
[299] B. P. Payne, M. C. Biesinger, N. S. McIntyre, *J. Electron Spectrosc. Relat. Phenom.* **2012**, *185*, 159.
[300] H. Arai, S. Müller, O. Haas, *J. Electrochem. Soc.* **2000**, *147*, 3584.
[301] X.-Z. Yuan, C. Song, H. Wang, J. Zhang, in *Electrochem. Impedance Spectrosc. PEM Fuel Cells Fundam. Appl.*, Springer London, London, **2010**, pp. 139–192.
[302] M. De Koninck, B. Marsan, *Electrochimica Acta* **2008**, *53*, 7012.
[303] Y. Liang, Y. Li, H. Wang, J. Zhou, J. Wang, T. Regier, H. Dai, *Nat. Mater.* **2011**, *10*, 780.
[304] M. Prabu, K. Ketpang, S. Shanmugam, *Nanoscale* **2014**, *6*, 3173.
[305] J. N. Soderberg, A. C. Co, A. H. C. Sirk, V. I. Birss, *J. Phys. Chem. B* **2006**, *110*, 10401.
[306] X. Ge, A. Sumboja, D. Wuu, T. An, B. Li, F. W. T. Goh, T. S. A. Hor, Y. Zong, Z. Liu, *ACS Catal.* **2015**, *5*, 4643.
[307] B. V. Tilak, S. Venkatesh, S. K. Rangarajan, *J. Electrochem. Soc.* **1989**, *136*, 1977.
[308] Z. X. Liu, Z. P. Li, H. Y. Qin, B. H. Liu, *J. Power Sources* **2011**, *196*, 4972.
[309] A. T. Marshall, L. Vaisson-Béthune, *Electrochem. Commun.* **2015**, *61*, 23.
[310] S. Panero, in *Encycl. Electrochem. Power Sources* (Ed.: J. Garche), Elsevier, Amsterdam, **2009**, pp. 14–22.
[311] S. H. Masood, W. Q. Song, *Mater. Des.* **2004**, *25*, 587.
[312] X. He, Q. Liu, J. Liu, R. Li, H. Zhang, R. Chen, J. Wang, *J. Alloys Compd.* **2017**, *724*, 130.
[313] X. Guo, T. Zheng, G. Ji, N. Hu, C. Xu, Y. Zhang, *J. Mater. Chem. A* **2018**, *6*, 10243.
[314] J. Benziger, J. Nehlsen, D. Blackwell, T. Brennan, J. Itescu, *J. Membr. Sci.* **2005**, *261*, 98.

[315] R. Banerjee, J. Hinebaugh, H. Liu, R. Yip, N. Ge, A. Bazylak, *Int. J. Hydrog. Energy* **2016**, *41*, 14885.
[316] P. Glaris, J.-F. Coulon, M. Dorget, F. Poncin-Epaillard, *Polymer* **2013**, *54*, 5858.
[317] S. A. A. Mansour, *Mater. Chem. Phys.* **1994**, *36*, 317.
[318] L. Ouyang, Q. Liu, C. Xu, C. Liu, H. Liang, *Talanta* **2017**, *164*, 283.
[319] B. Małecka, A. Łącz, E. Drożdż, A. Małecki, *J. Therm. Anal. Calorim.* **2015**, *119*, 1053.
[320] Y. Takagi, J.-C. Lee, S. Yagi, H. Yamane, T. Wano, D. Kitagawa, A. El Salmawy, *Polymer* **2011**, *52*, 4099.
[321] X. Tan, H. Gao, M. Yang, Y. Luan, W. Dong, Z. Jin, J. Yu, Y. Qi, Y. Feng, G. Wang, *J. Alloys Compd.* **2014**, *608*, 278.
[322] Q. Wang, S. Liu, H. Sun, Q. Lu, *Ind. Eng. Chem. Res.* **2014**, *53*, 7917.
[323] D. U. Lee, J. Li, M. G. Park, M. H. Seo, W. Ahn, I. Stadelmann, L. Ricardez-Sandoval, Z. Chen, *ChemSusChem* **2017**, *10*, 2258.

Appendix

Theoretical Specific Energy Calculation

Unlike conventional batteries, metal-air batteries gain mass as they are discharged. This is due to oxidation of the metal from O_2, which enters from outside the battery during the discharge process. Therefore, the "instantaneous" theoretical specific energy of a metal-air battery changes as it is discharged, and is governed by **Equation A.1**:

$$\text{Instantaneous Specific Energy (Wh kg}^{-1}) = \frac{F \cdot n \cdot OCV}{3.6} \cdot \frac{1}{DOD \cdot M_{M+O} + (1 - DOD) \cdot M_{Metal}}$$

$$= \frac{F \cdot n \cdot OCV}{3.6} \cdot \frac{1}{(M_{M+O} - M_{Metal}) \cdot DOD + M_{Metal}}$$

(Equation A.1)

where F is the Faraday constant, n is the number of electrons transferred per metal ion, OCV is the metal-air battery's nominal voltage, DOD is the fractional depth of discharge (0 for fully charged state, 1 for fully discharged state), M_{Metal} is the molar mass of the metal anode and M_{M+O} is the combined molar mass of the metal anode and the stoichiometric amount of O_2 that enters the battery. To calculate the overall theoretical specific energy of the metal-air battery, Equation A.1 must be integrated:

$$\text{Specific Energy (Wh kg}^{-1}) = \frac{F \cdot n \cdot OCV}{3.6} \int_0^1 \frac{1}{(M_{M+O} - M_{Metal}) \cdot DOD + M_{Metal}} d(DOD)$$

$$= \frac{F \cdot n \cdot OCV}{3.6} \left[\frac{\ln [(M_{M+O} - M_{Metal}) \cdot DOD + M_{Metal}]}{M_{M+O} - M_{Metal}} + C \right]$$

where C is a constant. Evaluating from DOD=0 to DOD=1 reveals the overall theoretical specific energy of the metal-air battery (**Equation A.2)**:

$$\text{Specific Energy (Wh kg}^{-1}) = \frac{F \cdot n \cdot OCV}{3.6} \left[\frac{\ln [(M_{M+O} - M_{Metal}) + M_{Metal}]}{M_{M+O} - M_{Metal}} - \frac{\ln [M_{Metal}]}{M_{M+O} - M_{Metal}} \right]$$

$$= \frac{F \cdot n \cdot OCV}{3.6} \left[\frac{\ln [M_{M+O} / M_{Metal}]}{M_{M+O} - M_{Metal}} \right] \qquad \textbf{(Equation A.2)}$$

By accounting for O_2 uptake, the specific energy calculated with **Equation A.2** enables a more realistic comparison of metal-air battery energy densities, either between each other or with conventional closed-system battery chemistries. This equation is thus used to calculate the specific energies in **Figure 1.1**.

Theoretical Metal-Air Battery Parameters

For each of the metal-air battery chemistries presented in **Figure 1.1**, **Table A.1** lists the most relevant theoretical parameters and the values used to calculate them. Specific capacity and specific energy values are calculated using the method described above. Volumetric capacity and energy densities were calculated using the density of the anode in its most favorable oxidized phase (**Equation A.3**), since the volume of a metal-air battery must accommodate the associated volume expansion of this phase from the metallic form.

$$Volumetric\ Energy\ Density\ = (Specific\ Energy) \cdot (Oxidized\ Anode\ Density)$$

(Equation A.3)

Table A.1. Theoretical metal-air battery parameters

Anode element	n	M_{Metal} [g mol^{-1}]	M_{M+O} [g mol^{-1}]	Oxidized Anode	Oxidized Anode Density [kg L^{-1}]	OCV [V]	Specific Capacity [Ah kg^{-1}]	Volumetric Capacity Density [Ah L^{-1}]	Specific Energy [Wh kg^{-1}]	Volumetric Energy Density [Wh L^{-1}]
Li	1	6.94	22.94	Li_2O_2	2.31	2.96	2003	2699	5928	7989
K	1	39.10	71.10	KO_2	2.14	2.37	501	807	1187	1913
Na	1	22.99	54.99	NaO_2	2.20	2.30	730	1072	1680	2466
Mg	2	24.31	40.30	$Mg(OH)_2$	2.34	3.09	1695	3112	5238	9619
Al	3	26.98	50.98	$Al(OH)_3$	2.42	2.71	2132	3817	5779	10,347
Zn	2	65.39	81.41	ZnO	5.61	1.66	733	3694	1218	6136
Fe	2	55.85	71.84	$Fe(OH)_2$	3.4	1.28	844	2537	1080	3244

Supplementary Tables for Chapter 2

Supplementary Tables for **Chapter 2** are available in Excel format online at

https://static-content.springer.com/esm/art%3A10.1038%2Fs41560-018-0108-1/MediaObjects/41560_2018_108_MOESM1_ESM.xlsx

or

https://tinyurl.com/y5mx7yyh